CONTROL OF THE SPIN RELAXATION AND MAGNETIC ANISOTROPY IN $FE_{1-X}GA_X$/ZNSE SYSTEMS

By

Hongyan Li

A dissertation submitted in partial fulfillment
of the requirements for the degree

of

Doctor of Philosophy

in

Physics

MONTANA STATE UNIVERSITY
Bozeman, Montana

July 2011

APPROVAL

of a dissertation submitted by

Hongyan Li

This dissertation has been read by each member of the dissertation committee and has been found to be satisfactory regarding content, English usage, format, citations, bibliographic style, and consistency, and is ready for submission to The Graduate School.

Dr. Yves Idzerda

Approved for the Department of Physics

Dr. Richard J. Smith

Approved for The Graduate School

Dr. Carl A. Fox

STATEMENT OF PERMISSION TO USE

In presenting this dissertation in partial fulfillment of the requirements for a doctoral degree at Montana State University, I agree that the Library shall make it available to borrowers under rules of the Library. I further agree that copying of this dissertation is allowable only for scholarly purposes, consistent with "fair use" as prescribed in the U.S. Copyright Law. Requests for extensive copying or reproduction of this dissertation should be referred to ProQuest Information and Learning, 300 North Zeeb Road, Ann Arbor, Michigan 48106, to whom I have granted "the exclusive right to reproduce and distribute my dissertation in and from microform along with the non-exclusive right to reproduce and distribute my abstract in any format in whole or in part."

Hongyan Li

July 2011

To my Parents

Thank you for making my dream your dream.

ACKNOWLEDGEMENTS

The first person I would like to thank is Prof. Yves Idzerda, thank you for helping to make the thesis I like and leading me into the research I like. Yves has so many good characters that I can not list all of them here. The two characters that impressed me most and all the students in the lab benefit from are: He is the one who always put the magic sparkling in science which lights up the student's interests. He is a person who always put the others in the front and he showed us to always respect others.

Second I would like to thank the Physics Department for giving me the chance to study physics and supporting me through the long years. The professors here made me love physics. I especially want to thank those who gave me lectures as well as my committee members, Dr. Dick Smith, Dr. John Neumeier and Dr. Greg Francis for their patience and confidence in me. Dr. Galina Malovichko, Ian Vrable and Karl Sebby thank you for your generosity for letting me use your instruments and helping me with the EPR measurements. Sarah, Margaret, thank you for taking care of my business all the time.

I would like to thank everyone in the lab. Dr. Paul Rugheimer, he is always there to help and share. Adam McClure, he is the best partner to work with. Dr. Alex Lussier, Dr. Damon Resnick, Dr. Ezana Negusse, Dr. Keith Gilmore, many thanks to you for introducing me into the new field. Thanks to Harsh Bhatkar and Vanessa Pool for their interesting conversations in the lab.

Besides my academic journey I have met wonderful people who are always there to help others. Sytil, Heather (Gus's mom), Zeb, Zachary…You guys are angels.

Finally, I would like to thank my husband Zhixin, for his love and support to the family. Thanks to my lovely kids, Richfield and Claire for bringing in the fun in life.

TABLE OF CONTENTS

TABLE OF CONTENTS-CONTINUED

TABLE OF CONTENTS-CONTINUED

LIST OF TABLES

Table Page

LIST OF FIGURES

Figure Page

LIST OF FIGURES – CONTINUED

Figure Page

LIST OF FIGURES – CONTINUED

Figure Page

LIST OF FIGURES – CONTINUED

Figure Page

LIST OF FIGURES – CONTINUED

Figure Page

LIST OF FIGURES – CONTINUED

Figure Page

ABSTRACT

Magnetostrictive materials will deform under application of a magnetic field. They can be deposited onto various substrates for engineering multifunctional materials, such as integrated micro actuators and multiferroric materials. In this dissertation clamping of a magnetostrive material onto a substrate is demonstrated to give control of the magnetic anisotropy and spin relaxation, to serve as a device with tunable spin relaxation, which uses magnetic field to change the strain and affect the relaxation. The purpose of this thesis is to use ferromagnetic resonance to investigate the interface effects (chemical bonding, interface strain…) on the magnetic anisotropy properties and the magnetic moment relaxation of $Fe_{1-x}Ga_x$ /ZnSe for different Ga doping.

$Fe_{1-x}Ga_x$ has been deposited on ZnSe(001) and ZnSe(110) surfaces. The growth was epitaxial and the crystal axes are perfectly aligned. Angular ferromagnetic resonance in the X-band (9.4 GHz) and Q-band (34.6 GHz) have been done on samples for a veriety of Ga concentrations and thicknesses.

The anisotropies for $Fe_{1-x}Ga_x$/ZnSe are found to be composed of a cubic term, an in-plane uniaxial term, and the out-of-plane uniaxial term. The in-plane uniaxial term changes its magnitude and direction with Ga doping while the cubic anisotropy term follows the same trend as the bulk material. The direction switch of the uniaxial anisotropy and the field dependence of the uniaxial term indicated that the uniaxial term is generated from anisotropic strain relaxation.

INTRODUCTION

Motivation

Magnetostrictive materials are a class of smart materials which under the influence of magnetic field they change their shape. The change of shape in turn affects the magnetization state which can lead to applications as sensors and actuators.

Magnetoelastic alloys in the thin film form are of current interest as materials for thin film magnetostrictive actuators [1], multiferroric heterostructures, and voltage controlled spin dynamics.

Multiferroric materials are attracting more and more research into the field. Multiferroric materials are both ferroelectric and ferromagnetic materials. The multiferroric research was developed to some extent in 1960s, but due to the difficulty in producing such materials, the research was halted. The multiferroric materials today are mainly ferroelectric and anti-ferromagnetic, but most applications require a ferromagnetic and ferroelectric material. Another route to this research would be to engineer a heterostructure which contains ferromagnetic material and ferroelectric material, so the structure will behave as a multiferroric composite. In multiferroric materials, we can use an electric field to control magnetic properties as outlined in Figure 1 [2], or use the magnetic properties to control the ferrroelectic polarization as shown in Figure 2. In Figure 2, the ferromagnetic material has a large magnetostriction. When the direction of its magnetic moment is changed through the application of an applied field, the dimension of the material will change. So the ferroelectric material will change its polarization.

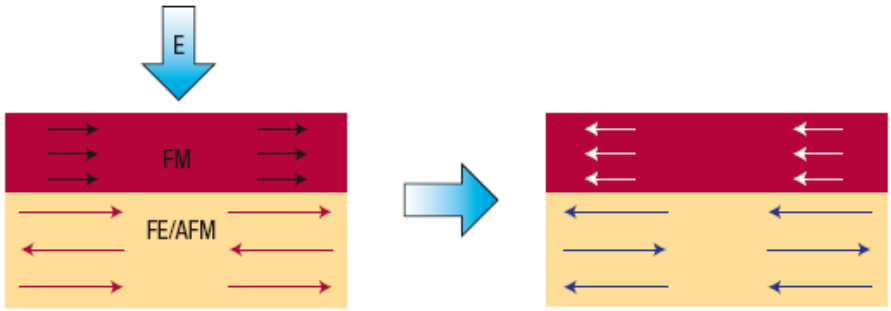

Figure 1: Heterostructures that can use electric field to control the magnetic properties of the thin films[2]. Reprinted by permission from Macmillan Publishers Ltd: Nature Materials, (vol **6**(1), page 21), copyright (2007).

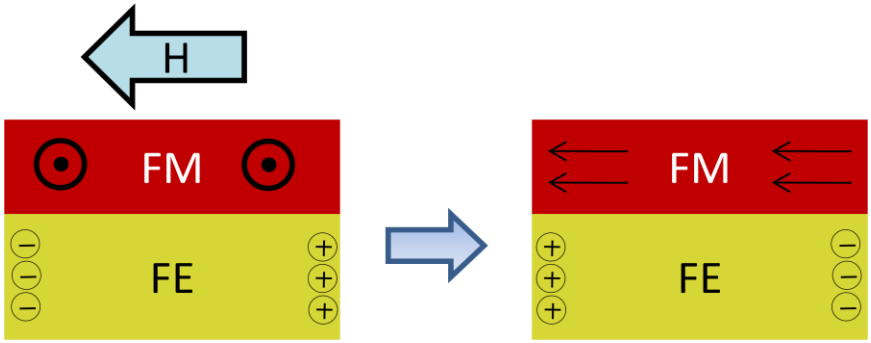

Figure 2: Heterostructures that can use magnetic field to control the polarization of ferroelectric thin film.

For single-crystal epitaxial thin films, when a magnetoelastic material is deposited onto non-magnetoelastic material, the application of a magnetic field will generate a uni-axial magnetoelastic stress in the pinned film. This stress creates a structural distortion in the crystal, resulting in an additional field dependent magnetic anisotropy. Having an applied mechanical stress (including from a piezoelectric substrate) affecting the magnetic anisotropy and modifying spin dynamics opens interesting possibilities for voltage controlled spin dynamics and magnetization reversal.

Bulk $Fe_{1-x}Al_x$ and $Fe_{1-x}Ga_x$ alloys show large magnetostriction. Because these alloys are not brittle, they become an interesting material for many applications. Bulk $Fe_{1-x}Ga_x$ has been extensively studied [3-7]. Fe deposited onto GaAs and ZnSe has also been extensively studied especially for the uniaxial in plane anisotropy [8-11]. But only a few $Fe_{1-x}Ga_x$ thin films have been studied in the literature [12-14].

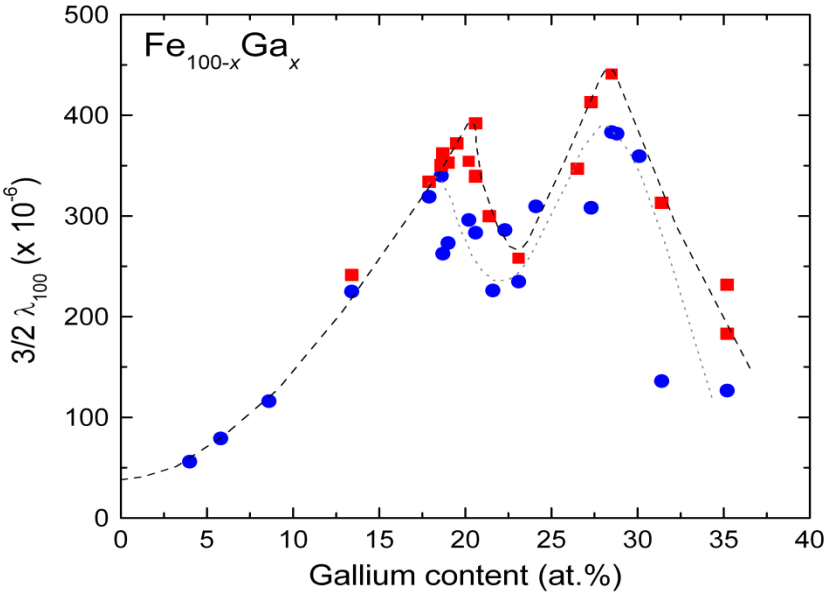

Figure 3: (3/2) λ_{100} as a function of Ga concentration for $Fe_{1-x}Ga_x$ [7]. Samples were annealed and either slow cooled (blue circles) or quenched in water (red square). With kind permission from Springer Science+Business Media: Magnetostriction of Binary and Ternary Fe-Ga Alloys, Journal of Materials Science **42** (2007) 9582, E. Summers, T. Lograsso, and M. Wun-Fogle, figure 1.

Magnetostriction usually is defined using magnetostriction constant λ, which describes the relation between the applied field and the saturation magnetostriction. Magnetostrictions are anisotropic. Tetragonal magnetostriction λ_{100} and rhombohedral magnetostriction constant λ_{111} are normally used to describe a cubic system. λ_{100} is defined as the saturation deformation in the [100] direction when the applied field is also

in the [100] direction. Same as λ_{100}, λ_{111} is defined as the saturation deformation in the [111] direction when the applied field is also in the [111] direction.

In the bulk form, the magnetic, elastic, and magnetoelastic properties vary as doping concentration *x*. When *x* increases, the tetragonal magnetostriction constant λ_{100} for $Fe_{1-x}Ga_x$ increases and shows a peak at 19% Ga concentration. It then decreases but reaches another peak at around 27% Ga doping [3] as shown in Figure 3. Contrary to λ_{100}, the rhombohedral magnetostriction constant λ_{111} decreases with doping of Ga into Fe, and λ_{111} changes sign when the cubic anisotropy changes sign at 20%. Magnetoelastic and magnetic anisotropies are related because both of them are the results of electron spin-orbital coupling. Measurements of magnetic anisotropy for bulk $Fe_{1-x}Ga_x$ using a vibrating sample magnetometer (VSM) [6] show that cubic anisotropy drops when *x* increases and that anisotropy is almost zero when *x* reaches 20%.

When magnetoelastic $Fe_{1-x}Ga_x$ is deposited onto the non-magnetoelastic ZnSe substrate, there will be a biaxial strain generated at the interface due to the lattice mismatch. Because of this biaxial strain (and interface diffusion), magnetic anisotropies are expected to change. If this biaxial strain has an anisotropic relaxation in different directions, additional magnetic anisotropy energy will be generated because the magnetoelastic energy contribution will be different in the two directions. When placed in magnetic fields, a field dependent anisotropy energy term will be generated since different field strengths will generate different stresses in the material.

Angle dependent ferromagnetic resonance (FMR) can measure anisotropy fields in full angles and show anisotropy forms and magnitudes explicitly. We have used X-

band (9.4 GHz) and Q-band (34.8 GHz) FMR to measure the magnetic anisotropy of single crystal $Fe_{1-x}Ga_x$ thin films deposited onto ZnSe(100) and ZnSe(110) surfaces. For different microwave frequencies, the resonance occurs at very different magnetic fields. Magnetic field dependent anisotropy can be measured using different FMR spectra acquired at different frequency and comparisons between them will show the field dependence of anisotropy constants.

Introduction to the Samples

GaAs and ZnSe are semiconductors in cubic zincblende structure. GaAs cleaves along {110} planes. The lattice constant of α–Fe (2.866 Å) is almost half that of GaAs (5.653 Å) and ZnSe (5.668 Å) as shown in Figure 4. The perfect lattice mismatch makes the epitaxial growth of α-Fe on Zinc blended GaAs and ZnSe possible. In 1980s, Prinz and Krebs reported that the high quality single crystal Fe films had been grown successfully on semiconductor GaAs, ZnSe, Si, Ge and the insulator MgO [9, 15-18]. Growth studies of 20 nm $Fe_{1-x}Ga_x$ films up to x=0.7 on these substrates results in single crystal bcc structures similar to pure Fe [19].

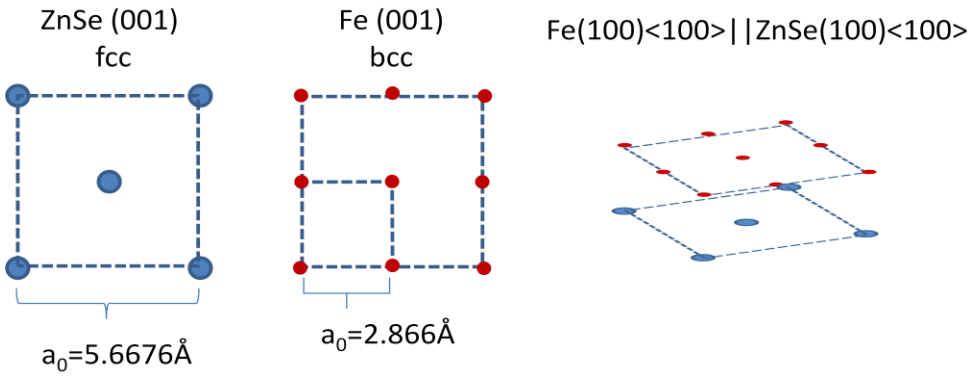

Figure 4: Lattice parameters of ZnSe(001) surface and BCC Fe(001) surface. Plot on the right shows the epitaxial growth of Fe(100)<100>||ZnSe(100)<100>.

Introduction to Elastic Energy and Magneto-elastic Energy

When a material is under stress, it will have deformation. The deformation of the material can be described by strain. There are two kinds of strains, normal strains and shear strains. Normal strains are strains that change the dimension of the material but do not change the directions of the material. The normal strain simply represents the fractional change in length of elements parallel to the ***x***, ***y***, and ***z*** axes respectively. For example the normal strain in the x direction is defined in Equation (1) and shown in Figure 5.

$$e_{xx} = \frac{\Delta x}{x} \tag{1}$$

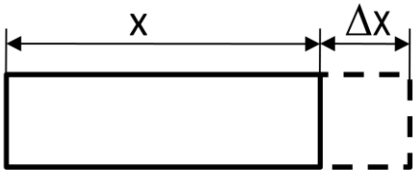

Figure 5: A scheme showing the definition of normal strain.

Shear strains result in the change of the principal axes directions. Shear strains are defined in terms of the changes in angles between axes, which is shown in Equation (2) and illustrated in Figure 6.

$$e_{xy} = \frac{1}{2}\left(\frac{\Delta x}{y} + \frac{\Delta y}{x}\right) \tag{2}$$

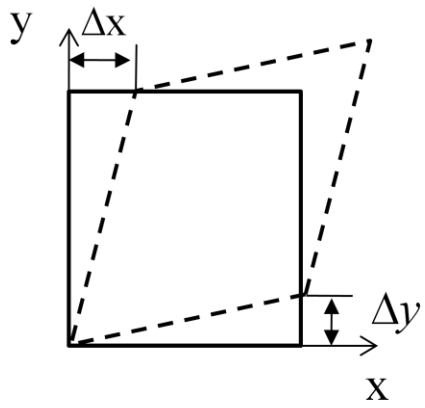

Figure 6: A scheme showing the definition of shear strain.

When the system is under strain, the energy associated with the change of dimensions or directions from its equilibrium position are called elastic energy. For a cubic system, the elastic energy can be written as:

$$U = \tfrac{1}{2}C_{11}(e_{xx}^2 + e_{yy}^2 + e_{zz}^2) + \tfrac{1}{2}C_{44}(e_{yz}^2 + e_{zx}^2 + e_{xy}^2) + C_{12}(e_{yy}e_{zz} + e_{zz}e_{xx} + e_{xx}e_{yy}) \quad (3)$$

where the C are the elastic stiffness constants and the e are the directional strains with e_{xx}, e_{yy} and e_{zz} the normal strain, e_{xy}, e_{yz} and e_{zx} the shear strain.

Some magnetic materials generate a mechanical deformation when placed in a magnetic field. These kinds of materials are called magneto-elastic materials. The deformation arises from spin-orbit coupling. When a magnetic field is applied, the spin direction will change. The change of spin direction will then cause the orbital change due to spin-orbital coupling, which causes the crystal to deform. Contrarily, a stress or strain will change the preferred magnetization direction. This inverse effect is called the inverse joule effect, or stress induced anisotropy. The magneto-elastic effect and the inverse joule effect are demonstrated in Figure 7.

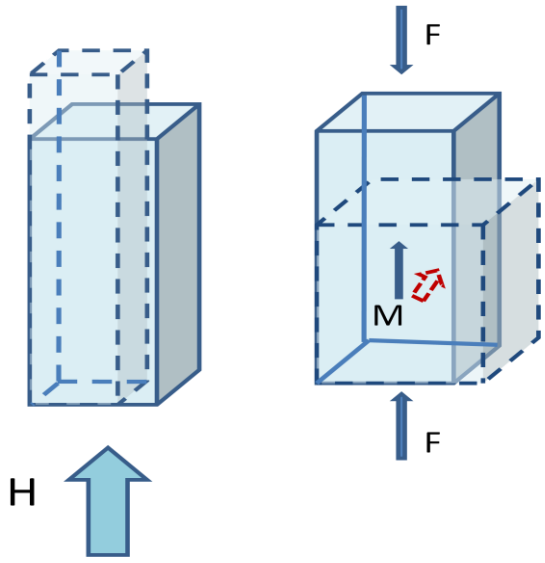

Figure 7: Magnetostrictive material responses under magnetic field or force. The left panel shows that the material undergoes a strain deformation when placed in a magnetic field. The right panel shows that the magnetic moment will change direction if a strain is generated in a material.

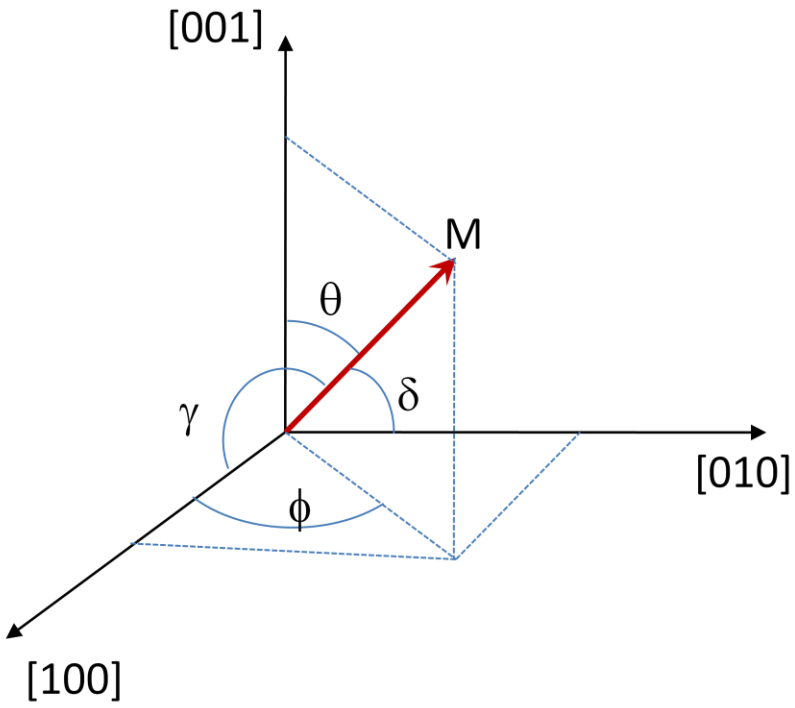

Figure 8: Coordinate system and angles for magnetization M.

The coupling between the magnetization direction and the mechanical deformation can be phenomenologically expressed using the magneto-elastic energy density. B is the coupling coefficients between the strains e_{ij} and the direction of magnetization given by α_{ij}. The magneto-elastic energy density in the cubic crystal is:

$$E_{me} = B_1(\alpha_1^2 e_{xx} + \alpha_2^2 e_{yy} + \alpha_3^2 e_{zz}) + B_2(\alpha_1\alpha_2 e_{xy} + \alpha_2\alpha_3 e_{yz} + \alpha_3\alpha_1 e_{zx}) \quad (4)$$

where B_1 is tetragonal magneto-elastic coupling constant, B_2 is rhombohedral magneto-elastic coupling constant, and α are the magnetization directions with $\alpha_1 = \cos\gamma = \sin\theta\cos\phi$, $\alpha_2 = \cos\delta = \sin\theta\sin\phi$, and $\alpha_3 = \cos\theta$. Angles are defined in Figure 8.

Another magnetostrictive parameter frequently used is magnetostriction constant λ. It is defined as $\Delta\ell/l$, where $\Delta\ell$ is the saturation strain in magnetic fields as shown in Figure 9. λ_{100} is the magnetostriction in the [100] direction when magnetic field is applied in the [100] direction. λ_{111} is the magnetostriction in the [111] direction when magnetic field is also in the [111] direction.

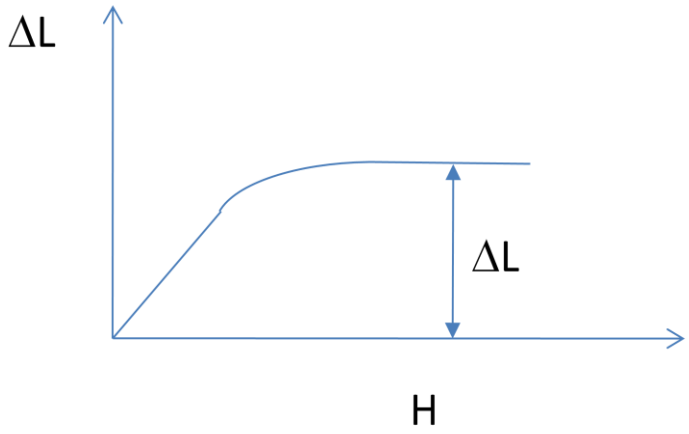

Figure 9: Definition of magnetostriction constant λ.

Introduction to Magnetic Anisotropy Energy

Magnetic anisotropy energy is an important parameter for magnetic materials. Magnetic anisotropy energy determines how easy it is to flip a magnetic moment from one direction to another. It determines how well a magnetic moment can stay in one direction and how hard it is to change the magnetic moment's orientation to another direction. For example, in memory devices, once we write information we would like to keep the moment in one direction until we want to change it. Then the magnetic anisotropy energy competes with thermal energy to keep the magnetic moment in that direction.

The direction, in which the magnetic moment prefers to point without an external field, is the easy-axis direction and is a minimum in the magnetic energy. The direction which will cost the most external work to make the moment point is the hard axis. In the hard axis direction, the magnetic energy is the maximum.

The energy surface can be used to visualize the magnetic anisotropy forms. The energy density surface plots the magnetic energy of a magnetic moment pointed in that direction. For example, Figure 10 shows an energy density surface of a uni-axial anisotropy. In the [100] direction, the energy surface shows a minimum, which means it is an easy axis. While in the (100) plane, the energy surface is maximum, which means the magnetic anisotropy has a hard plane in the (100) plane.

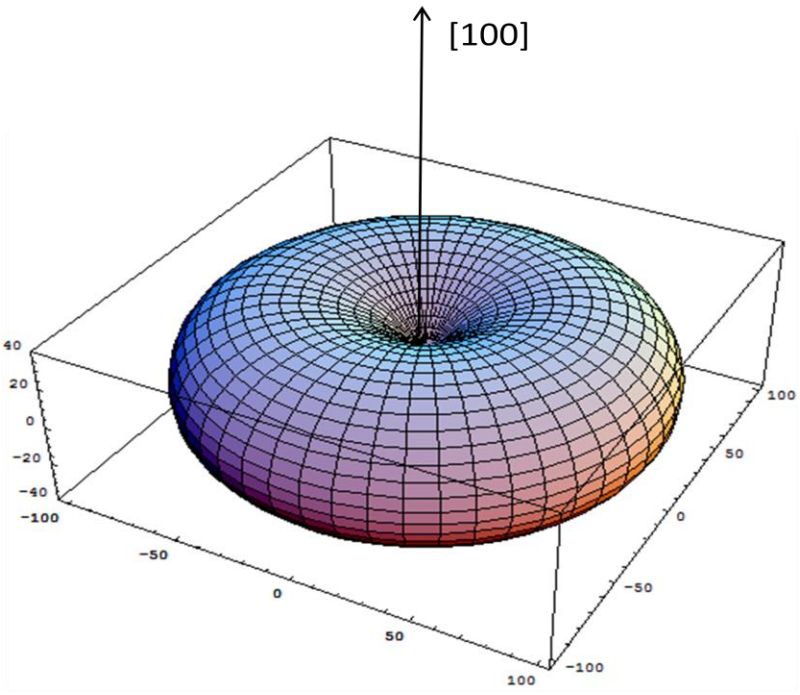

Figure 10: Plot of uniaxial magnetic anisotropy energy density surface.

Physical Origins of Magnetic Anisotropy

The magnetic anisotropy comes from the asymmetry of the material, either microscopically or macroscopically. Microscopic asymmetry comes from crystal fields in the material, directional chemical bondings *etc*. Macroscopic asymmetry comes from the shape of crystal, strain in the material, boundary of the material *ect*.

Crystalline Anisotropy Energy: Magnetocrystalline anisotropy originates from the coupling of the spin part of the magnetic moment to the electronic orbital shape and orientation (spin-orbital coupling) as well as in the chemical bonding of the orbitals on a given atom with their local environment (crystalline electric field).

The crystal field is an electric field derived from neighboring atoms in the crystal. Each atom's orbital has its own shape. For example, the d-orbitals are often grouped as e_g and t_{2g} orbitals, whose shapes are shown in Figure 11.

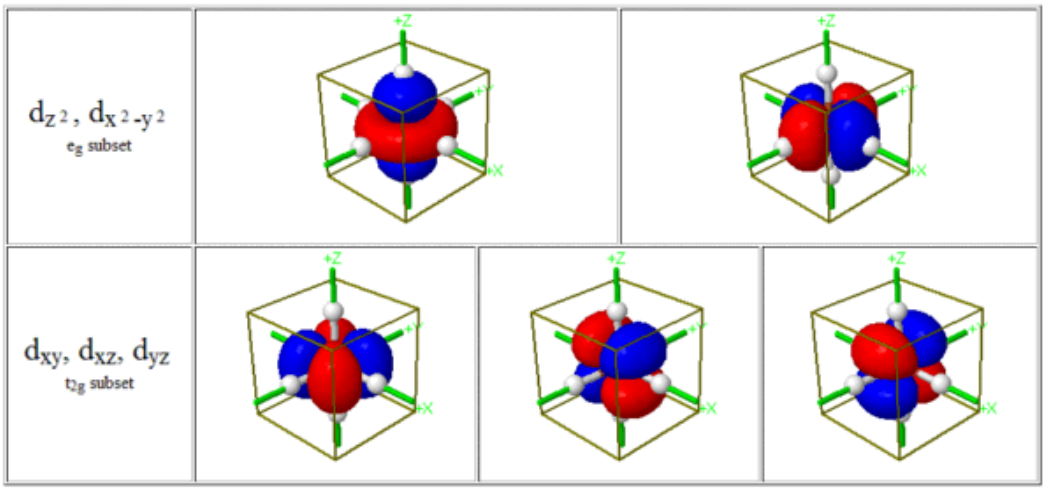

Figure 11: Electron distribution shapes for different d orbitals.[20]

The orbital shapes are distributions of electrons. With these different electron orbital, atoms interact with their surroundings differently, and generate different magnetic anisotropies. For example, with crystal electric field shaped as in Figure 12, if the atomic orbital has zero angular moment, the orbital can take on any orientation with respect to the crystal no matter what the symmetry of the crystal field. Furthermore, since the coupling between the direction of the spin and the orbital angular momentum is zero, the spin magnetic moment is free to assume any direction in space dictated by other factors such as applied field. If the orbital has a non-zero projection in the Z direction, which is $\langle lz \rangle$ is not zero, they may assume any orientation in a spherically symmetric crystal field, but only certain orientations will be preferred in crystal fields of lower symmetry.

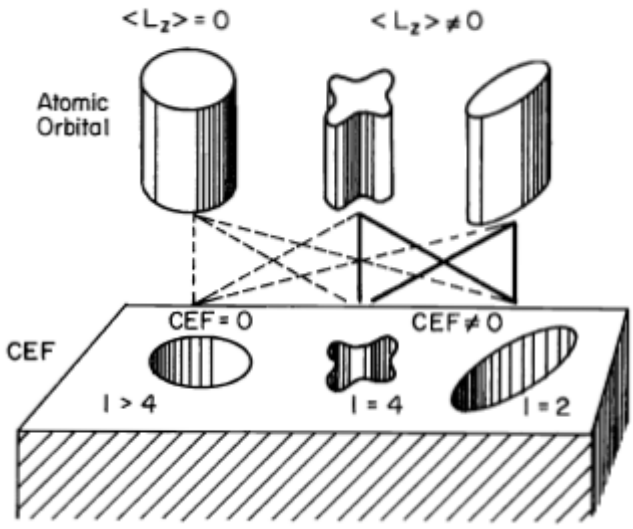

Figure 12: Crystal field shapes and atomic orbital shapes.[21]

Shape Magnetic Anisotropy[22]: Shape anisotropy originates from the anisotropic demagnetization field. Demagnetization field comes from the surface un-compensated free poles that emit field lines through the material, this field line will be opposite to the magnetic field. The demagnetization fields are proportional to the magnetization and can be defined as:

$$\begin{aligned} B_x &= -N_x M_x \\ B_y &= -N_y M_y \\ B_z &= -N_z M_z \end{aligned} \tag{7}$$

where N_x, N_y and N_z are the demagnetization factors. The components of the internal magnetic field B_i in an ellipsoid can be written as:

$$\begin{aligned} B_x^i &= B_x^0 - N_x M_x \\ B_y^i &= B_y^0 - N_y M_y \\ B_z^i &= B_z^0 - N_z M_z \end{aligned} \tag{8}$$

where B^0s are the fields without demagentic fields. For sphere, the de-magnetic factors are $N_x=N_y=N_z=4\pi/3$ in cgs unit. For a thin film in the x-y plane the de-magnetic field factor N_z is -4π.

Surface Magnetic Anisotropy: Surface anisotropy arises from the broken symmetry of atoms sitting at the surface. In the bulk material, orbital moments can have 3-d distribution. At the surface, electron momentum components perpendicular to the surface have been significantly reduced because electrons have reduced probability of being found outside the surface. This will generate orbital momentum perpendicular to the surface. If the spin-orbital interaction is strong, the spin moment perpendicular to the surface will also be increased.

Magneto-Elastic Contribution to Anisotropy Energy: For a magnetostrictive material, we inspect the energy terms related to magnetic moment, $E = E_{me} + E_{an} + E_{static}$. It is shown that the energy density depends on the magnetization direction, which means the magnetoelastic term has built-in magnetic anisotropy energy. If the magnetoelastic energy contributes to anisotropy energy, the magnetoelastic energy can be written as:

$$E_{ME} = \Delta K_u + \Delta K_1 + \cdots \tag{9}$$

For our thin film system where the thin film is clamped onto the substrate as shown in Figure 13, if there is no strain relaxation and $e_{xx}=e_{yy}=e_{||}$, $e_{zz}=e_{\perp}$, $e_{xy}=e_{yz}=e_{zx}=0$, magnetoelastic energy term is written as:

$$\begin{aligned} E_{me} &= B_1(\alpha_1^2\varepsilon_{||} + \alpha_2^2\varepsilon_{||} + \alpha_3^2\varepsilon_{\perp}) \\ &= B_1(\alpha_1^2\varepsilon_{||} + \alpha_2^2\varepsilon_{||} + \alpha_3^2\varepsilon_{||}) + B_1\alpha_3^2(\varepsilon_{\perp} - \varepsilon_{||})) \\ &= B_1\varepsilon_{||} + B_1\alpha_3^2(\varepsilon_{\perp} - \varepsilon_{||}) \end{aligned} \tag{10}$$

where α are the directional cosines of the magnetization along the three coordinate axes. It should be noted that the first term does not depend on the magnetization direction. If α_3 is replaced with $\cos\theta$, the last term will be equivalent to a uni-axial term in the z direction, which is an out-of-plane uniaxial energy. So the biaxial strain does not cause the cubic anisotropy to change. But if the strain e_{xx} is not equal to e_{yy}, an in-plain uniaxial anisotropy will be generated with axes in the x and y directions.

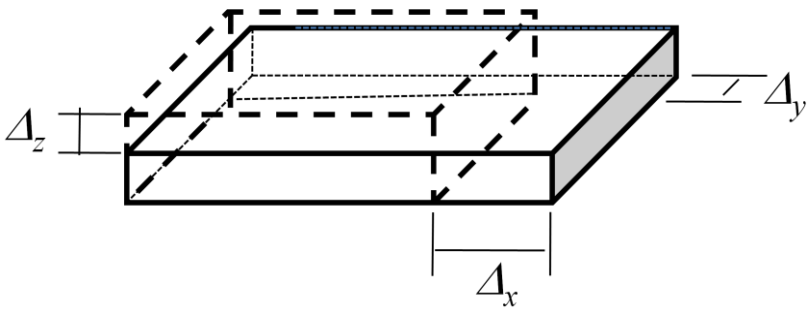

Figure 13: Compressive biaxial strain in a system.

For a thin film with a shear strain ε_{xy} in the x and y direction, and no shear strain in the z direction as shown in Figure 14, the magnetoelatic energy term can be written as:

$$\begin{aligned} E_{me} &= B_2(\alpha_1\alpha_2\varepsilon_{xy} + \alpha_2\alpha_3\varepsilon_{yz} + \alpha_1\alpha_3\varepsilon_{xz}) \\ &= B_2(\alpha_1\alpha_2\varepsilon_{xy}) \\ &= B_2\varepsilon_{xy}\sin\theta\cos\phi\sin\theta\sin\phi \\ &= B_2\varepsilon_{xy}\,\tfrac{1}{2}\sin(2\phi)\sin^2\theta \end{aligned} \tag{11}$$

where θ is equal to $\pi/2$ for magnetization in the film plane, $sin\theta$ goes to 1. The shear strain in the film plane results in an in-plane uniaxial term with axes in the [110] and [1-10] directions.

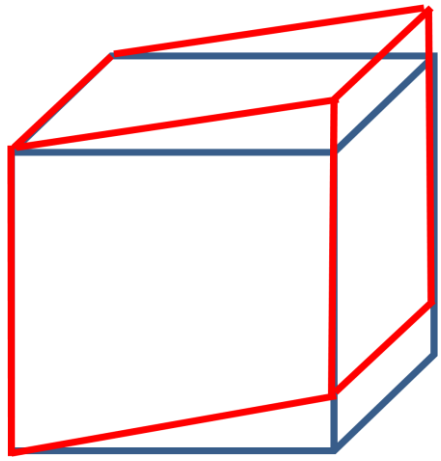

Figure 14: Shear strain in a system.

Quantify Magnetic Anisotropy Energy

A quantitative measurement of the strength of magnetic anisotropy is the field, called the anisotropy field, *Ha*, which is the field needed to saturate the magnetization in the hard direction. The energy per unit volume needed to saturate a material in a particular direction is given by a generalization of Equation (12):

$$u_a = \int_0^{Ms} H(M)dM(erg/cm^3). \tag{12}$$

As has been discussed previous, magnetic anisotropy energy can be represented using a 3-D surface, where each point on the surface represents the energy needed to move the magnetic moment to that direction.

Uniaxial Magnetic Anisotropy: Uniaxial anisotropy energy means that there is only one easy or hard axis direction. It is often expressed as :

$$u_a = \frac{U_0}{V} = \sum_n K_{un} \sin^{2n}\theta = K_{u0} + K_{u1}\sin^2\theta + K_{u2}\sin^4\theta + \cdots \tag{13}$$

K_{u0} is the zero order uniaxial anisotropy and does not depend on angle, so it has no contribution for anisotropy energy. K_{u1} is the second order uniaxial magnetic anisotropy, Ku1 >0 means an easy axis in the θ=0 direction while K_{u1}<0 means a hard axis in the θ=0 direction as shown in Figure 15. K_{u2} is the fourth order uniaxial magnetic anisotropy.

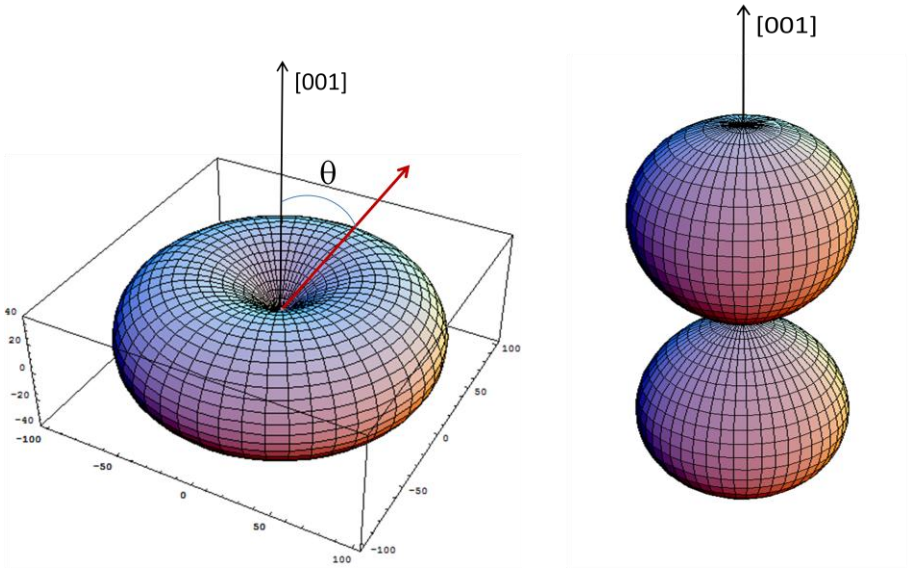

Figure 15: Uniaxial magnetic anisotropy. In the left panel, it is easy axis in the [001] direction. In the right panel, it is hard axis in the [001] direction.

Cobalt has uniaxial anisotropy with K_{u1}>0, which means an easy axis is in the *c* direction. The de-magnetic anisotropy for a thin film is a K_{u1}<0 uniaxial anisotropy. This means that the axis perpendicular to the film plane direction is a hard axis and magnetic moment prefers to align in the film plane, this is the reason why most magnetic thin films

have in-plane magnetic moment. Surface anisotropy usually is normal to the film plane with $K_{u1}>0$, causing the magnetic moment align perpendicular to the film plane.

Cubic Anisotropy Energy: In cubic materials, the magnetic anisotropy is also a cubic. Cubic anisotropy means that <100> directions have equivalent energies. Cubic anisotropy can be expressed as:

$$u_a = K_0 + K_1(\alpha_1^2\alpha_2^2 + \alpha_2^2\alpha_3^2 + \alpha_3^2\alpha_1^2) + K_2(\alpha_1^2\alpha_2^2\alpha_3^2) \tag{14}$$

Again, the αs are the directional cosines of the magnetization along the three coordinate axes as shown in Figure 8. For $K_1>0$, the <100> direction is easy axis direction while for $K_1<0$, the <100> direction is the hard axis direction, as shown in Figure 16. K_2 is a higher order cubic anisotropy, with $K_2>0$, the <111> direction is the hard-axis direction, while for $K_2<0$, the <110> direction is the hard-axis driection.

Cubic crystal structures like BCC or FCC normally will have cubic magnetic anisotropy. BCC Fe has cubic anisotropy with $K_1>0$, which means <100> are magnetic easy directions and <111> are magnetic hard directions, [011] is an intermediate direction. For FCC Ni, whose K_1 is less than 0, <001> are hard axes and <111> are easy axes, again, the <110> direction are the intermediate direction.

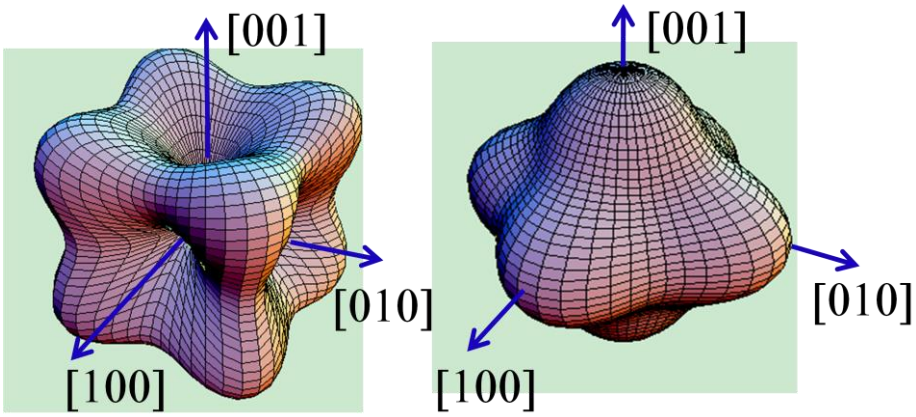

Figure 16: Cubic magnetic anisotropies. In the left panel, K_1 is positive. In the right panel, K_1 is negative.

Ways to Determine Anisotropy Energy

For bulk materials, magnetic anisotropy measurements are often made using a torque magnetometer, VSM (vibrating sample magnetometer), ferromagnetic resonance, or Mossbauer spectroscopy.

For magnetic particles, magnetic anisotropy can be derived from ACMS measurement, which has been described in detail by Damon Resnick [23].

Introduction to the Bulk Material $Fe_{1-x}Ga_x$

Magnetostriction Properties

BCC Fe has small magnetostiction coefficients. The tetragonal magnetostiction λ_{100} for BCC Fe is 20 ppm, and the rhombohedral magnetostriction λ_{111} is 16 ppm. It has been found that with the addition of some elements, such as Al, Cr, and Ga, the magnetostrition λ_{111} decreases and λ_{100} increases. Clark [3] first reported the 10 fold increase of λ_{100} in Fe-Ga alloys. And the saturation field is as low as 150 Oe. Ga and Al

both have large solubility in Fe and retain BCC like symmetry both in disordered alloy form and in the ordered B_2 and $D0_3$ structures, so they are ideal elements to make large magnetostiction alloys.

For $Fe_{1-x}Ga_x$, magnetostriction shows a very interesting Ga concentration dependent property as shown in Figure 3. As Ga concentration increases, tetragonal magnetostriction λ_{100} increases and reaches a peak around 19% Ga, and it decreases but reaches another peak at around 27% Ga [3]. The $Fe_{0.81}Ga_{0.19}$ was named Gafenol (Gallium, Fe and naval ordinance lab). The existence of the two magnetostriction constant peaks has different reasons. According to Kittel [22], $\lambda_{100}=-3b_1/2(c_{11}-c_{12})$. From Table 1, we see that b_1 increases as doping of Ga till 24%, and $(c_{11}-c_{12})/2$ suddenly drops at 24%. Then the first peak of λ_{100} is attributed to the increase of $|b_1|$ up to 19%, and the second peak is attributed to the softening of the shear elastic constant $(c_{11}-c_{12})/2$ happening at 24% of Ga and extending to 27% Ga.

	$(c_{11}-c_{12})/2$ (GPa)	$(3/2)\lambda_{100}$ ($\times 10^{-6}$)	b_1 (MJ/m^3)
Fe (Ref. 9)	48	30	−2.9
5.8% Ga	40	79	−6.3
13.2% Ga	28	210	−11.8
17% Ga	21	311	−13.1
18.7% Ga	19.7	395	−15.6
24.1% Ga	9.4	270	−5.1
27.2% Ga	6.8	350	−4.8

Table 1: Room temperature tetragonal magneto-elastic constants for $Fe_{1-x}Ga_x$ [3].

Different from λ_{100}, the rhombohedral magnetostriction λ_{111} decreases with the doping of Ga into Fe, as shown in Figure 17. λ_{111} changes sign when cubic anisotropy

changes sign at 20%. According to Kittle [22], $\lambda_{111}=-b_2/3c_{44}$. From Table 2, b_2 changes sign at 20% Ga, which causes λ_{111} to change sign at 20%. Unlike λ_{111}, λ_{100} reaches a peak at the same Ga concentration, so Clark concluded that an ordering transition happened at this concentration.

	c_{44} (GPa)	$(3/2)\lambda_{111}$ ($\times 10^{-6}$)	b_2 (MJ/m^3)
Fe (Ref. 9)	116	−32	7.4
8.6% Ga	119	−27	6.4
13.2% Ga	~119	−24	5.7
20.88% Ga	~120	42	−10.1
28.63% Ga	~120	61	−14.6

Table 2: Room temperature rhombohedral magneto-elastic constants for $Fe_{1-x}Ga_x$.

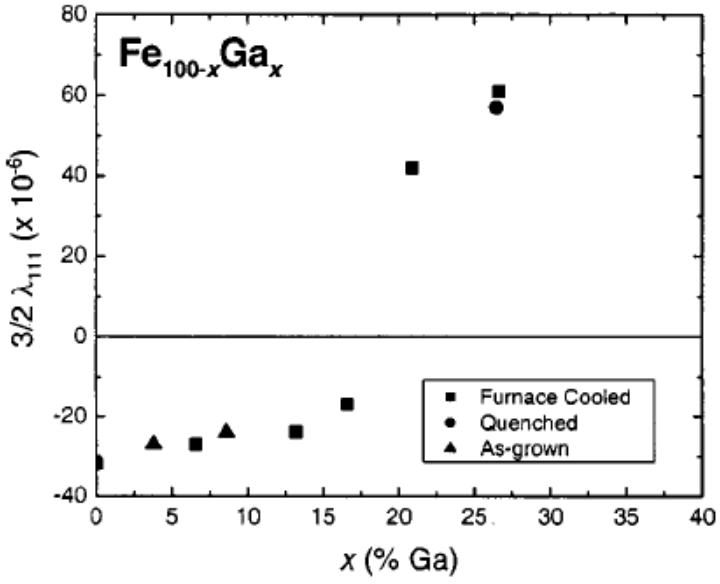

Figure 17: Rhombohedral magnetostriction constant λ_{111} as function of Ga concentration at room temperature.[3] Reprinted with permission from Journal of Applied Physics, **93**, A. E. Clark, Hathaway, K. B., Wun-Fogle, M., Restorff, J. B., Lograsso, T. A., Keppens, V. M., Petculescu, G., Taylor, R. A., Copyright [2003], American Institute of Physics.

Crystal Structure

Bulk $Fe_{1-x}Ga_x$ alloys undergo multiple phases as the growth temperature and Ga concentration change. Ikeda [24] examined the equilibria phases of the Fe-Ga binary system. They prepared the sample using induction melting in an alumina crucible under argon atmosphere using Fe and Ga. Samples were annealed at 1100 ºC for 30 minutes followed by quenching in ice water. The phases of the samples were examined by transmission electron microscopy (TEM), scanning electron microscopy (SEM) and energy dispersion spectroscopy (EDS). Phase stability was examined using Concentration Gradient Method (CGM). Transition temperatures from order to disorder, and from paramagnetic to ferromagnetic were investigated using differential scanning calorimetric (DSC) method. Figure 18 shows the phase diagram of the Fe-Ga system and Figure 19 shows the structure for the different phases.

The structure change in the bulk material, has been theoretically investigated to explain the extraordinary magnetoelastic terms in $Fe_{1-x}Ga_x$ [26]. The lattice constants of B2, $L1_2$ and $D0_3$ were optimized through total energy minimizations. $L1_2$ is found to be the ground state while $D0_3$ is the metastable state and B2 is the unstable state under tetragonal distortion. The energy of the B2 phase decreased monotonically when the B2 lattice elongated along the z axis. However, for real materials, atoms have a much higher degree of freedom for random disorder, so it is possible to have the B2-like structure locally in samples as a secondary phase. The calculated magnetic anisotropy energy with change of lattice strain in the *Z* axis showed that $L1_2$ and $D0_3$ have negative λ_{100} while B2 has positive λ_{100} as shown in Figure 20.

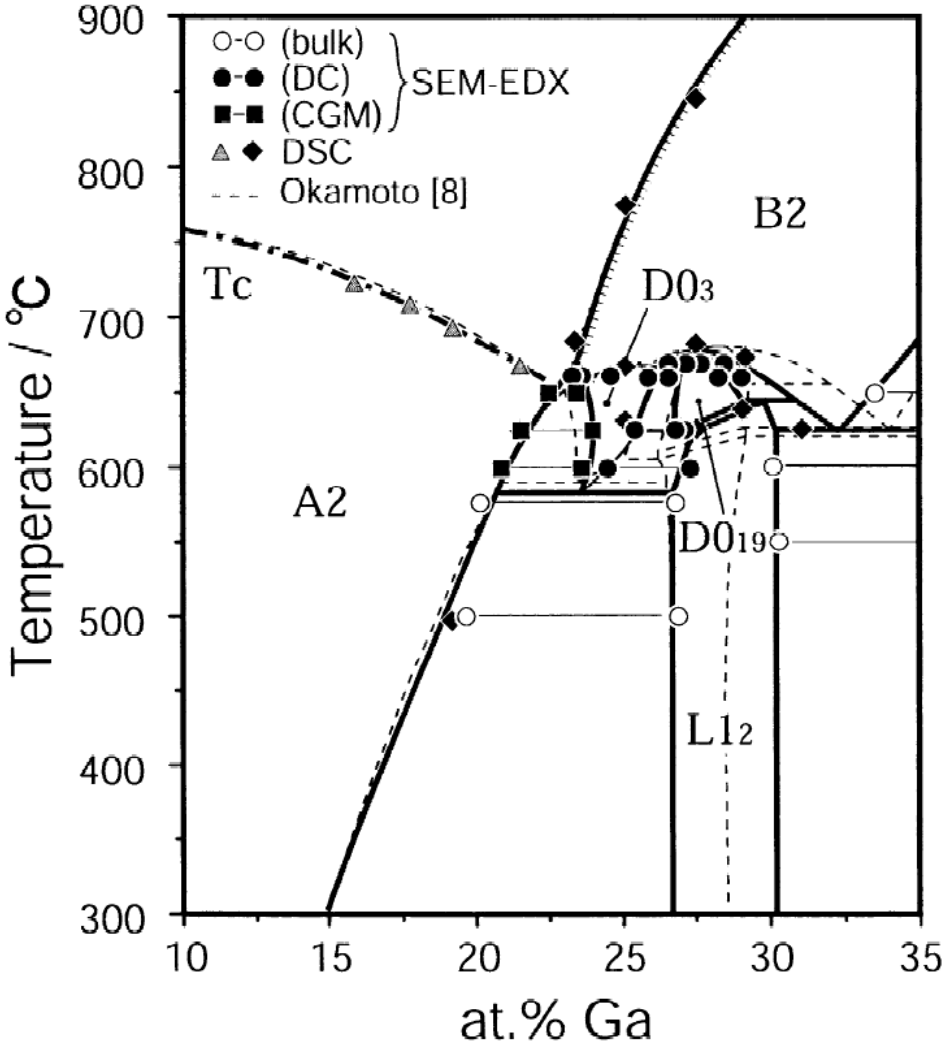

Figure 18: Experimental phase diagram of the Fe-rich portion in Fe-Ga system [24, 25]. Reprinted from Journal of Alloys and Compounds, **347**, O. Ikeda, R. Kainuma, I. Ohnuma, K. Fukamichi, and K. Ishida,Phase equilibria and stability of ordered b.c.c. phases in the Fe-rich portion of the Fe-Ga system, p.198, Copyright (2002), with permission from Elsevier.

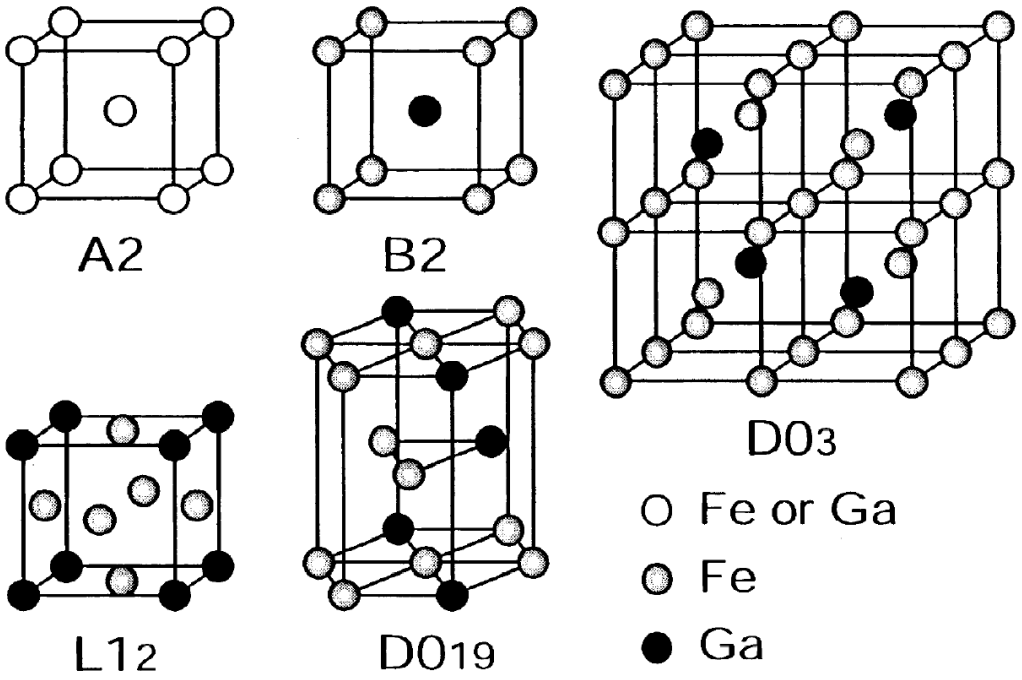

Figure 19: The crystal structures of A2, B2, $D0_3$, $L1_2$ and $D0_{19}$ for Fe-Ga alloy. Reprinted with permission from Journal of Applied Physics **91**, R. Wu, 7358, copyright (2002)

The theoretical results show that even though B2 structure is unstable it is still responsible for the large positive magnetostriction in the Fe-Ga alloys. When the crystal structure changed from $L1_2$ or $D0_3$ to B2, the sign of λ_{100} would change.

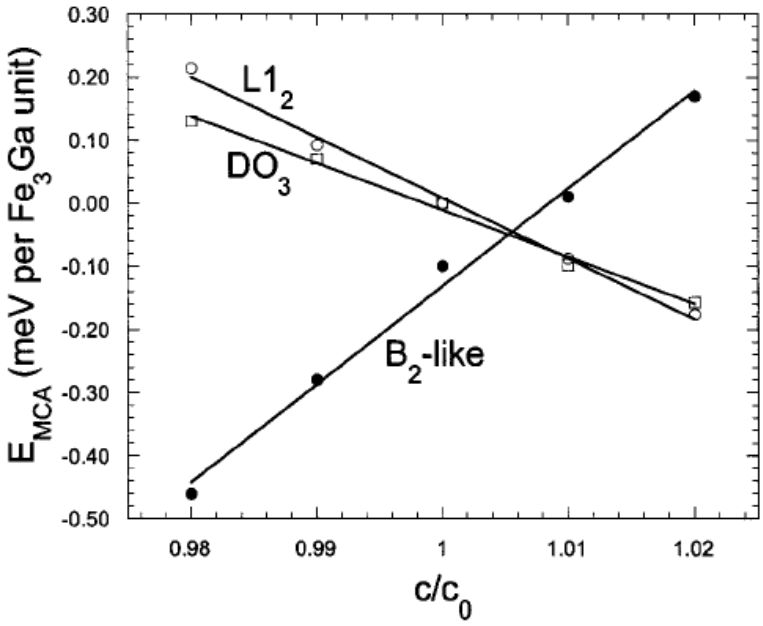

Figure 20: Calculated strain-induced magneto-crystalline anisotropy energies of Fe_3Ga. [26] Reprinted with permission from Journal of Applied Physics **91**, R. Wu, 7358, copyright (2002)

Lattice Constants Versus Ga Concentration

Lattice parameter a as a function of Ga concentration for BCC FeGa was determined by Borrego [5]. They prepared the sample by arc-melting pure Fe and Ga in an Edmund-Buhler high vacuum arc-melting system and used X-ray diffraction (XRD) to get the lattice constant a. They showed that the lattice constant of BCC Fe increased as Ga addition which can be seen from Figure 21. The lattice constant for FeGa can be expressed as:

$$a = 0.2869 + 0.0002y \quad \text{(nm)} \tag{5}$$

Where a is the lattice constant, and y is the Ga concentration (at %). Additional weak peaks due to possible occurrence of $D0_3$ ordering are not observed. This might be due to the fact that Fe and Ga have similar scattering factors.

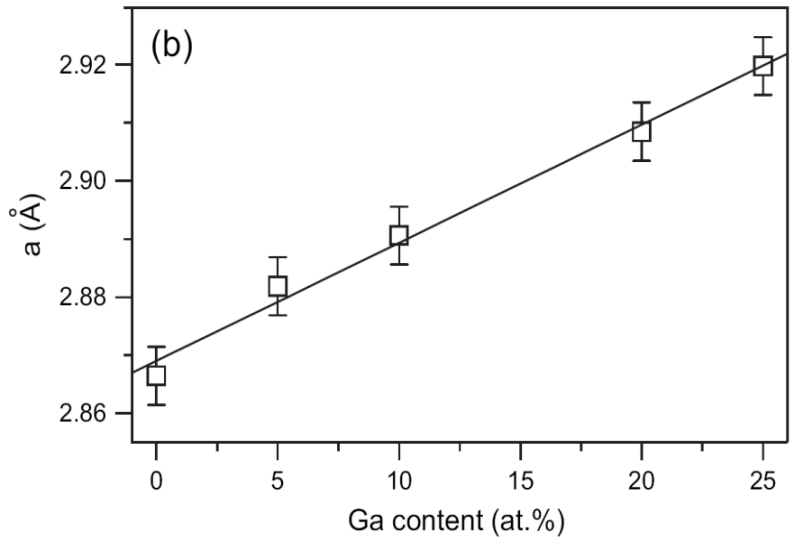

Figure 21: Lattice parameter a of the BCC phase of FeGa alloys as a function of Ga concentration. [5] Reprinted from Intermetallics, **15**, .M. Borrego, J.S. Blázquez, C.F. Conde, A. Conde, S. Roth, Structural ordering and magnetic properties of arc-melted FeGa alloys, p. 193-200, Copyright (2007), with permission from Elsevier.

Magnetic Properties

The magnetic properties of Fe-Ga alloy have been measured for its magnetic moment, Curie temperature, and magnetic anisotropies. The magnetic moment of Fe-Ga alloy has been measured using VSM and shows decreasing with the doping of Ga, and the moment per Fe also decreased with the doping of Ga. [5] At low Ga content up to 20 at %, the moment per Fe can be expressed as:

$$\langle \mu_{Fe} \rangle = 2.24(3) - 0.004(3)y \ [\mu_B]. \quad (6)$$

With additional Ga doping, Fe moment dropped quickly as shown in Figure 22. The sudden drop of Fe moment suggests a change of structural ordering in the binary alloy.

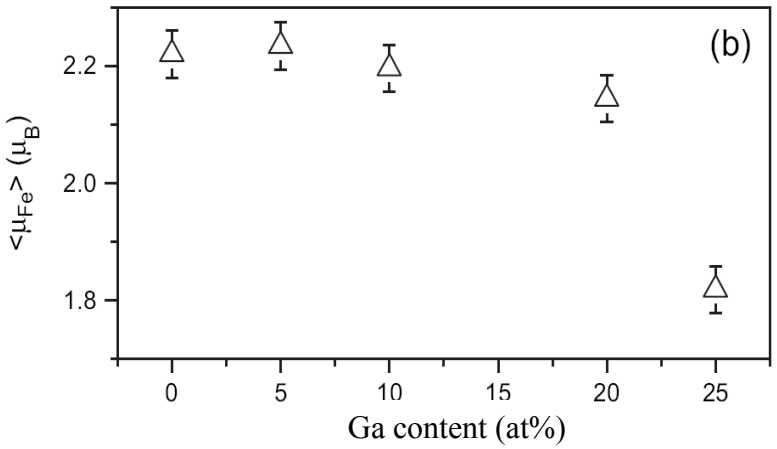

Figure 22: Composition dependence of average magnetic moment per Fe atom at 300 K for FeGa alloys at different Ga concentration.[5] Reprinted from Intermetallics, **15**, .M. Borrego, J.S. Blázquez, C.F. Conde, A. Conde, S. Roth, Structural ordering and magnetic properties of arc-melted FeGa alloys, p. 193-200, Copyright (2007), with permission from Elsevier.

The Curie temperature T_c also dropped monotonically with Ga content as shown in Figure 23. Curie temperature dropped from 1050 K to 700 K as the alloy went from pure Fe to 25 at % of Ga content.

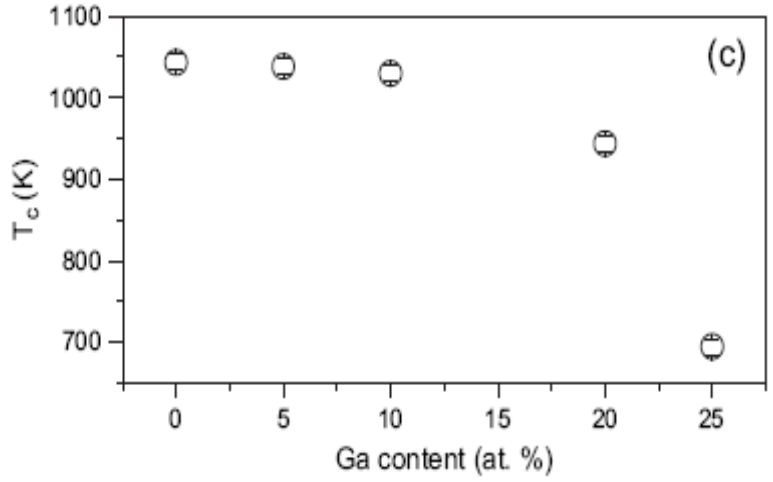

Figure 23: Curie temperature, *Tc*, of Fe-Ga alloys as function of Ga concentration.[5] Reprinted from Intermetallics, **15**, .M. Borrego, J.S. Blázquez, C.F. Conde, A. Conde, S. Roth, Structural ordering and magnetic properties of arc-melted FeGa alloys, p. 193-200, Copyright (2007), with permission from Elsevier.

Magnetic anisotropy of bulk Fe-Ga alloys has been measured using vibrating sample magnetometry (VSM) [6]. The anisotropy energy is a purely cubic term and there is no uniaxial energy showing up in the bulk Fe-Ga materials. The cubic magnetic anisotropy K_1 increased with doping of Ga but was immediately followed by a decrease and K_1 decreased to zero at around 20% Ga doping. The crossing anisotropy at 20% means that there is no directional preference for the magnetic moment in the material and all the directions become magnetically equivalent. In the VSM measurements, the magnetization versus field curves for <110> and <111> directions are identical. They attributed these to the K_2 term as defined earlier. The K_1 and K_2 values are plotted in Figure 24 and Figure 25, respectively.

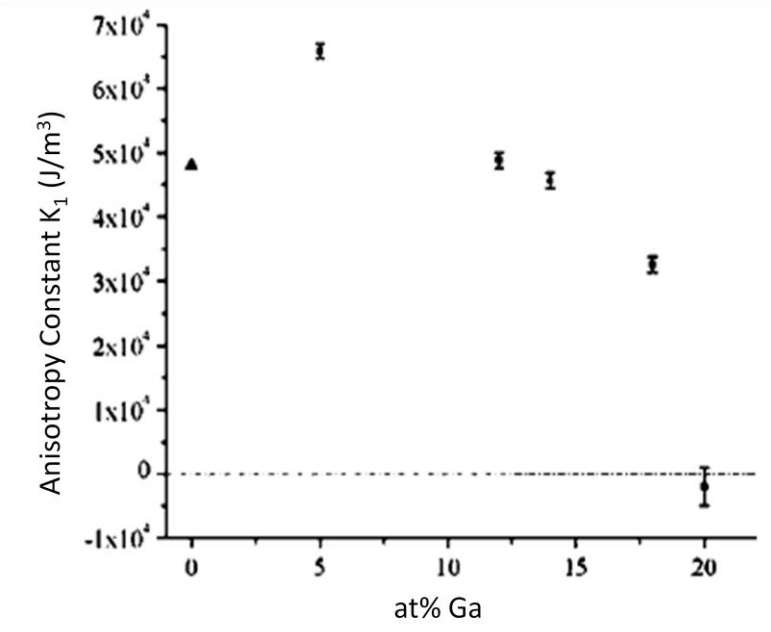

Figure 24: K_1 versus Ga concentration for $Fe_{1-x}Ga_x$.[6] Reprinted with permission from Journal of Applied Physics, **95**, S. Rafique, J. R. Cullen, M. Wuttig, and J. Cui, Copyright [2004], American Institute of Physics.

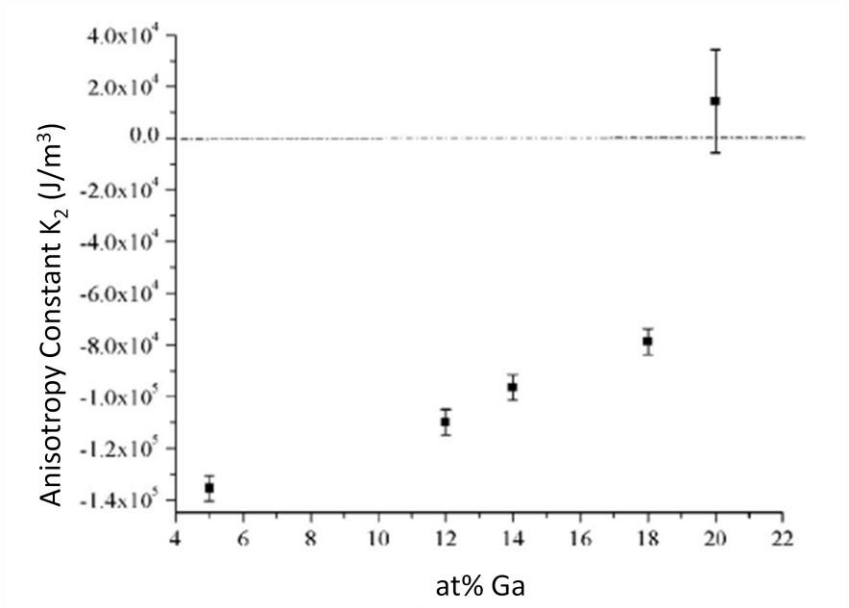

Figure 25: K_2 versus Ga concentration for $Fe_{1-x}Ga_x$.[6] Reprinted with permission from Journal of Applied Physics, **95**, S. Rafique, J. R. Cullen, M. Wuttig, and J. Cui, Copyright [2004], American Institute of Physics.

GaAs and ZnSe Substrate Characteristics

GaAs is a widely used semiconductor second only to Si. GaAs and ZnSe are semiconductors both in the cubic zincblende structure, which can be thought of as an FCC lattice of Ga/Zn with another FCC lattice of As/Se displaced by $\sqrt{3}/4$ of the lattice constant in the [111] direction (see Figure 26). The lattice constant of GaAs is 5.653 Å and the lattice constant of ZnSe is 5.669 Å. GaAs is often called a group III-V semiconductor, because Ga has 3 valence electrons and Arsenic has 5 valence electrons. The Ga-As bonding is mostly covalent and partly ionic, because the electronegativites are smaller for metal Ga (1.81) than non-metal As (2.18). ZnSe is often called a group II-VI semiconductor, because Zn has 2 valence electrons and Se has 6 valence electrons. It is

an intrinsic semiconductor with a band gap of 2.70 eV at 25 ºC. The electronegativites are 1.65 for Zn and 2.55 for Se (the electronegativity for Fe is 1.8).

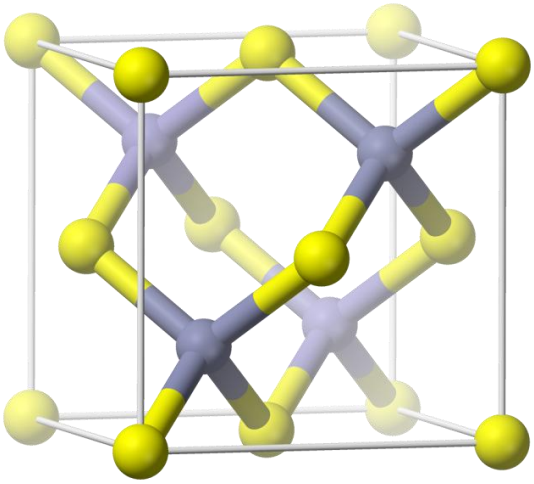

Figure 26: Zinc blend Structure of GaAs or ZnSe. Different colors represent different atomic types (Ga/Zn) or (As/Se).

GaAs cleaves along {110} planes and the cleavage plane contains an equal number of Ga and As atoms. Each surface atom has three nearest neighbors leaving one unpaired electron bond. No surface reconstruction on the surface has been observed. The surface termination consists of planar zigzag chains of alternating cations and anions. The surface structure of the (110) plane is shown in the right panel of Figure 27.

In contrast to (110) planes, the (100) planes are occupied with only one kind of atom, either cations or anions, termed Ga-rich or As-rich substrates. The surface atoms have two dangling bonds in either [110] or the [1-10] direction, depending on termination. The dangling bonds on Ga terminated (100) surfaces lie in the (1-10) plane while on As terminated surfaces they lie in the (110) plane. The surface structure of (100) is shown in the left panel of Figure 27. The surface undergoes a wide range of

reconstructions which involve significant surface atom rearrangement and modification of surface periodicity.

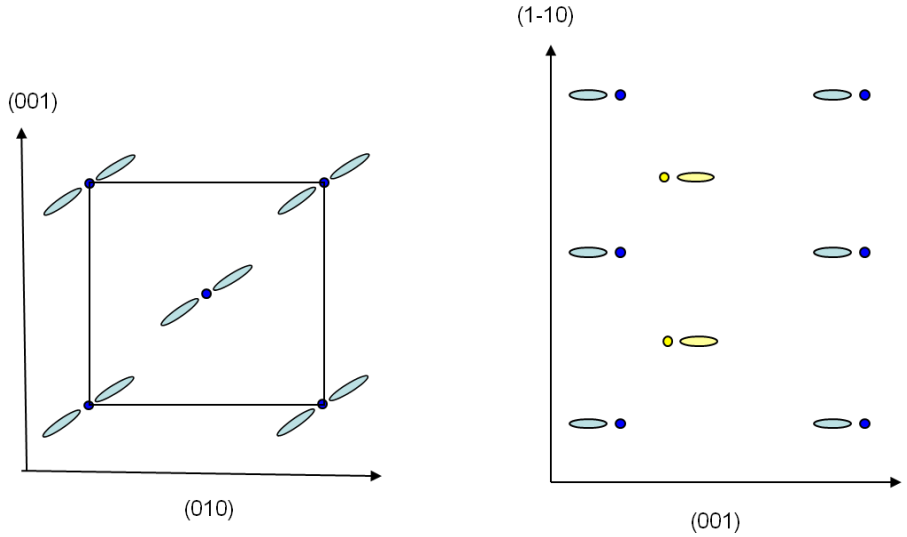

Figure 27: Surface terminations of Zinc blend structure. The left panel shows the surface termination of (001) surface. The blue atoms can be either Ga or As. The blue wings represent the bonding directions. The right panel shows the surface termination of (110) surface. The (110) surface consists of two kinds of atoms, which are represented by blue and yellow.

Tomiya [27] used AFM and TEM to investigate the surface morphology of ZnSe-related II-VI films grown by MBE. He found that the Se terminated surface had full coverage and was (2×1) reconstructed while Zn terminated surface only had half coverage and was c(2×2) reconstructed. Under group II Zn rich conditions with c(2×2) surface reconstruction, the process of roughening gives rise to periodic elongated corrugations aligned in the [1-10] direction. While under group VI Se rich conditions with (2×1) surface reconstruction, rounded grains are present at the surface instead of corrugated structures. The surface morphology is dependent on the VI/II ratio and growth temperature, but it is independent of the film strain [27].

Literature Review of $Fe_{1-x}Ga_x$ Grown on ZnSe and GaAs

In previous sections, we have reviewed the properties of bulk $Fe_{1-x}Ga_x$ and the properties of substrates GaAs and ZnSe. In this section, I will review the properties of $Fe_{1-x}Ga_x$ epitaxially grown on ZnSe and GaAs substrates beginning with the epitaxial growth of pure Fe.

Fe/GaAs(100)

This review about Fe/GaAs(001) follows the review paper written by Wastlbauer G. and Bland, J. A. C [8].

Growth Properties: On Ga-rich surfaces, Sano and Miyagama [28] used RHEED to investigate structure change for Fe deposited on sputter annealed GaAs(001)-(4×6). The RHEED signal decreased rapidly for the first monolayer of Fe and the low intensity remained till thickness reached 4ML, after which, the intensity increased and by 5.5 ML, the RHEED regained its intensity. They attributed these to the initial cluster formation followed by clusters coalescence and subsequent layer-by layer growth.

Monchesky [29] found that up to 2 ML Fe, the RHEED pattern showed coexistence of Fe and GaAs patterns. Zolfl [30] and Brockman [31] found coalescence between 3 ML and 4 ML, which is followed by quasi-layer-by-layer growth after 5 ML.

Bensch [32] found that RHEED pattern for GaAs disappeared after 0.5 ML of Fe but a clear Fe pattern appeared only after at least 2 ML of Fe. Their data also showed that ferromagnetic order and magnetic anisotropy set in at 2.5 ML. They concluded with amorphous growth in the beginning, followed by a crystalline growth around 2.5 ML.

The above comments suggested that the growth of Fe on Ga rich GaAs surfaces proceeded via nucleation of 3D islands and followed by quasi-layer-by-layer growth.

On As-rich surfaces, Kneedler [33, 34] reported that the growth proceeded with nucleation of 2D island followed by layer-by-layer growth. The reason for the 3D cluster growth on the Ga rich surface and 2D growth on the As-rich surface was attributed to the bonding energy between Fe-Ga and Fe-As. Fe prefers to bond to As over Ga atom [35, 36].

Atom Outdiffusion and Interface Interdiffusion: Sano and Miyagawa [37] measured As and Ga atomic Auger emission spectroscopy(AES) intensities for different Fe film thickness and substrate temperature. Figure 28 shows the results. They found that both Ga and As diffused out of the substrate at high temperatures (>500ºc) and segregated into the film but only As outdiffuses at lower temperatures. Monchesky [29] and Schults [38] suggested a 0.75 ML and 0.7 ML of As segregation to the surface regardless of surface reconstruction and growth temperature. Theoretical study by Mirbt [36] suggested that As has a stronger chemical driving force to outdiffusion than Ga.

At the interface, the structure is Fe/reacted layer/ GaAs. The reacted layer has the form of $Fe_3Ga_{2-x}As_x$ [39-41]. $Fe_3Ga_{2-x}As_x$ is ferromagnetic while Fe_2As is antiferromagnetic.

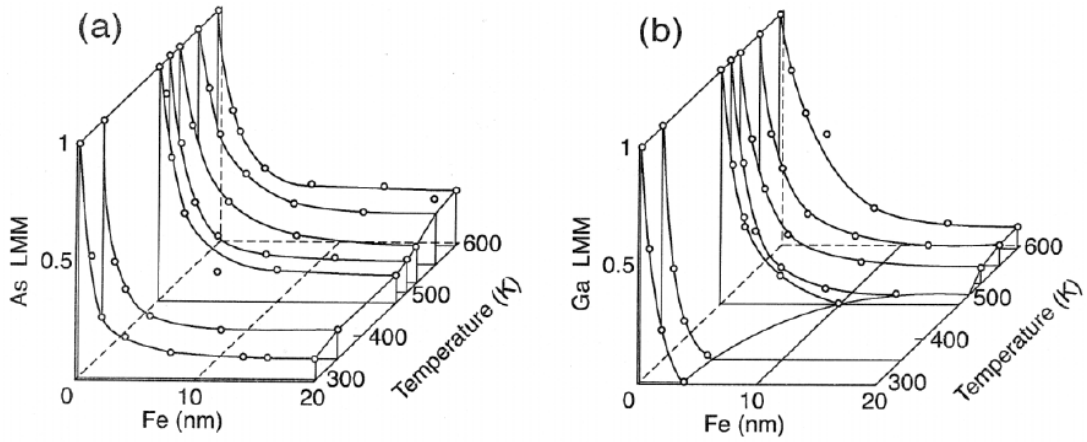

Figure 28: AES signal intensities of As(a) and Ga(b) as a function of Fe film thickness and GaAs substrate temperature.[37] Reproduction from Jpn. J. Appl. Phys., **30**, 1343, 1991, Sano, K. and T. Miyagawa, Surface Segregations During Epitaxial Growth of Fe/Au Multilayers on GaAs(001)

Magnetic Properties: For bulk Fe in the BCC structure [8, 21], the Curie temperature is 1043 K, and the saturation magnetization at room temperature is 1707 emu/cm^3. Magnetic moment per Fe atom is 2.22 μ_B. Magnetic anisotropy is in the cubic form and the magnetic anisotropy constant K_1 is 4.81×10^5 erg/cm^3, and K_2 is 1.2×10^3 erg/cm^3. The K_1 term dominates with <100> the easy axes and <111> the hard axes.

When Fe is deposited onto GaAs at low temperature, Fe takes the form of BCC α–Fe, but the properties change compared with the bulk α–Fe. Jantz [16] first reported the magnetic anisotropies of Fe/GaAs(100) via FMR measurement and showed that an in-plane uniaxial anisotropy presented in these samples. Krebs [10] studied different thickness of Fe films and found that all of the thin films had [-110] as hard axis for the uniaxial term.

The magnetization of Fe/GaAs could change due to the interdiffusion and outdiffusion. Theory suggests that interface layer of Ga or As reduces the interfacial Fe moment [35, 36]. But experiments showed that the Fe moment of these thin films is bulk like [30, 32, 42] or shows little reduced moment [43, 44].

The magnetic anisotropies of Fe/GaAs are also largely affected by the interface. The anisotropy can be separated into a surface term and a volume term. $K_1^{eff} = K_1^{vol} + (K_1^{Fe/GaAs} + K_1^{Cap/Fe})/t$ can be used to fit for the thickness data, where t is the thickness of the film. A volume contribution and interface contribution can be extracted out. The cubic anisotropy decreases significantly for reduced film thickness. The volume contribution of cubic anisotropy K_1^{Vol} of 4×10^5 erg/cm^3 is about the same as bulk α-Fe. The interface contribution K_1^{int} is about -4×10^{-2} erg/cm^2. The two terms are in the opposite sign which means that the hard and easy axes rotate 45° from the interface to the bulk [29, 31, 45].

The uniaxial anisotropy term has been reported as a purely interface term as K_u^{vol} is almost zero. This uniaxial term does not depend on surface reconstruction or the termination of the surface. The easy axis is always parallel to [110] whether the growth started on a Ga rich or an As rich surface [8]. The origin of the uniaxial in-plane anisotropy remains in dispute. The mechanism for the uniaxial term could be the surface bonding directions [46]. On the surface, the Fe-As bonding dominates and the directional bonding creates an easy-axis in the [110] direction. Mirbt [36] pointed out that because of this directional bonding, the in-plane strain along [110] is different from [-110]

(contraction larger along [110] than [-110]). The strain difference created an anisotropic magnetoelastic term and contributed to the uniaxial anisotropy.

Fe/ZnSe(100)

The growth of Fe/ZnSe has several advantages over Fe/GaAs substrate:

1. The epitaxial growth could happen at lower temperature for Fe/ZnSe while higher temperature is needed for epitaxial growth of Fe/GaAs. The low temperature growth will generate a sharp interface for Fe/ZnSe.
2. Spin relaxation time in ZnSe is very long. Theoretical calculations show that Fe/ZnSe/Fe structure presents a very large spin polarization of conduction electrons and a large tunneling magnetoresistance due to the higher tunneling probability of the majority electron of Fe through ZnSe.
3. No reduction of Fe magnetic moment is observed even for the first Fe monolayer grown at room temperature.

Atom Outdiffusion and Interface Interdiffusion: Mosca [47] *et al.* did annealing on Fe/ZnSe surface to investigate the stability of the interface. Their TEM image showed that Fe/ZnSe/GaAs has very sharp interfaces. The X-ray photoemission spectroscopy (XPS) data showed that for annealing below 390 °C, the surface remains unchanged. The Fe state did not change and the residual ZnSe on the surface disappeared as annealing temperature went up. As annealing went beyond 400 °C, the Fe core level spectra changed and on the surface, the Zn and Se signal showed up again and became stronger as temperature increased. This indicates that ZnSe epilayer migrates to the surface of the Fe film. The intensity of Se signal is much larger than Zn signal, which indicates that Se

likes to float on top of Fe. The as-prepared sample did not show any Ga signal. As annealing temperature went up to 400 °C, the Ga signal appeared.

Growth Mode and Magnetic Properties: The lattice mismatch between ZnSe and GaAs is small, so ZnSe can grow epitaxially on GaAs and Fe can also grow epitaxially on ZnSe. Fe grown on ZnSe has been shown to have a layer by layer growth at 175 °C while the growth on GaAs showed 3-D growth mode. The Fe/ZnSe interface is less active than Fe/GaAs [18]. The interface properties made ZnSe a more promising substrate than GaAs. The magnetic moment in the above growth showed reduction, but the reduction is smaller for similar layer thickness than Fe/GaAs [10] .

The growth temperature controls the growth mode for Fe/ZnSe. At low growth temperature, like room temperature, the growth mode is 3D clusters. At 7 ML, the clusters coalesce and form a flat surface. The magnetic moment does not show reduction and Se atom segregation appears on top of the Fe thin film [48]. For growth temperature of 180 °C, the growth was toward 3D clusters for the first 5 ML and then coalesced. The coalescence was completed at 7 ML and was followed by layer-by-layer growth. No magnetic reduction was found at the interface. Photoemission study showed that Fe-Se bonding formed on the interface and Se floated on top of Fe. About 1.5 ML of Zn goes into Fe and occupies the Fe site [49]. The magnetic moment showed increase for the first 2 ML of growth [50]. For growth temperature of 450 K, the growth mode was 3D for the first 8 ML and was then followed by layer-by-layer growth. The magnetic moment did not show any reduction, but there was a paramagnetic-ferromagnetic transition during the

film growth. For Fe below 8 ML, it was shown to be superparamagnetic and above 8 ML, ferromagnetic Fe formed with poor crystalline quality [51].

Cubic Anisotropy: During the early growth of Fe/ZnSe, no cubic anisotropy was observed for the first 2 ML [50]. For thicker films, the cubic anisotropy of Fe/ZnSe is shown to have easy-axes in the <100> directions. The volume contribution has been found to be 4.5×10^5 erg/cm^3 [11, 52] (Reiger[48] found it is 6.3×10^5 erg/cm^3). Krebs [10] found that the cubic anisotropy field is 0.3 kOe, and the ZnSe interface has a contribution of -5.6×10^2 erg/cm^3, or -2.8×10^2 erg/cm^3.

Uniaxial Anisotropy: A uniaxial anisotropy is also present in the Fe/ZnSe growth. The easy-axis is in [110] direction and that hard-axis is in the [1-10] direction. The contribution of the uniaxial term comes from the purely interface component. The values of the uniaxial term are found to be 3.2×10^{-2} erg/cm^2 [11], or 5.9×10^{-2} erg/cm^2 [48], or 0.02 kOe [10].

Fe/GaAs(110)

Fe can also be epitaxial grown on the GaAs(110) surface. The growth method is similar to the growth on the GaAs(100) surface.

Atom Outdiffusion and Interface Interdiffusion: Ruckman [53] used synchrotron radiation photoemission to analyze room temperature growth interface of Fe on GaAs(110) surfaces. Their results showed that the substrate was disrupted with Fe, Ga and As atomic intermixing. Below the deposition of about 3 Å, there were significant amounts of Ga and As. For Fe and As, there were two kinds of bondings, the thin film

region and dilute Fe-As phase persisting to high coverage. Fe metal started to form at 5Å, and As was always present in the film. Ga seemed to be trapped near the original interface.

Strain on the Interface: Syed [54] showed that Fe/GaAs(110) film grown by MBE at temperature of 175 °C and 20 Å/min had a mosaic structure originating at the interface. The x-ray diffraction θ-2θ scan showed that the lattice constant resumed the bulk α-Fe value after 1 μm while for thin films, the d-spacing constant is lower than the bulk which is unexpected for Fe epitaxially grown on GaAs with a compressive strain. Prinz [55] showed that for the growth temperature of 175 °C, the growth mode was 3D at first and then coalesced at 25-50 Å. The FMR results [15, 56] showed that the Fe/GaAs(110) has a uniaxial in plane anisotropy and the easy axis of the uniaxial anisotropy changed from [110] to [001] as the thickness grew from 50 Å to 200 Å.

Haugan [57] used atmospheric pressure metal-organic chemical vapor deposition to grow Fe/GaAs(110) film at different substrate temperature and found that Fe films can grow single crystal between substrate temperature of 200 °C and 330 °C. Amorphous films were observed at substrate temperature below 200 °C and it was not possible to grow films when substrate temperature is above 330 °C. X-ray diffraction θ - 2θ scans showed that for Fe films grown with substrate temperature between 200 °C and 300 °C, the d-spacing lattice constant is 2.023 ± 0.003 Å, regardless of film thickness, close to bulk α-Fe of 2.0265 Å within experimental errors. While for a 144 Å Fe film grown at substrate temperature of 330 °C, the d-spacing lattice constant is 2.034, which is

expanded compared with bulk α-Fe. The expanding of Fe film indicates that there is a biaxial strain in the film. For a thicker film at 300 Å, the biaxial strain was still observed.

Ding [58] used rf-magnetron sputtering to grow films from 5 nm to 164 nm. X-ray diffraction and FMR were used to characterize these films. X-ray diffraction was conducted for our-of-plane direction using glancing angle in the in-plane direction. XRD data showed that for thin Fe films there is an in-plane expansion and out-of-plane contraction, which means that the thin Fe films have a tensile stress instead of a compressive stress as expected from lattice mismatch. When thickness reaches 164 Å, the lattice distortion disappeared but the lattice constant is about 0.2% bigger than bulk Fe, which might be caused by Ar atom incorporation during sputtering. The strain versus thickness relaxation is shown in Figure 29.

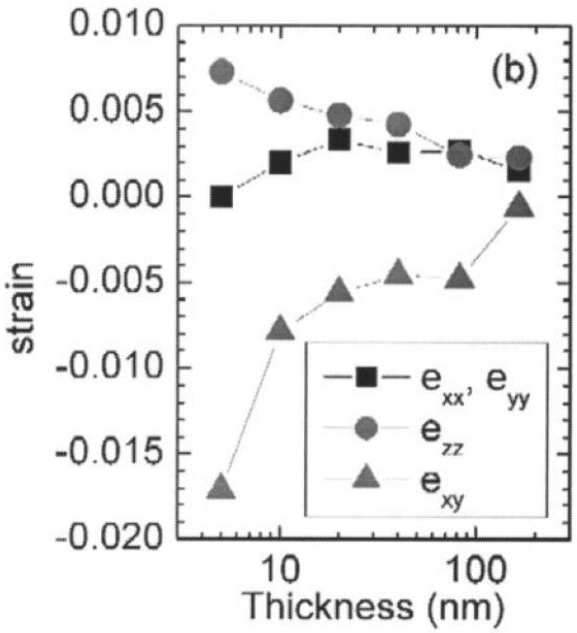

Figure 29: Strain for different Fe film thickness. [58] Reprinted with permission from Journal of Applied Physics, **93**, 6674, Y. Ding, C. J. Alexander, and T. J. Klemmer, Copyright [2003], American Institute of Physics.

Cubic and Uniaxial Magnetic Properties: Hollinger [59] used room temperature growth of Fe on GaAs(110) and observed a 3D growth mode in the beginning and a coalescence at 4 ML. The anisotropy easy-axis goes from [-110] to [001] as thickness goes from 4 ML to 64 ML. Thickness dependent data showed that $K_1^{Vol} = 3.6\times10^5$ erg/cm^3 and $K_1^{int} = -3.9\times10^{-2}$ erg/cm^3, or $K_u^{Vol} = 2.7\times10^5$ erg/cm^3 and $K_u^{int} = -14.1\times10^{-2}$ erg/cm^2.

Madami [60], using *in situ* brillouin light scattering, measured the anisotropies of Fe on GaAs(110) during growth. The results showed an easy-axis switch from [1-10] to [001] as thickness went from 20 Å to 120 Å. The fitted data showed that the uniaxial term changed sign when the thickness went from 40 Å to 100 Å. Then the film was capped with Cu which strongly affected the anisotropy of the thin (<10 Å) films.

Gester [61] used sputter anneal method to grow films at 150°C and did *in situ* study of magnetic anisotropies. Their results showed that the easy-axis of the uniaxial term changed sign as thickness changed. The easy-axis changed from [110] direction to [100] direction as thickness grew.

Winking [62] suggested using two step process to grow Fe films on GaAs(110) to improve the interface quality. In their experiment, they used growth temperature of 130 K and then step annealed to room temperature. Their LEED picture showed that the growth was layer-by-layer. There was no magnetic hysteresis showing up below 2 ML of deposition and the ferromagnetism showed up at 3.5 ML deposition. The easy-axis switched at 4 ML thickness from [001] to [110] as thickness went from 3.5 ML to 5 ML.

In Ding [58]'s research, the anisotropies for films ranging from 5 nm to 164 nm show that the uniaxial terms are all favoring the [001] direction, and the value decreases

with thickness except for the 82 nm sample. For 5 nm sample, the K_u/M value is 96 Oe and the value decreases to 47/19 Oe when thickness reaches 164 nm. The cubic anisotropy gets close to bulk value when the sample thickness reaches 164 nm (221Oe). When thickness is low, the K_1/M value is 189 Oe.

Uniaxial Term Review

The review for the uniaxial term for Fe/GaAs(100) or Fe/ZnSe(100) is difficult due to a vast amount of literature to read and the mislabeling of (110) and (1-10) directions in the literature. The existence of the uniaxial term is because either interface bonding changes the electronic structure or anisotropic strain generates the uniaxial term.

The papers that claimed that the directional interface bonding created the uniaxial terms are listed as below.

Sjostedt [46] proposed the theory that interface bonding changed electronic structures and produced the uniaxial term.

McPhail [63] compared the uniaxial term for Fe/GaAs(100) that has a smaller strain with Fe/InAs(100), which has a bigger strain. He found that the uniaxial term for Fe/GaAs is bigger than Fe/InAs even though the strain is smaller. The author therefore claimed that the uniaxial term is not caused by strain.

Lu [64] measured the magnetic anisotropy for Fe/GaAs(100) and concluded that the [1-10] direction is the hard axis for uniaxial term. The paper did annealing after growth. After annealing, perpendicular lattice dimension relaxed while the in-plane uniaxial term did not change much, so the uniaxial term cannot be caused by strain relaxation.

Morley [65] deposited Fe/ $Ga_{0.8}In_{0.2}As(001)$ to compare with Fe/GaAs(001). Fe and $Ga_{0.8}In_{0.2}As(001)$ have the same lattice constants so they should not have anisotropic lattice relaxation problem, but uniaxial term still presents and is almost the same with Fe/GaAs(001). So, uniaxial term could not come from lattice strain but from Fe-As bonds that distorted the BCC cell in the [110] and [1-10] directions.

Brockmann [31] showed that the uniaxial term for Fe/GaAs(001), [110] is the easy-axis direction while [1-10] is the hard direction. Uniaxial term is purely an interface term.

Moosbuhler [45] showed that for Fe/GaAs(001), easy-axis is always in the [110] direction, and surface reconstruction does not affect the uniaxial anisotropy.

Gustavsson [11] showed that for Fe/ZnSe(001), the uniaxial term has [110] as the easy direction and [-110] as the hard direction. His results showed that cubic interface anisotropy $K_1^{Fe/ZnSe}$ is $-5.6*10^{-2}erg/cm^2$, and the volume uniaxial contribution K_u^{vol} is zero. The interface uniaxial contribution $K_u^{Fe/ZnSe}$ is $3.2*10^{-2}erg/cm^2$. RHEED pattern showed anisotropic lattice relaxation in [110] and [1-10] directions below 15 Å.

Zakeri [66] used FMR to measure anisotropy for Fe/GaAs(001). For the uniaxial term, he determined that [110] is the easy axis while [1-10] is the hard axis. Strain relaxation can explain uniaxial term but had smaller value.

Papers that claimed that the uniaxial magnetic anisotropy is due to the anisotropic relaxations are listed as below.

Mirbt's theoretical calculation [36] showed that when Fe is deposited on GaAs, lattice expanded in [-110], and shrank in [110] due to the different Fe-As bonding energy and Fe-Ga bonding energy.

Gordon [67] did XAFS on Fe/GaAs(001). The results showed that the Fe lattice expanded in [-110] direction and shrank in the [110] direction, and that the distortation was a factor of 3 smaller than what theory predicted [36]

Thibado [68] used STM to investigate the interface of Fe/GaAs(001). The results showed that Fe islands elongated along [-110] direction (As dimer row) for the first 50Å film growth. That is because Fe-As bond is stronger, which resulted in Fe nucleation on surface As site.

Aktas [69] deposited Fe films on GaAs(001) and Au(001). Fe/GaAs(001) produces a compressive strain in the Fe film and the [1-10] direction is hard. Fe/Au(001) produces a tensile strain in the Fe film and the [1-10] direction is easy. He also found a linear temperature dependence of the magnetic anisotropy, which suggests uniaxial anisotropy is magnetoelastic effect and changed by thermal expansion.

Zuberek [70, 71] grew Si/Fe/GaAs and Ge/Fe/GaAs structures. He used FMR and strain modulated FMR (SMFMR) to measure magnetic anisotropy and magnetoelastic constants. His results showed that B1 for Ge/Fe/GaAs is large. B1 and B2 changed sign as thickness changes.

Schultz [38] used Rutherford backscattering, x-ray diffraction and TEM to find Fe/GaAs surface characteristics before and after 450 ºC annealing. After annealing, surface formed Fe_2As and Fe_3Ga ($D0_3$). The diffusion rate of Fe in the reacted interface was found to be of similar magnitude to that of Ga and As.

James [72] characterized Fe/GaAs(001) interface. He showed that the interface not only missed Fe columns, but also had partial occupancy of the remaining columns. There were about half the Fe missing in the partially occupied columns.

Thomas [73] investigated thickness dependence of the uniaxial magnetic anisotropy and the strain relaxation for Fe/GaAs(001). He found that when the Fe film is less than 1.5 nm thick, the [110] direction is easy. While as thickness increases to 13 nm, the [1-10] direction becomes the easy direction. Comparing the results with the anisotropic strain observation, he concluded that the interface generated a uniaxial term in the [110] direction while the anisotropic strain relaxation caused the easy direction to be in the [-110] direction. The two terms competed with each other and caused the easy axis to switch for different thickness.

Xu [74] deposited Fe/InAs(001) which produced a tensile strain in the Fe film. RHEED pattern showed that anisotropic strain relaxation and thickness range of uniaxial lattice relaxation were in perfect agreement with the uniaxial magnetic anisotropy thickness dependence.

Xu [75] compared Fe/InAs(001) which has tensile strain with Fe/GaAs(001) which has compressive strain. [011] is the easy-axis for Fe/InAs(001) while [011] is the hard axis for Fe/GaAs(001). Strain in Fe/InAs(001) relaxed much faster in the [1-10] direction, but to explain the uniaxial term using magnetoelastic theory, B_2 needs to have opposite sign of bulk Fe.

Cuenya and Roldan [76] deposited Fe thin films on Ga terminated GaAs(001) surface. Mossbauer showed V22 might come from a preferred non-cubic atomic environment of Ga atoms around the ^{57}Fe atom in the intermixed interfacial region.

Tournerie [77] deposited Fe/$Al_{0.48}In_{0.52}As$(001). He showed that the [110] direction is the easy axis for the uniaxial part.

Zhai [78] deposited Fe/GaAs(100). He showed that K_u is easy in the [1-10] direction.

Bensch [79] deposited Fe/GaAs(001). He showed that K_u is easy in the [110] direction.

FERROMAGNETIC RESONANCE SPECTROSCOPY

Ferromagnetic resonance spectroscopy (FMR) is a form of electron spin resonance (EPR) spectroscopy at microwave frequencies. It is called ferromagnetic resonance because the materials to be studied are ferromagnetic materials. FMR is a very important technique for characterizing magnetic thin films. First, we can determine the magnetic film quality from linewidths, resonance lineshifts, etc. Second, the resonance field shifts reveal magnetic properties like magnetic moment and magnetic anisotropies.

Introduction to EPR

In an electron spin resonance measurement, the resonance occurs for unpaired electrons in the materials. It is based upon the Zeeman effect, in which the electron spin moment $\mu_{B,}$ energy levels split in the presence of a magnetic field according to $E = -\vec{\mu}_B \cdot \vec{H}$, where μ_B is the magnetic moment for the electron and H is the magnetic field. The energy splitting will be bigger with the increase of the magnetic field. The Zeeman effect allows a ground-state electron to absorb a photon with energy equal to the splitting between the up and down energy states. So with a microwave at a fixed frequency *v*, the photon energy is *hv*. In most FMR measurements, the frequency is fixed and the applied field is varied. At the resonance field where photon energy is equal to the Zeeman splitting energy, photon can be absorbed. The electron spin resonance process is plotted in Figure 30.

In a magnetic material, magnetic anisotropy (whether magnetocrystalline, shape, or stress-induced) acts as an effective internal field on the unpaired electron, so this

electron will experience the internal field from the material plus the external applied field. With the same microwave frequency υ, the required external magnetic field (H_{res}) to have resonance will be smaller due to the internal field contribution.

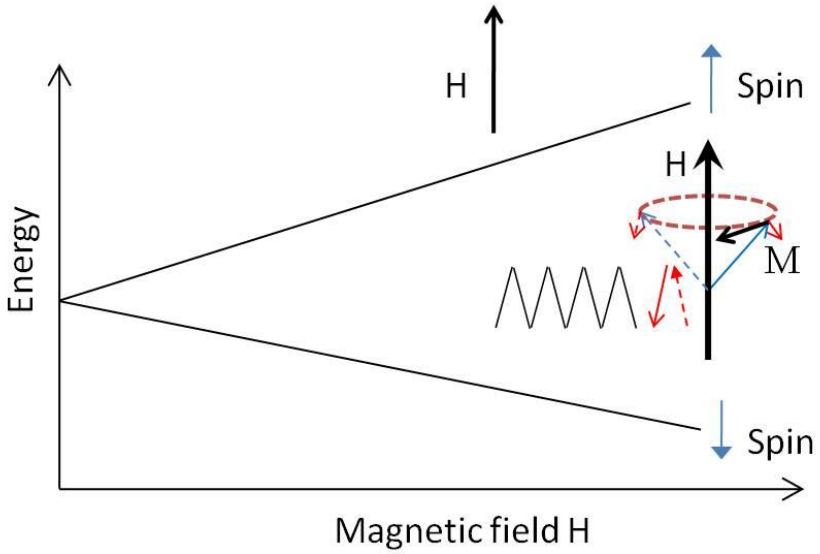

Figure 30: Zeeman splitting and electron spin resonance process.

The electron spin experiences a torque when placed in a magnetic field. This torque will cause the spin to precess along the magnetic field. The precession frequency of the spin is $\nu_0 = g\mu_B H/h$. When the precession frequency is equal to the microwave frequency, the spin will absorb the microwave energy. With anisotropic internal field, the external field needed to generate the same precession frequency will be smaller. So when the sample is rotated, because of the anisotropic internal field, the resonance field will shift. From the shift of the resonance field, the symmetry, magnitude and direction of the anisotropy field can be obtained. The details of EPR theory can be found elsewhere. [80]

Electron Spin Resonance in Ferromagnetic Materials (FMR)

FMR in principle is similar to EPR. The only difference is the working materials. In FMR, we work with ferromagnetic materials, where electron magnetic moments are strongly coupled to each other so the transition does not happen to individual spins but to magnons (quanta of spin waves).

The linewidth of FMR can tell the quality of film and relaxation time. The shifts in angular dependent resonance field can tell the magnetic anisotropy energy form and magnitude.

Resonance Theory

In ferromagnetic materials, magnetic moments are strongly coupled and have preferred direction. In equilibrium, a magnetic moment will point in the direction of the minimum energy surface. If the magnetic moment is perturbed from its equilibrium point, it will experience a torque. The torque will make the magnetic moment precess around its energy minimum with a frequency proportional to the second derivative of energy surface. If a microwave at the same frequency as the precessing frequency of the magnetic moment is applied, the magnetic moment will absorb the microwave photon. This is called resonance absorption. In materials where there is anisotropic energy for the magnetic moment in different directions, the magnetic moment will have a natural precession frequency along the easy-axis as if there were an equivalent magnetic field in the easy-axis direction.

Applying a magnetic field to the material, magnetostatic energy will superimpose on anisotropy energy and if the magnetic field is large, it will tend to create an energy

minimum in the direction of the applied field. This will align the magnetic moment in the field direction. The precession frequency will be $\frac{\omega}{\gamma} = \left|\vec{H}_{res} + \vec{H}_{\text{int}}\right|$. If we measure the resonance field for a full angular rotation of the sample, the equivalent internal field can be extracted.

Following Smit and Beljers [81], and Suhl[82], we denote E as the total energy of magnetic moment in the ferromagnetic material. The equilibrium position of the magnetic moment is in the z direction. When the magnetic moment is slightly displaced from the equilibrium direction, the torque experienced by the magnetic moment will be:

$$\frac{dM}{dt} = \gamma M \times H \quad . \tag{15}$$

and the equation of motion for the magnetization will be:

$$\begin{aligned} -M\dot{\theta} &= \gamma \partial E / \partial \varphi, \\ M\dot{\varphi} &= \gamma \partial E / \partial \theta. \end{aligned} \tag{16}$$

From small deviations of the equilibrium point, the energy E can be expanded in a Taylor series:

$$E = E_0 + \frac{1}{2}(E_{\theta\theta}\theta^2 + 2E_{\theta\varphi}\theta\varphi + E_{\varphi\varphi}\varphi^2) \quad , \tag{17}$$

where $E_{\theta\theta}$ is $\partial^2 E / \partial\theta^2$, $E_{\theta\varphi}$ is $\partial^2 E / \partial\theta\partial\varphi$ and $E_{\varphi\varphi}$ is $\partial^2 E / \partial\varphi^2$.

The equations of motion now become:

$$\begin{aligned} -M\dot{\theta} &= \gamma(E_{\varphi\varphi}\varphi + E_{\theta\varphi}\theta), \\ M\dot{\varphi} &= \gamma(E_{\theta\theta}\theta + E_{\theta\varphi}\varphi). \end{aligned} \tag{18}$$

The solution for this equation of motion will be:

$$\omega_{res} = \frac{\gamma}{M}\left[\frac{\partial^2 E}{\partial\theta^2}\frac{\partial^2 E}{\partial\varphi^2} - \left(\frac{\partial^2 E}{\partial\theta\partial\varphi}\right)^2\right]^{\frac{1}{2}} . \quad (19)$$

For an arbitrary equilibrium position (θ_0, φ_0), the resonance angular frequency will be:

$$\omega_{res} = \frac{\gamma}{MSin\theta}\left[\frac{\partial^2 E}{\partial\theta^2}\frac{\partial^2 E}{\partial\varphi^2} - \left(\frac{\partial^2 E}{\partial\theta\partial\varphi}\right)^2\right]^{\frac{1}{2}} . \quad (20)$$

where ω_{res} is the procession frequency, M is the magnetization, E is the energy, θ is the azimuth angle and φ is the polar angle.

The relation between the magnetic moment precession frequency and the magnetic field for a cubic system is plotted in Figure 31. In this figure, the relation between the rotation angle and resonance field can be seen for frequencies from 0 to 25 GHz. For low microwave frequency, for example 5 GHz, when the sample is at 45º, there will be two resonance fields, at 600 Oe and at 900 Oe. While as we rotate the sample 4º degrees away from 45º, no resonance line will be seen. For the higher resonance field, for example 15 GHz, there will be a resonance line for every angle.

In magnetic thin films, additional anisotropic energies are the demagnetization field and the magnetostatic energy. We only deal with simple cubic and uniaxial anisotropic materials, so we follow the FMR theory from Krebs [10] and Artman [83] for magnetic thin films.

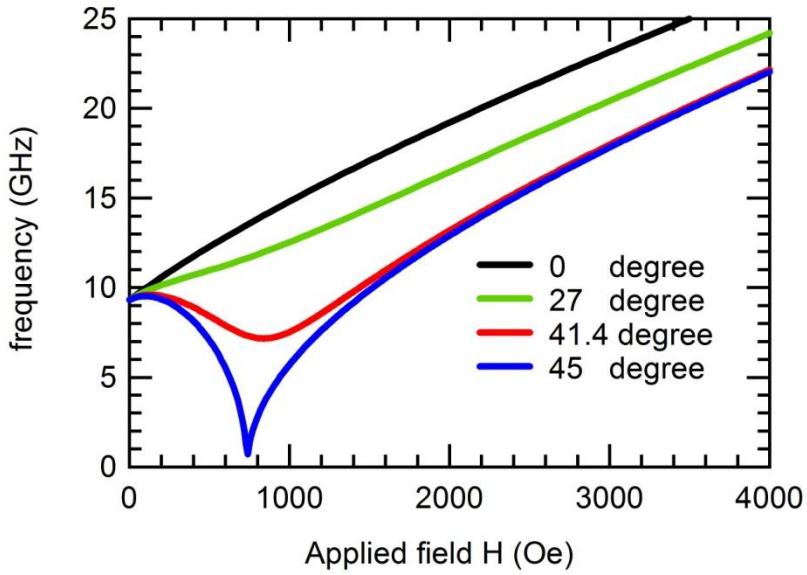

Figure 31: Frequency and magnetic field plot for a cubic anisotropy when magnetic fields are in different directions.

Thin Films in the (01-1) Plane with Cubic Magnetic Anisotropy

Now we consider an arrangement where a magnetic thin film is deposited onto a substrate, and the film surface is the (01-1) plane, we apply a magnetic field H in the film plane with an angle ψ to the [100] direction as shown in Figure 32. The magnetization direction has an angle of θ with respect to [100] and the azimuth of M has angle ϕ. If the magnetic thin film has cubic anisotropy energy, the form of free energy density to first order is:

$$\begin{aligned} E = & \frac{1}{4}K_1(\sin^2(2\theta)+\sin^4\theta\cdot\sin^2(2\varphi)) \\ & -MH(\cos\theta\cdot\cos\psi+\sin\theta\cdot\sin\psi\cdot\sin(\tfrac{1}{4}\pi+\varphi)) \\ & +\frac{1}{2}\times 4\pi M^2(n\cdot\cos^2\theta+n\cdot\sin^2\theta\cdot\sin^2(\tfrac{1}{4}\pi+\varphi)+(1-2n)\cdot\sin^2\theta\cdot\cos^2(\tfrac{1}{4}\pi+\varphi)) \end{aligned} \quad (21)$$

where the first term is the cubic anisotropy term, the second term is magnetostatic energy, the third term is the demagnetization energy, and $4\pi n$ is the demagnetization factor for the thin film in the plane. Usually, for a very thin film, n is equal to 1. Here because of small skin depth, the demagnetization effect from the rf field has been ignored.

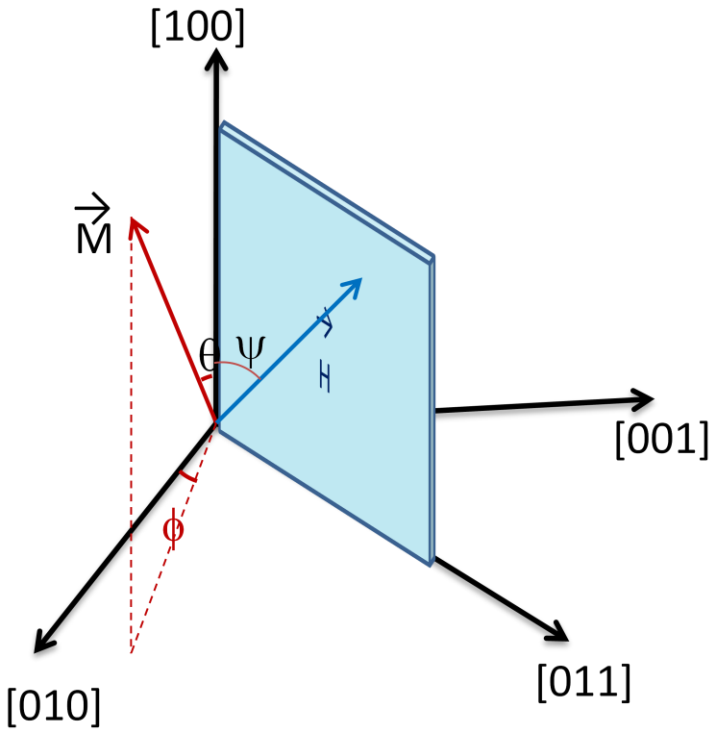

Figure 32: Magnetic thin film and external field H are in the (01-1) plane.

Thin Films in the (010) Plane with Cubic Anisotropy

For a magnetic thin film deposited on a substrate with the (001) plane parallel to the substrate, and applied magnetic field in the film plane, the setup can be drawn as in Figure 33. For a magnetic film with cubic anisotropy energy, the free energy to the first order can be written as:

$$E = \frac{1}{4}K_1(\sin^2(2\theta) + \sin^4\theta\sin^2(2\varphi)) - MH(\sin\theta\cos(\Phi - \varphi)) + \frac{1}{2}\times 4\pi M^2(n\cdot\sin^2\theta + (1-2n)\cdot\cos^2\theta) \quad (22)$$

Again the first term is the cubic anisotropy energy, the second term is the magnetostatic energy, and the third term is the demagnetization energy. Φ is the angle between applied magnetic field and the [100] axis. The magnetization direction has an angle θ with the [010] axis and the azimuth angle is ϕ to the [100] axis.

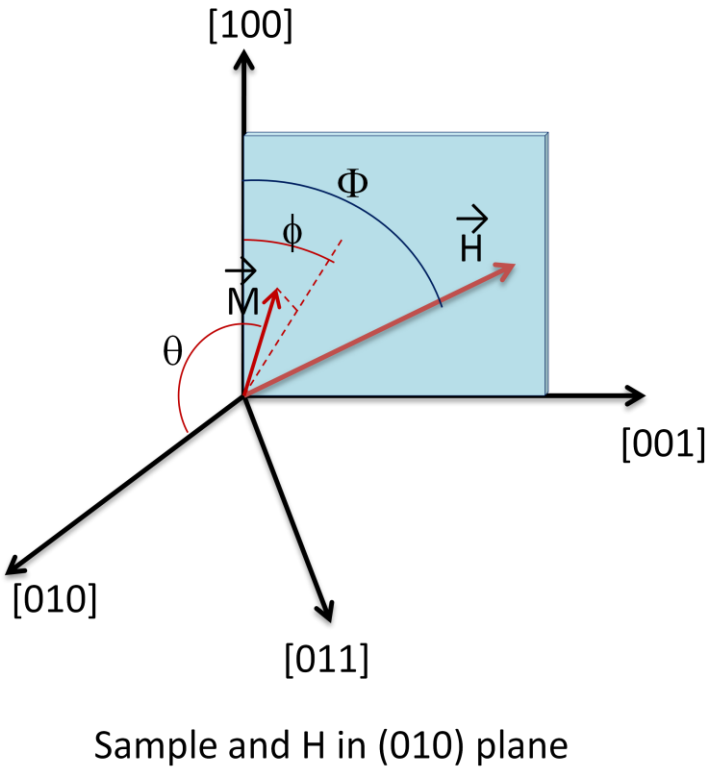

Figure 33: Sample and applied magnetic field in the (010) plane

Thin Films in the (01-1) Plane with Uniaxial Anisotropy

A uniaxial term with easy or hard axis in the [100] direction (see Figure 34) can be expressed as:

$$E_u = K_u Cos^2[\theta]. \tag{23}$$

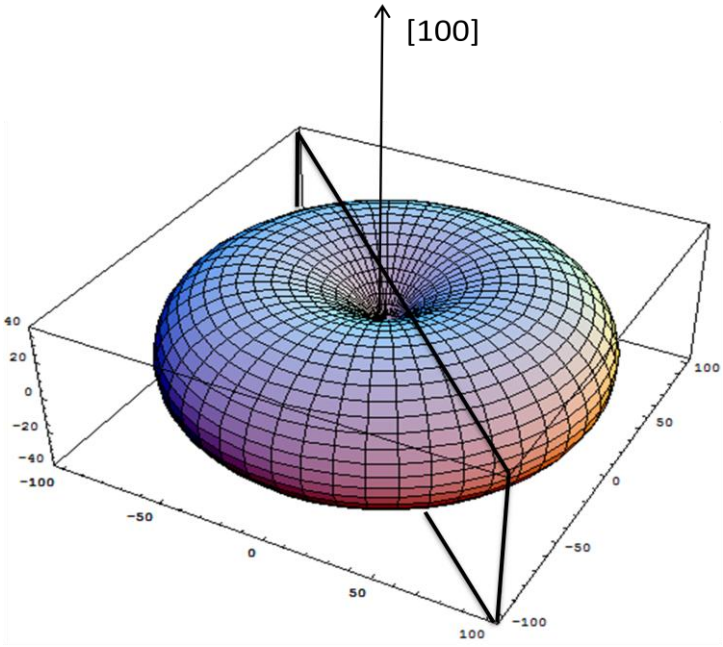

Figure 34: A thin magnetic film in the (01-1) plane with uniaxial anisotropy in the [100] direction. The black frame is the film plane.

Thin Films in the (010) Plane with Uniaxial Anisotropy

A uniaxial term in the (010) plane (see Figure 35) can be expressed as:

$$E_u = K_u \cos^2(\phi + \phi_0). \tag{24}$$

where ϕ_0 is the angle between the hard axis and the [100] direction.

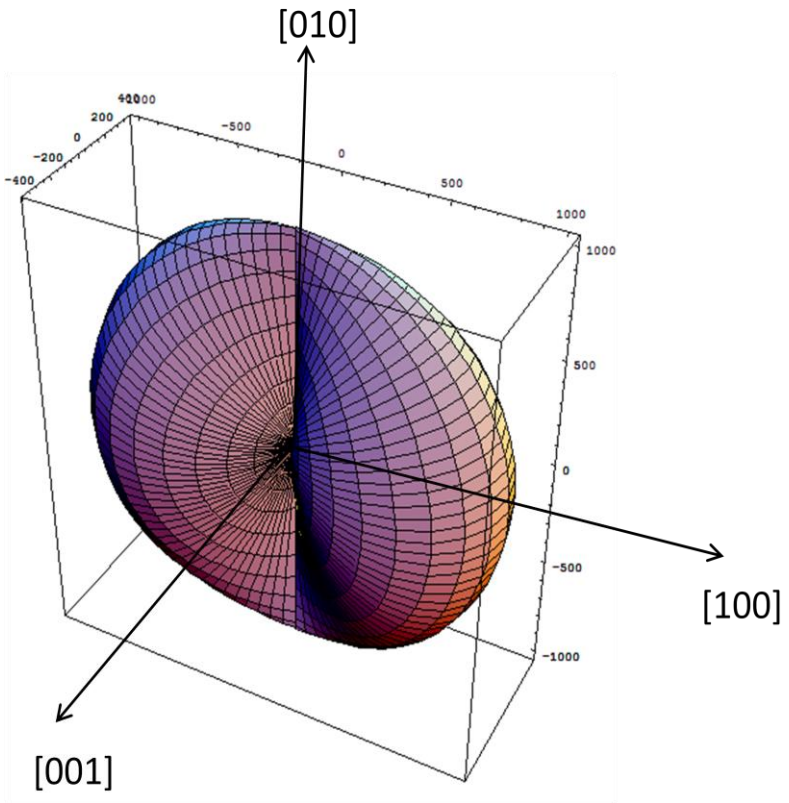

Figure 35: A thin magnetic film in the (010) plane with uniaxial anisotropy hard axis in the [100] direction

For a cubic system with uniaxial anisotropy, the magnetic energy can be written as:

$$E = -M \cdot H + K_1(\alpha_1^2\alpha_2^2 + \alpha_2^2\alpha_3^2 + \alpha_1^2\alpha_3^2) + K_u \cos^2\Theta + 2\pi M_\perp^2 + K_\perp (M_\perp / M)^2 . \quad (25)$$

Here the first term is magnetostatic energy. The second term is the cubic crystalline anisotropy energy where K_1 is the usual fourth-order cubic anisotropy constant. When K_1 is positive, the easy axes are along [100], [010], and [001]. The third term is the uniaxial in-plane energy, where K_u is the uniaxial second order anisotropy constant. The fourth term is demagnetization field. The fifth term counts for any perpendicular anisotropy

energy. α are the direction cosines of M. Θ is the angle between M and in-plane [100] axis.

Magnetic Field Dependent Magnetic Anisotropy Term

When there is no external field applied, the magnetic moment will align in the easy-axis direction and has a natural precession frequency. When an external field H is applied in another direction, it will tilt the magnetic moment direction and also change its precession frequency. If there is a magnetic field dependent energy term in the magnetic anisotropy energy, for different microwave frequency, due to the resonance fields happening at very different magnetic field, the field dependent magnetic anisotropy constant can be extracted out.

For a cubic system, if the magnetic field dependent magnetic anisotropy is in the same direction as the uniaxial anisotropy direction, the magnetic energy can be written as:

$$\begin{aligned} Energy = & \frac{1}{4}K_1(sin^2(2\theta) + sin^4\theta sin^2(2\varphi)) \\ & -MH(sin\theta cos(\Phi - \varphi)) \\ & +2\pi M^2 cos^2\theta \\ & +K_u cos^2(\varphi + \frac{\pi}{4}) \\ & +a_0 MHCos^2(\varphi + \frac{\pi}{4}) \end{aligned} \quad . \qquad (26)$$

Here the last term is the field dependent anisotropy term. In the following section, we will compare the resonance frequency versus magnetic field for the no-field-dependent anisotropy (a_0=0) and the field-dependent ansitropy (a_0=0.2) in two rotation angles, 0º and 45º. In Figure 36, the black line plots the resonance field with the applied field

strength for samples without field dependent mangetic anisotropy. The red line plots the resonance field with the applied field relation for samples with a uniaxial field dependent mangetic anisotropy with strength a_0 equal to 0.2.

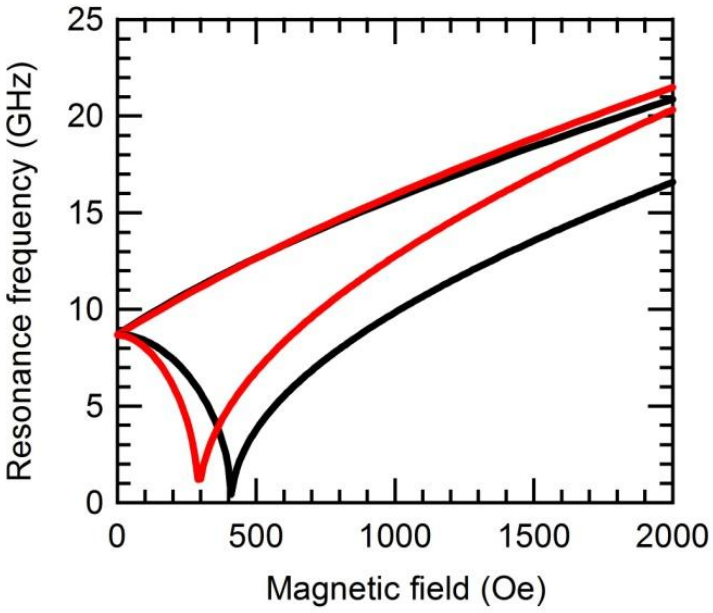

Figure 36: A field dependent magnetic anisotropy effect on magnetic anisotropy changes on different frequency.

Line Shape and Linewidth

The lineshapes of EPR can usually be fitted with a Lorentzian or Gaussian function. The Lorentzian line shape takes the form of $y = \frac{a}{1+bx^2}$, and the Gaussian takes the form of $y = a\exp(-bx^2)$. The line shape of the EPR is determined by the types of interaction between the spin and its environment. The line widths depend on the strength of interaction and the relaxation time. For a system with homogeneous environment the

relaxation time is short so the spin system remains in thermal equilibrium during the experiment. Normally the line shape is Lorentzian. For a system with inhomogeneous environment, the line shape is Gaussian.

FMR linewidth is a good indicator of relaxation time and it comes from both homogeneous broadening and inhomogeneous broadening. Both the spin lattice relaxation time T_1 and spin-spin relaxation time T_2 contribute to the line width. In an inhomogeneous environment, the inhomogeneous broadening determines the line width of EPR signal.

The inhomogeneous sources are:

1. An inhomogeneous magnetic field, which might come from external (applied field is not uniform) or internal of the material.
2. Crystallographic axes which are in different directions in the materials.
3. Two magnon scattering.
4. Phonon magnon scattering.

The intrinsic effects are:

1. Eddy currents,
2. Radiation damping,
3. Spin-Orbit coupling,

FMR measures the resonance of spin wave, other than the individual spins, so exchange energy does not contribute to the resonance energy in FMR measurements.

EXPERIMENTAL SETUP

Sample Growth

Single crystal thin films of $Fe_{1-x}Ga_x$ have been grown by Adam McClure using the MBE system. The procedure has been previously described [19]. The polished GaAs surface was first sonicated in acetone for 5 minutes, next rinsed in methanol, then rinsed in de-ionized water, and finally dried with nitrogen gas. To remove the carbon contaminants, substrate was treated with ozone for 45 minutes. The last step of the cleaning was to heat the substrate to 620 ºC for 45 minutes in an ultrahigh vacuum condition to remove the surface oxides and other contaminants.

To improve the substrate and thin film interface, an 80 nm ZnSe buffer layer was grown on the GaAs. The substrate was held at 175 ºC, and single source ZnSe crucible was used at a deposition rate of 13 Å/min. A UTI quadrupole mass spectrometer was used to monitor the flux of the source materials. After the buffer layer was deposited, the sample was cooled to 150 ºC. The deposition of $Fe_{1-x}Ga_x$ thin film was from independent Fe and Ga Knudsen cell sources. The thickness of the $Fe_{1-x}Ga_x$ alloy thin films deposited were about 21 to 25 nm as determined by Rutherford backscattering. The deposition rate was 2.3 to 2.8 Å /min. A 40 Å Al layer was deposited on top of the $Fe_{1-x}Ga_x$ alloy film to protect them from oxidation. The capping layer was deposited at a substrate temperature of 100 ºC with deposition rate being 3.5 Å /min.

The samples prepared to investigate the Ga concentration effect were: Pure Fe, and iron doped with 4.5%, 7%, 11%, 15%, 20%, 21%, 23%, 36%, 38%, 45% and 57% Ga concentration grown at about 20 nm thickness on ZnSe(100) and 0%, 15%, 20%,

21%, 23%, 33%, 38% and 45% Ga concentrations grown at about 20 nm on ZnSe(110) surfaces.

The samples used to study the $Fe_{1-x}Ga_x$/ZnSe interface effects were prepared at different thicknesses. The samples at 21% Ga concentration were at thickness of 2.4 nm, 4.8 nm, 9.9 nm, 19.8 nm and 39.7 nm on ZnSe(100) surfaces and at 10 nm, 20 nm and 40 nm thickness films on ZnSe(110) surfaces.

Sample Characterization using VSM and RHEED

In the first chapter, we have introduced the sample growth procedure. The sample quality was monitored by reflection high energy electron diffraction (RHEED). XMCD [84] and VSM [19] were used to characterize the magnetic properties. During the growth, the sample concentration was monitored using a UTI quadrupole mass spectrometer to measure the flux rate. The thickness was monitored by deposition duration. The final thickness and concentration results were determined using Rutherford backscattering postgrowth. The crystal quality of the GaAs surface and each deposited layer was monitored *in-situ* by RHEED using 10 KeV electrons.

Figure 37 shows the RHEED patterns for the clean GaAs (001) surface, the deposited ZnSe(001) buffer layer and the deposited BCC $Fe_{0.89}Ga_{0.11}$ film. The discontinuous lines of GaAs substrate show that the GaAs surface is rough and the clean lines for ZnSe show that the ZnSe buffer layer has epitaxial growth on GaAs and the quality of the ZnSe buffer layer has been greatly improved. The RHEED pattern for the $Fe_{0.89}Ga_{0.11}$ is shown in Figure 37 and it indicates a (2×1) surface reconstruction and the

BCC single crystal is in registry with the ZnSe buffer layer. The lattice constant of the BCC $Fe_{0.89}Ga_{0.11}$ is 2.9 Å and close to that half of ZnSe.

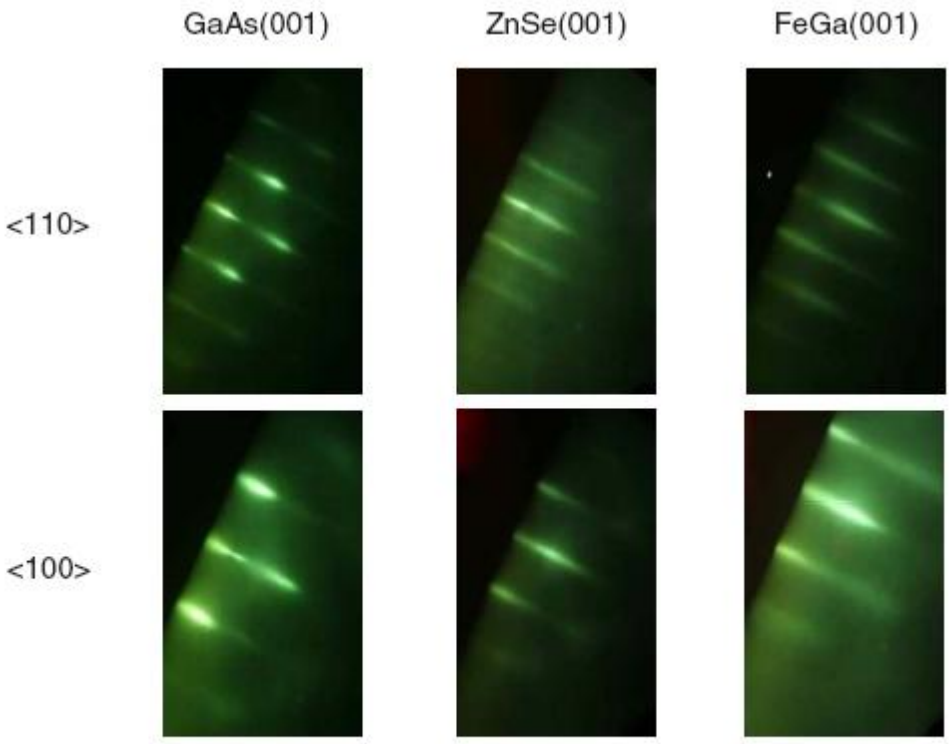

Figure 37: RHEED patterns of the clean GaAs(001) surface, the ZnSe(001) buffer layer, and the BCC $Fe_{0.89}Ga_{0.11}$(001) film. The incident electron beam is along the in-plane direction shown.

The magnetic properties of these $Fe_{1-x}Ga_x$ samples have been measured using vibrating sample magnetometer (VSM), an option from the Quantum Design Physical Property Measurement System (PPMS). The magnetic field was applied in the plane of the samples along the primary high symmetry directions. Figure 38 shows an example VSM measurement results on 5% Ga and 28% Ga films. From (a) we see that along <100> direction, the hysteresis loop is square and the magnetization is easily saturated at a magnetic field less than 50 Oe. And along <110> and <1-10> directions, the saturation

field is as high as 500 Oe. That shows the easy axis is along<100> direction. While for 28% doping of Ga, the square hysteresis loop changed to <110> direction and the <100> becomes the hard axis. Another interesting feature is the inequivalence of <110> and <1-10> directions.

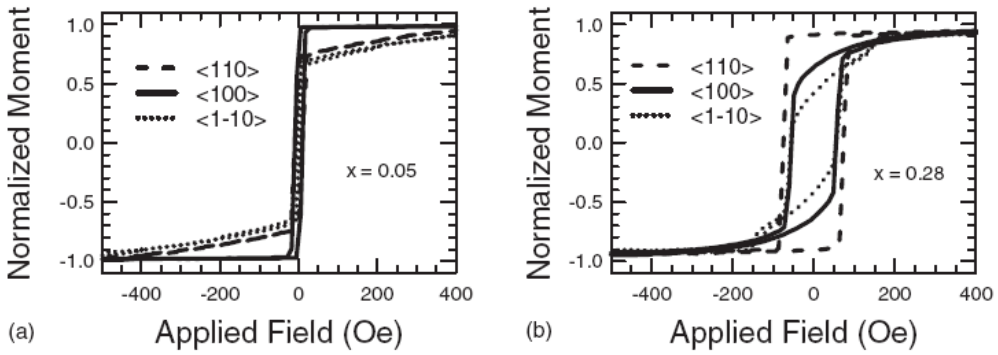

Figure 38: Hysteresis measured by VSM for FeGa/ZnSe(001) along 3 different principle axes. The left panel shows the hysteresis loop for 5% Ga doping. The right panel shows the hysteresis loop for 28% Ga doping.

Identification of Sample Orientations

The substrate orientations have been indentified using factory labeling, reflection high energy electron diffraction (RHEED) and electron backscattering diffraction (EBSD).

RHEED is a technique used to characterize the sample surfaces. It is especially useful for monitoring the growth of films in a MBE chamber. Sample orientations can be identified from the spacing of stripes in the RHEED picture. Figure 39 shows the RHEED images for the three principle axes for ZnSe(110) surface grown on GaAs(110) surface.

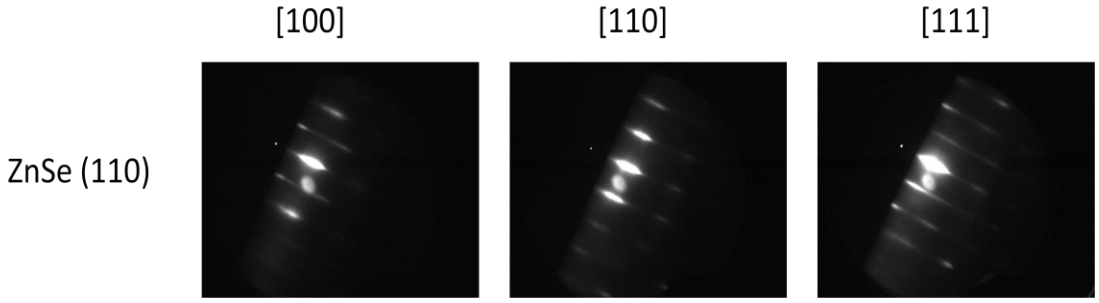

Figure 39: RHEED images of ZnSe deposited on GaAs(110) surface in three principle axes [100], [110], and [111]. The line spacing is inversely proportional to the real lattice spacing.

Sample orientations have also been carried out from the EBSD system. EBSD is a technique to obtain crystal information at the sample surface. A setup and layout of the system is shown in Figure 40 and Figure 41. An electron beam is incident on a tilted crystal sample, and an electron back scattering pattern forms on a phosphor screen. The diffraction pattern consists of Kikuchi lines which are results of electron diffraction from different crystalline planes. From the diffraction pattern we can determine crystal structures and its orientation relative to the sample.

The experiment uses electron energy at 20 keV with incident angle at 70º to the sample. EBSD is a surface technique which probes 20-100 nm below the surface. It can be used to indentify crystal orientations and phases. The spatial resolution of this technique is 20 nm to 1 mm, it has a relative angle resolution of 0.1º-1º and absolute resolution of 2º.

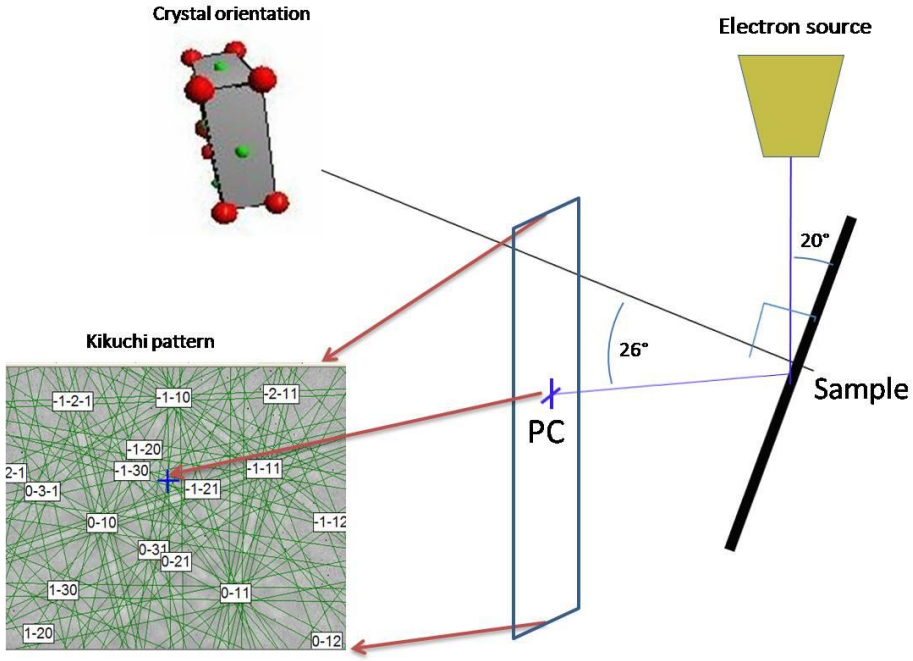

Figure 40: A schematic plot of the EBSD system.

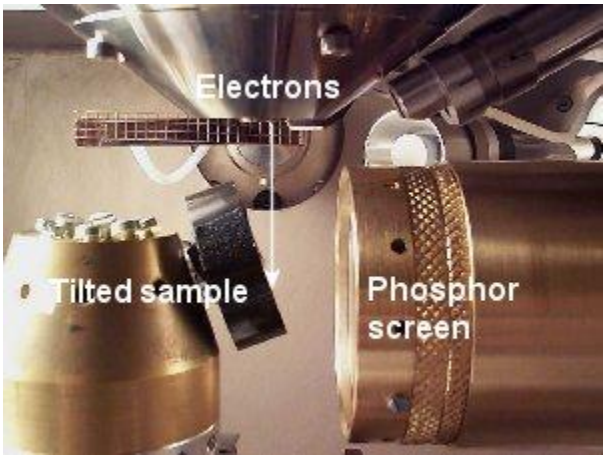

Figure 41: Set up of the EBSD system.

The left panel in Figure 42 shows the Kikuchi pattern collected from a screen that is about 75° titled relative to the sample normal. The right panel in Figure 42 showed the crystal orientation viewed from the sample normal.

The crossing-signs + in Figure 40 and Figure 42 are the pattern center (PC), which describes the location of the nearest point between the phosphor screen and the sample. The center of the Kikuchi band corresponds to the intersection between the diffracting plane and the phosphor screen. The labeling of intersections between Kikuchi bands are the crystal axis directions. The position of the Kikuchi bands can be found automatically with the Hough transform and used to calculate the crystal orientation of the sample region that formed the pattern.

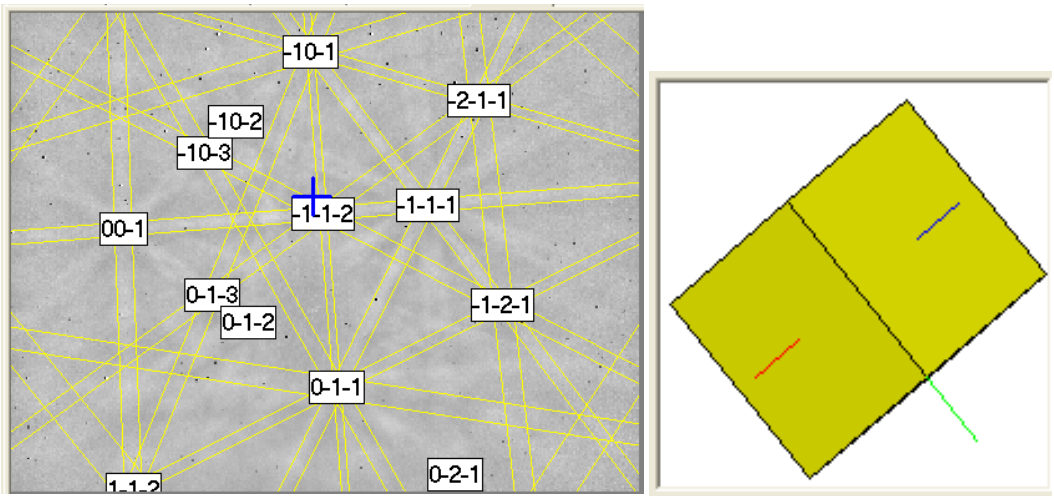

Figure 42: The left panel shows the Kikuchi pattern from the phosphor screen. The numbers show the crystal axis directions. The right panel shows the crystal orientation obtained from the Kikuchi pattern.

Introduction to the FMR Machine

An EPR system consists of the microwave bridge which contains the electromagnetic radiation source and the detector, as shown in Figure 43. The sample is in the microwave cavity which can amplify weak signal from the sample, with a magnet for tuning the energy levels. The system also has a console which contains signal processing and control electronics and a computer. Refer to the Bruker manual for more details.

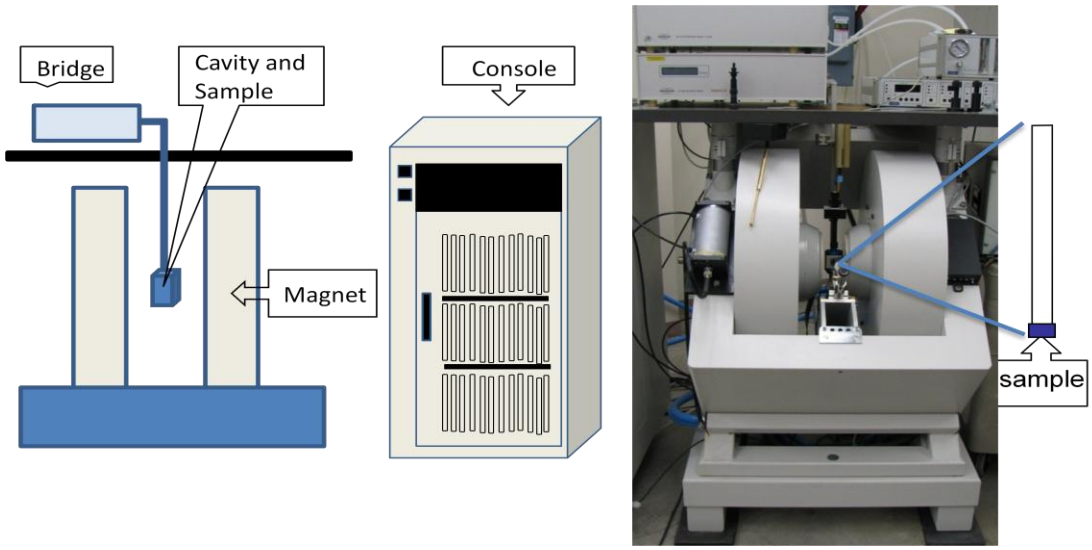

Figure 43: Setup of a FMR machine.

The Microwave Bridge

The microwave bridge contains the microwave source and the detector. The basic idea of the bridge is shown in Figure 44. A microwave source generates a signal, and the signal intensity gets tuned by the attenuator and goes to the cavity. The detection of the signal is from the reflected signal from the cavity. The reflected signal passes the

circulator and goes into detector diode and outputs a voltage. For accuracy and linearity of the signal intensity, a reference signal is also input into the detector diode. The phase and intensity ("bias") of the reference signal can be adjusted to get the best signal.

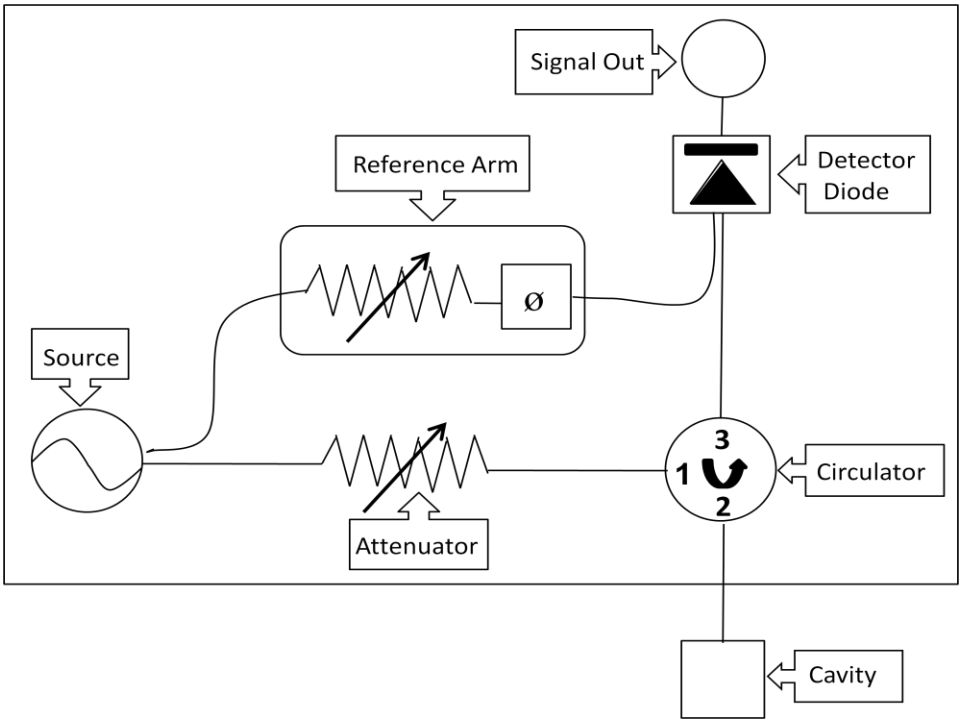

Figure 44: Schematic drawing of how the microwave bridge works.

The EPR Cavity

A microwave cavity is a metal box used to amplify the weak signal from the sample. At the resonance energy of the cavity, all the microwave energy will be stored in the cavity without any reflection. Cavities can be characterized by their quality factor *Q*, which is defined as how efficiently the cavity stores microwave energy.

$$Q = \frac{2\pi(energy\ stored)}{energy\ dissipated\ per\ cycle}$$

Energy dissipation per cycle means the loss of energy during one microwave period. The measurement of *Q* factor can be done as:

$$Q = \upsilon_{res}/\Delta\upsilon .$$

where υ_{res} is the resonance frequency of the cavity and $\Delta\upsilon$ is the width of the resonance frequency at half height.

When a sample is placed into the cavity, it will change the resonance condition. When the resonance energy of the cavity meets with the microwave, it will absorb the energy. In this case, *Q* factor will be lower and microwave will be reflected back. This results in an EPR signal.

To increase the sensitivity of detection, the sample needs to be in the best position in the cavity and an "iris screw" is used to adjust the cavity impedance. An "iris screw" is a screw between the cavity and the waveguide. By moving the iris screw up and down, the iris of the cavity will change size and thus change the impedance of the cavity. When the cavity is critically coupled, the Q factor will be large.

The Signal Channel

To enhance the sensitivity, EPR spectrometers use a phase sensitive technique (lock-in amplifier). This technique eliminates the baseline instability due to DC electronics, and generates less noise from the detection diode. This technique also eliminates noise or interference which has a frequency that is different from the modulation frequency.

The scheme of the detection works as follows. A slowly swept magnetic field is applied to the cavity. On top of this sweeping magnetic field, another sinusoidal

modulated field is also applied to the cavity. The EPR signal will also be modulated and the amplitude is proportional to the slope of the original signal.

The signal channel compares the modulated signal with a reference signal that has the same frequency and phase with the modulated field, and extracts the amplitude of the modulated signal, and then produces a DC signal that is the derivative of the original EPR signal. This process is shown in Figure 45.

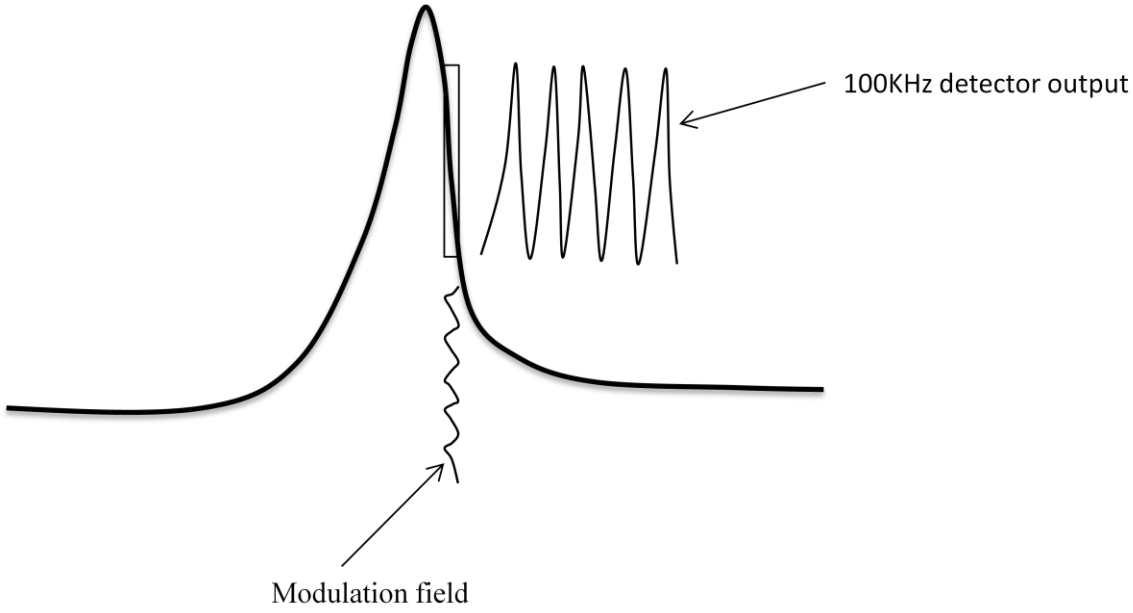

Figure 45: The generation of EPR signal.

Magnetic Field Controller

Magnetic field controller consists of two parts: a part which sets the field values and timing of the field sweep, and a part which regulates the current in the magnet to attain the requested field value.

A microprocessor is used to control the field and timing of magnetic field sweep. The field sweep can be divided into a maximum of 4096 steps. At each step, a

corresponding voltage is sent to the controller that regulates the magnetic field. The waiting time between each step is controlled by total sweep time.

A Hall probe is placed in the gap of the magnet. The Hall probe generates a voltage that is proportional to the magnetic field. By comparing the magnetic field from Hall probe and the reference voltage set by the microprocessor, a necessary adjustment to the current will be made to the magnet.

FMR Measurement

We used room temperature FMR to measure the magnetic anisotropies for all of our samples. The experiment was done in the X-band for the microwave frequency at 9.4 GHz and the Q-band for the microwave frequency at 34.6 GHz. The X-band FMR spectrometer is either Varian E-line spectrometer or Bruker EleXsys. The Q-band FMR measurements were made using Bruker EleXsys E 500 system.

The samples were mounted onto the flat side of a quartz sample rod with sample surface being horizontal in the cavity. Upon rotation of the sample rod, the sample rotated horizontally in the cavity with the applied field in the plane of the film. Angle dependent FMR was done for rotations from 0º to 180º for these samples.

The size of the resonance cavity is determined by the microwave frequency. The higher the microwave frequency is, the smaller the cavity size. Because of the limitations of the cavity size for the Q-band measurement, the sample had to be cut into less than 1.6 mm in dimension. The samples deposited onto GaAs(001) substrates were cut into less than 1.5 mm by 1.5 mm squares with edges along the [110] and [1-10] directions. The samples that were deposited onto GaAs(110) substrates were cut into 1.5 mm by 1.5 mm

squares with one of the edge along the [111] direction and the other edge perpendicular to the [111] direction.

To compare the results in the X-band and the Q-band, the same samples were used in the two frequency measurements.

EXPERIMENTAL RESULTS

To investigate the Ga concentration and $Fe_{1-x}Ga_x$/ZnSe interface effect on the magnetic properties of $Fe_{1-x}Ga_x$ films, two series of samples were deposited on both ZnSe(001) and ZnSe(110) surfaces.

The samples prepared to investigate the Ga concentration effect were: Pure Fe, and iron doped with 4.5%, 7%, 11%, 15%, 20%, 21%, 23%, 36%, 38%, 45% and 57% Ga grown at about 20 nm thickness on ZnSe(001) and Fe with 0%, 15%, 20%, 21%, 23%, 33%, 38% and 45% Ga grown at about 20 nm on ZnSe(110) surfaces.

The samples used to study the FeGa/ZnSe interface effects were 21% Ga doped samples prepared at different thicknesses. The samples were at thickness of 2.4 nm, 4.8 nm, 9.9 nm, 19.8 nm and 39.7 nm on ZnSe(001) surfaces and at 10 nm, 20 nm and 40 nm thickness films on ZnSe(110) surfaces.

To see the consistency of the measurements and magnetic field effect on magnetic anisotropies for those samples, both the X-band and the Q-band FMR measurements have been performed on the same samples and the results have been compared.

Example Spectra

The FMR spectra were collected with fixed microwave frequency resonance at the sample cavity. The magnetic field was slowly scanned from low field to high field while a spectrum was recorded. For a better sensitivity, the FMR spectra were recorded in the derivative form of the absorption signal. The peak of the signal occurs at the zero

crossing of the derivative spectrum. We define this point as the resonance field (H_{res}). Figure 46 shows pure Fe spectra in the X-band and the Q-band for two different rotations.

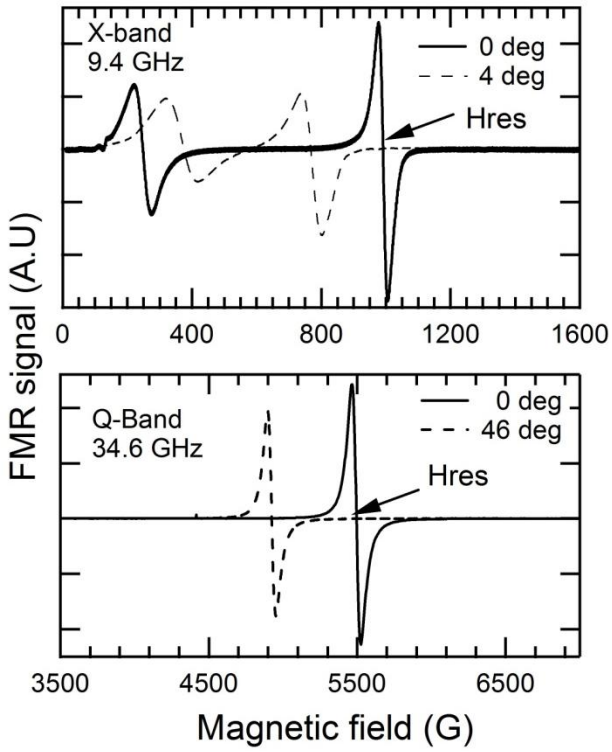

Figure 46: Typical FMR spectra in X band and Q band along different rotations. Top panel plots X band spectra and bottom panel plots Q band spectra for the same pure Fe film.

Comparing the X-band and Q-band spectra, we noticed that for the X-band FMR, the resonance happens at ~1000 Oe, while for the Q-band FMR, the resonance happens at a much higher field for the same sample. In the X-band, figure 46 shows a 0º rotation and 4º rotation spectra. It is shown that two resonance peaks appears. Both the peaks have large resonance field shifts upon a 4º rotation. The appearance of the two resonance lines occurs because the internal field creating a precession frequency that is close to the microwave frequency. The first resonance peak that is in the low magnetic field

corresponds to where the magnetization is not aligned with the applied magnetic field. The second resonance peak, which occurs at a higher magnetic field, corresponds to the situation where the magnetization of the sample is aligned with the applied field. While in the Q-band spectra, there is one resonance peak showing up at about 5000 Oe and the resonance field also shifts as angle changes.

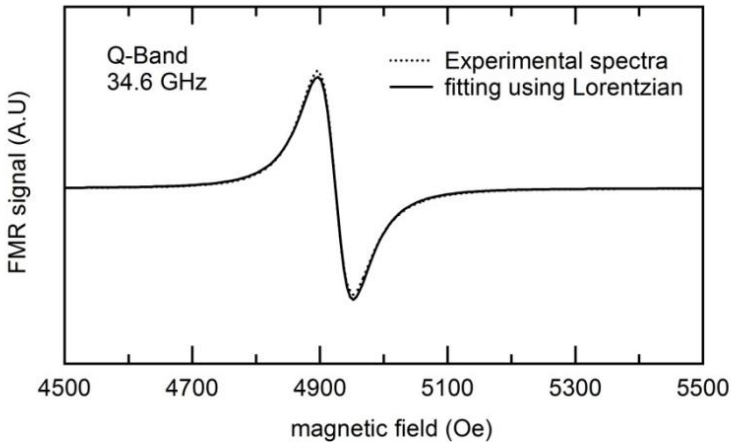

Figure 47: Example spectra with fitting using derivative of Lorentzian.

The spectra have been fitted using the derivative of the Lorentzian function:

$$f(x) = -2A\omega_0(x-x_0)/((x-x_0)^2+\omega_0{}^2)^2 + kx + c \quad . \tag{27}$$

where A is the amplitude of the signal, ω_0 is the full width half maximum of the Lorentzian function, and x_0 is the resonance field H_{res}. C and k terms are to compensate for the offset and a background subtraction. There are two ways to define linewidth. One is to use the full width half maximum, where the linewidth will be the ω_0 in the Lorentzian function. The other is to use the inflection points on the derivative form of the spectra to get linewidths. In this way, the linewidth is $\sqrt{3}/3$ of ω_0 from the full width half

maximum. Figure 47 shows an example spectrum with the fitting using the derivative of Lorentzian function.

Full Angular Resonance Field

After making the full angular rotation measurement from 0º to 180º, we extracted resonance fields (H_{res}) and linewidthes using the Lorentzian fit. A polar plot was then made for the whole angular rotation. Figure 48 shows the whole angular rotation plot of the resonance field for pure Fe deposited on ZnSe(001) in the X-band. Figure 49 shows the Q-band results for the same pure Fe sample. It can be seen that both the X-band and the Q-band resonance fields versus angle data have four-fold symmetry. Along the <110> directions, the resonance fields are highest. The big difference between the two plots is that the X-band and the Q-band resonances happen at very different fields. The X-band resonance fields are around 1000 Oe while the Q-band resonance fields are around 5000 Oe. In the X-band, resonance only occurs at a certain angle while at other angles, the resonance disappears. In the Q-band measurement, the resonance fields show up for the whole angular rotation. This is because the X-band resonance frequency 9.4 GHz is so low that in some angles, the internal field is high enough to generate a precession frequency of the magnetic moment equal to or greater than the microwave frequency. So applying a field in the same direction as the internal field will only increase the precession frequency of the magnetic moment, producing no resonance peak. When the sample was rotated to different angles, the internal field can be in different directions from the applied field and will decrease the precession frequency, possible to make resonance happen. This effect can be seen from the X-band FMR data in Figure 48. Since

the Q-band frequency is 34.6 GHz, the internal field is not large enough to generate a precession frequency higher than that. This is why complete angular resonance field plots for high frequency measurements are always observed. The angular plots show that the easy axes are in the [100] directions and hard axes are in the [110] directions.

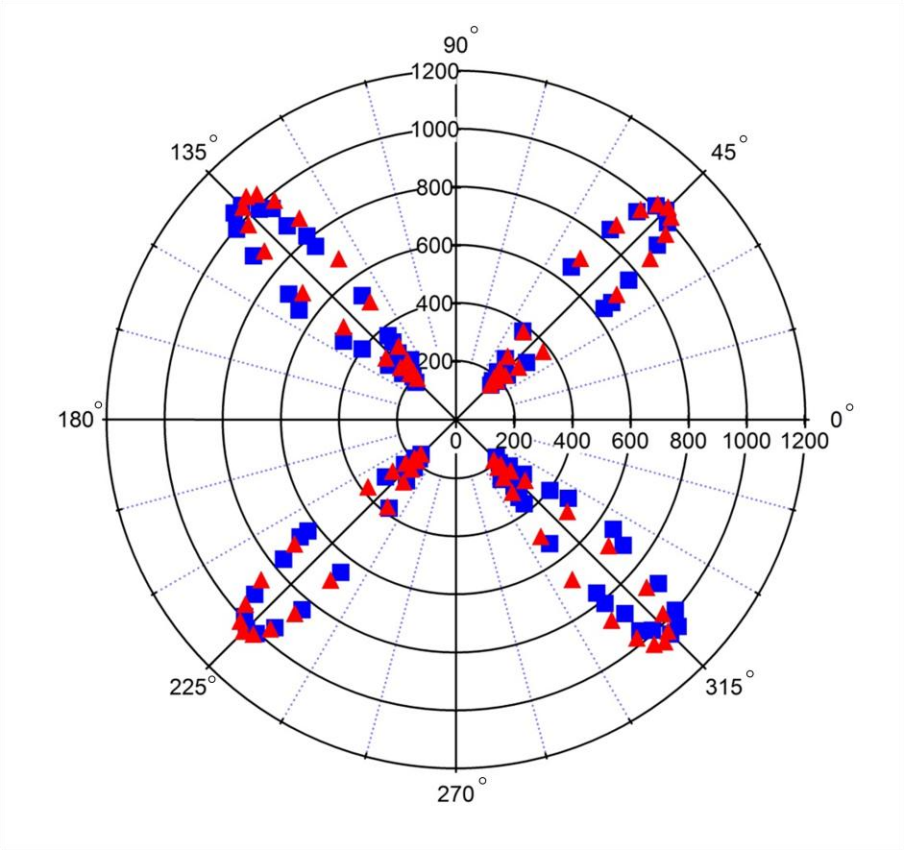

Figure 48: X-band resonance field versus angle plot for pure Fe/ZnSe(001). 0º is in the [100] direction. The blue squares are the experimental data and the red crossings are the fits.

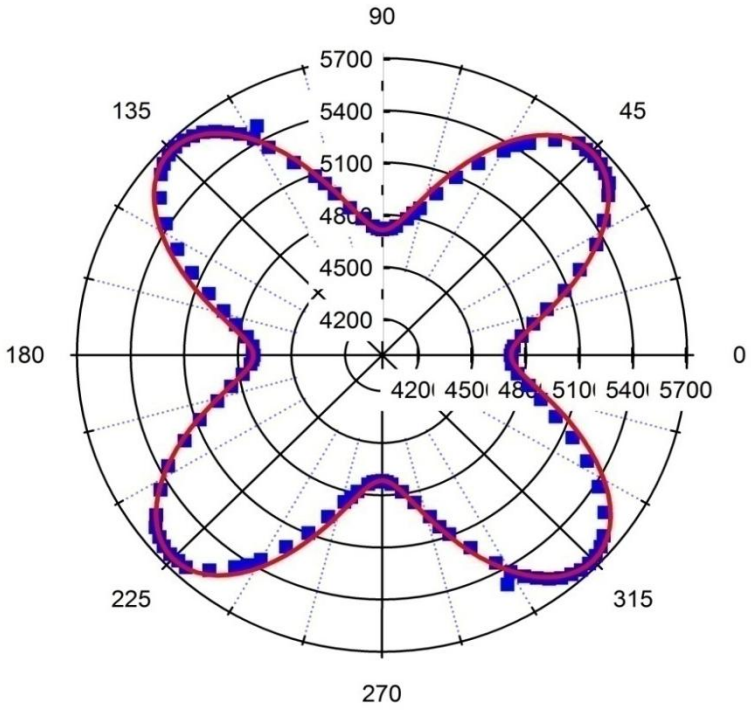

Figure 49: Q-band resonance field versus angle plot for pure Fe/ZnSe(001), 0º is in the [100] direction. The blue squares are the experimental data and the line is the fit to the data.

Fitting to the Resonance Fields

From the experimental resonance field versus angle data in Figure 48 and 49, we can see that the magnetic anisotropy is of a cubic term. There is a slight difference on the resonance field at 45º and 315º which indicates a uniaxial term in the [110] direction. The uniaxial term is more prominent in Ga doped samples, as will be shown later. We follow Krebs [10] and Artman [83] to use a magnetostatic energy term plus a cubic anisotropy term, an in-plane uniaxial term, a demagnetization term and an out-of-plane uniaxial term as shown in Equation (28) to represent the energy density.

$$E = -M \cdot H + K_1(\alpha_1^2\alpha_2^2 + \alpha_2^2\alpha_3^2 + \alpha_1^2\alpha_3^2) + K_u \cos^2(\Theta + \tfrac{1}{4}\pi) + 2\pi M_\perp^2 + K_\perp (M_\perp / M)^2 \quad . \qquad (28)$$

Here the first term is the magnetostatic energy. The second term is the cubic crystalline anisotropy energy, where K_1 is the usual fourth-order cubic anisotropy constant, making the easy-axis along <100> when it is positive. The third term is uniaxial in-plane magnetic anisotropy energy, with K_u the uniaxial second order anisotropy constant. The fourth term is the demagnetic field. The fifth term accounts for any perpendicular anisotropy energy. The fourth term and the fifth term have the same dependency on the azimuth angle, so these two terms are combined and $\tilde{Kp} = 2\pi M^2 + Kp$ is used in the fittings. The α's are the directional cosines of M with crystal axes [100], [010] and [001]. Θ is the angle between M and in-plane [100] axis. Anisotropic energy K_1, K_u, and K_p and magnetization M can be determined using ω versus H relation.

In FMR fittings, K_1, K_u and $\tilde{K}_p$ can not be independently extracted because they are linearly dependent on the magnetization M values used in the fitting. However, K_1/M, Ku/M and $\tilde{K}_p/M$ are always valid parameters and do not depend on the magnetization M values. In this dissertation, either K/M values or modified K values are reported. The modified K values are defined as: $K_{\mathrm{mod}} = M_{vsm} K/M$, where K/M are values from fitting and M_{vsm} are measured magnetization values from VSM. Effective magnetization can be calculated as $2\pi M_{eff} = \tilde{K}_p/M$,where $\tilde{K}_p$ is the total uniaxial perpendicular anisotropy energy, and M is the magnetization value used in the fitting procedure.

Figure 48 and 49 show the fittings to the X-band and the Q-Band data for the pure Fe sample using Equation (28). The fitting parameters for the X-band data are M_{eff} = 1572

emu/cm^3, K_1/M_{eff} = 270 Oe, and K_u/M_{eff} = 4.7 Oe. The fitting parameters for the Q-band data are M_{eff} = 1709 emu/cm3, K_1/M_{eff} = 268 Oe, and K_u/M_{eff} = 4.2 Oe. The fitting parameters are close to each other except for the effective magnetization value.

Quality Determination of a Thin Magnetic Film from FMR Measurements

The other useful information we can get from FMR spectra is the quality of the films. We can tell the quality of the magnetic thin films from linewidth, resonance field shift and number of peaks. A sharp linewidth always indicates a good film growth. For polycrystalline samples, the linewidth will be large due to the inhomogeneous broadening. A good film will have a large magnetic anisotropy and will result in a large resonance field shift upon changing the rotation angle while polycrystal films normally show no or small angular resonance field shifts. For a film, if only one peak is expected but there are multiple peaks, it shows that the film is not single crystal. The multiple peaks come from different crystal orientations or different crystal properties. For example, in our samples for Fe deposited on the ZnSe(001) surface, the sharpest full width half max (FWHM) linewidths for pure Fe are 39 Oe in the Q-band and 22 Oe in the X-band (From fittings using Lorentzian function). This is comparable to the literature of 45 Oe in the Q-band for pure Fe/ZnSe(001) [9]. From Figure 47 and 49, we see that there is only one FMR line showing up in the Q-band and the resonance field has a decent angular dependence. These indicate a good film growth.

For one of our Fe/GaAs(110) sample without the ZnSe buffer layer, we see multiple lines in the FMR as shown in Figure 50. Those lines shift together when we make the angular rotation. All the lines have a minimum at the same angle. So we suspect

there are multi-layers of films that have different magnetic anisotropy constants, but the crystal orientations are the same for all the layers.

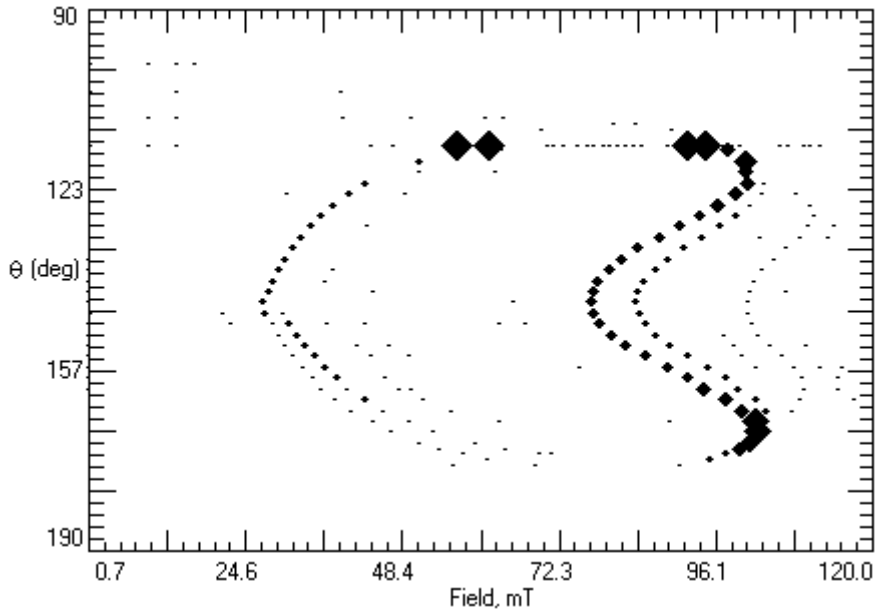

Figure 50: Angular FMR for Fe/GaAs(110) with no buffer layer.

While for one of our Fe/MgO(001) samples, whose resonance field has been shown in Figure 51, the multi-lines of the FMR have different maximum and minimum resonance field angles and the shifts for these two lines are the same except an angle shift. So the two lines correspond to two different film domains that have almost the same magnetic anisotropy while the crystal orientations are slightly tilted at different angles.

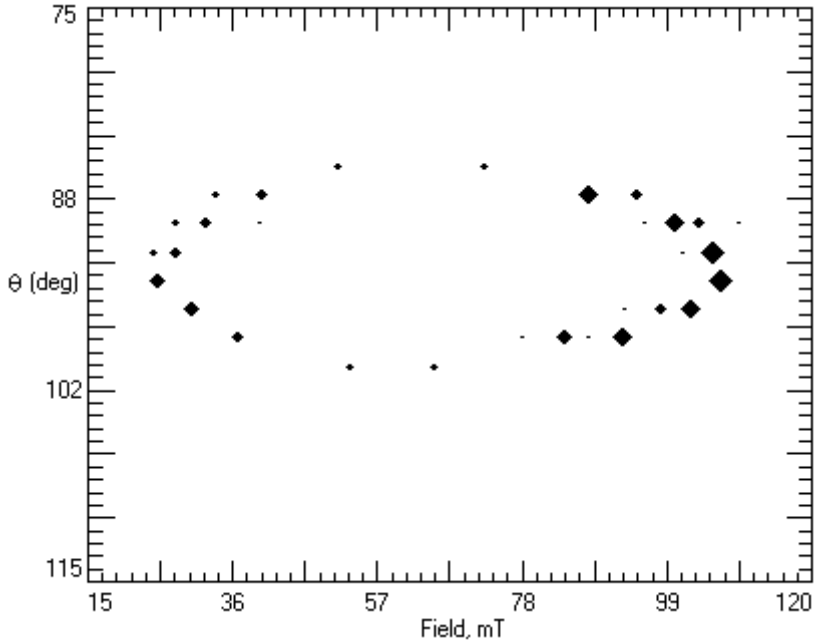

Figure 51: Angular FMR for Fe/MgO(001)

Comparison between the X-band and
Q-band Data for the Same Samples

In the previous section, we have listed resonance field shifts for pure Fe on ZnSe(001) in the X-band and Q-band. We have noticed some similarities and the differences. Below we will compare resonance field shifts and linewidths for 20% and 23% Ga doping in ZnSe(001) in the X-band and the Q-band for the same samples.

Figure 52 shows the resonance fields in the X-band and Q-band data for the same 20% Ga doped FeGa sample grown on ZnSe(001) surface. It can be seen that unlike for pure Fe, the 20% sample has full angular data in the X-band. This is because the de-magnetic field is smaller after doping so the total internal field gets smaller, resulting in the lower natural precession frequency. The other big difference compared with the pure

Fe sample data shown before is the big inequality of the resonance field at 45º and 135º. For pure Fe, the difference is only about 10 Oe, while for the 20% Ga doped sample, the difference is about 190 Oe. For the 20% Ga sample, we can barely see a cubic symmetry but we can see a big uniaxial symmetry.

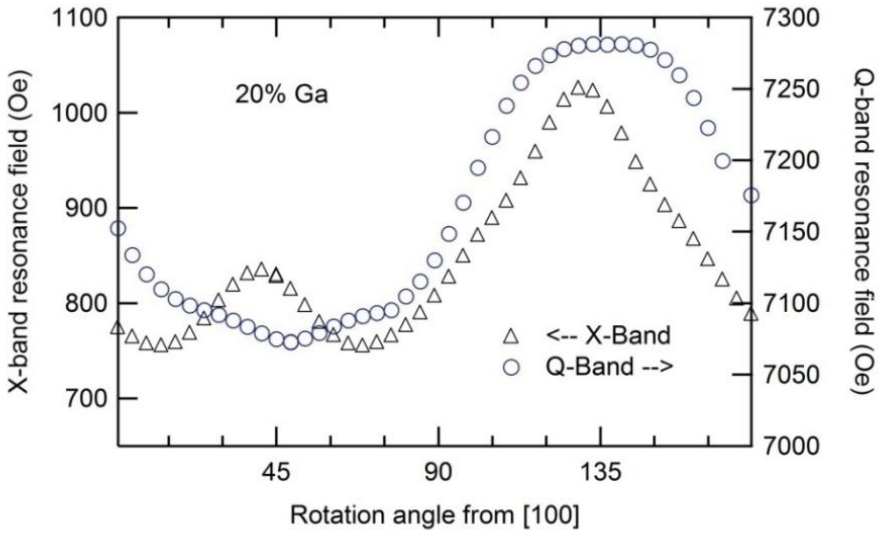

Figure 52: Resonance fields in the X-band and Q-band for the 20% Ga sample.

Comparing the Q-band data with the X-band data, we notice that these two measurements generated similar results except a slight change over the relative size of cubic anisotropy and uniaxial anisotropy. The linewidths in both X-band and Q-band are shown in Figure 53. It has much simpler pattern than the resonance field. Even though the magnetic anisotropy shows the uniaxial symmetry, the linewidths show only cubic symmetry.

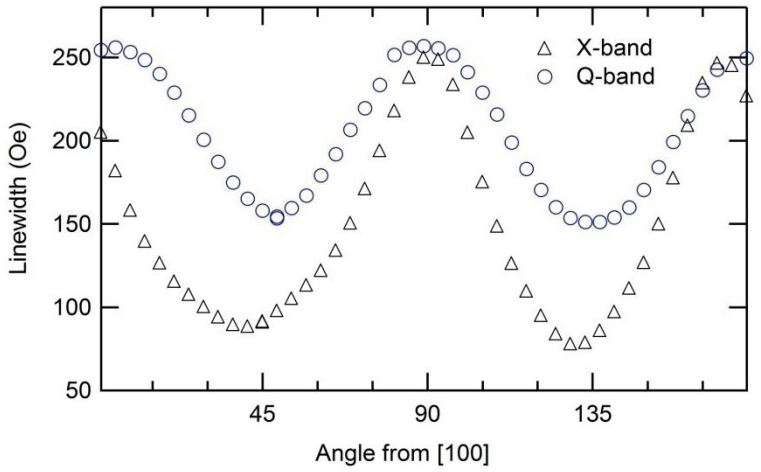

Figure 53: X-band and Q-band linewidthes for the $Fe_{0.8}Ga_{0.2}$/ZnSe(001) sample.

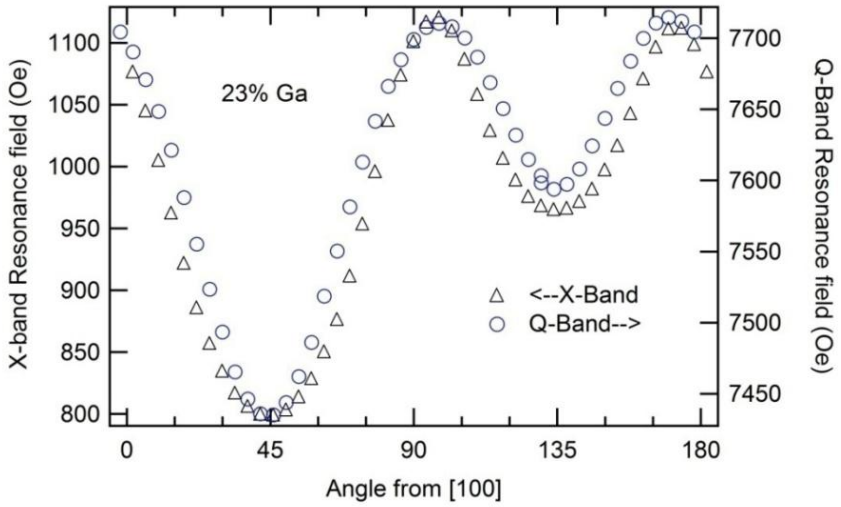

Figure 54: Resonance fields in the X-band and Q-band for the $Fe_{0.77}Ga_{0.23}$/ZnSe(001) sample.

Figure 54 shows the resonance fields for the 23% Ga sample in the X-band and Q-band. In the 23% Ga doped sample, we notice that the cubic term re-appeared. But the [100] direction becomes a hard axis, which means that cubic anisotropy K_1 is a negative term. The uniaxial terms show a slight difference in the X-band and Q-band data, which

can be seen from the 45 degree and 135 degree data. The difference in the 20% Ga is slightly larger than the difference in the 23% Ga sample.

Magnetic Anisotropies for $Fe_{1-x}Ga_x$/ZnSe(001)

Different Concentration Samples

In the following section we will discuss the results for pure Fe, and iron doped with 4.5%, 7%, 11%, 15%, 20%, 21%, 23%, 36%, 38%, 45% and 57% Ga grown at about 20nm thickness on ZnSe(001) from both the X-band and the Q-band FMR.

Figure 55 through 60 show X-band and Q-band Hres versus angles data for several Ga concentrations. It is shown that when Ga concentration is less than 20%, the [100] direction is an easy direction. While at 20% Ga doping, the cubic anisotropy almost disappeared. It is also shown that when Ga concentration gets more than 20%, the cubic anisotropy switches its easy and hard axis direction.

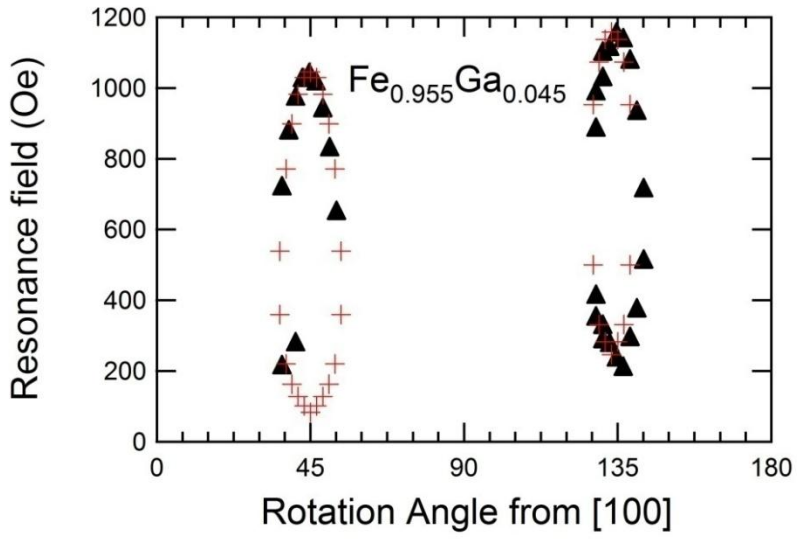

Figure 55: X-band angular resonance fields for $Fe_{0.955}Ga_{0.045}$/ZnSe(001). The black triangles are the experimental data. The red crosses are the fittings to the data.

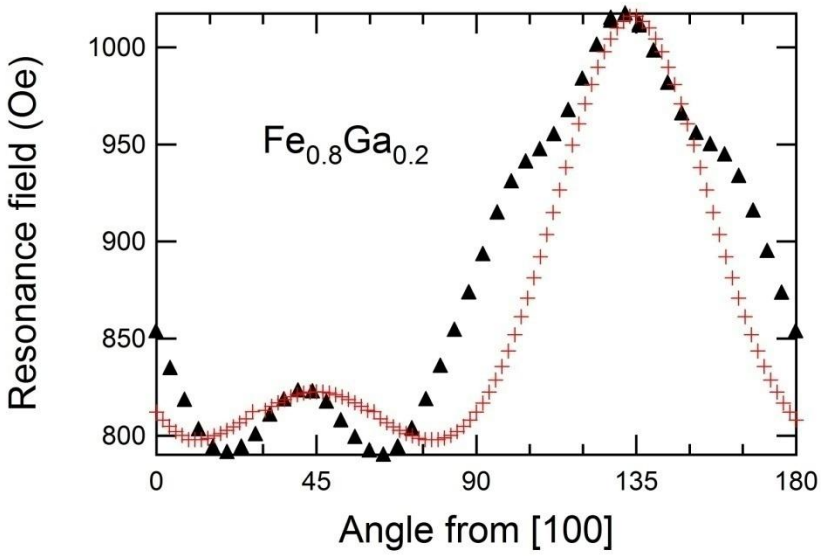

Figure 56: X-band angular resonance fields for $Fe_{0.8}Ga_{0.2}$/ZnSe(001). The black triangles are the experimental data. The red crosses are the fittings to the data.

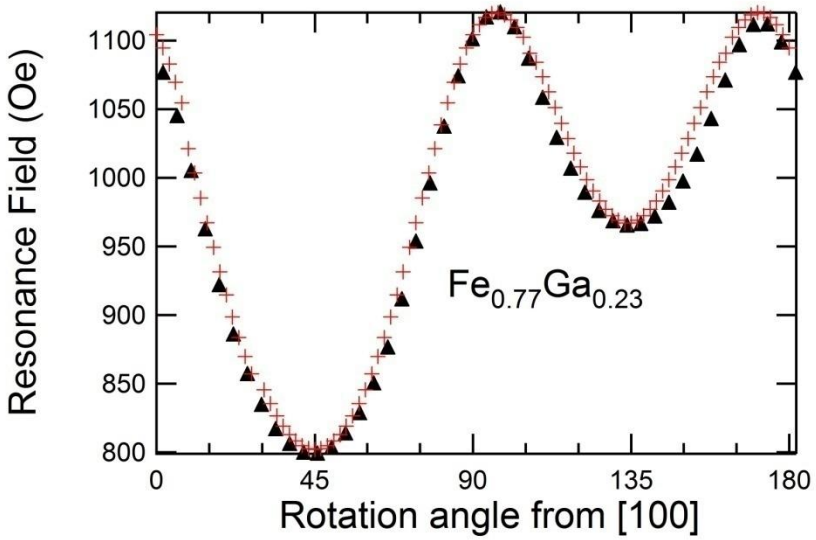

Figure 57: X-band angular resonance fields for $Fe_{0.77}Ga_{0.23}$/ZnSe(001). The black triangles are the experimental data. The red crosses are the fittings to the data.

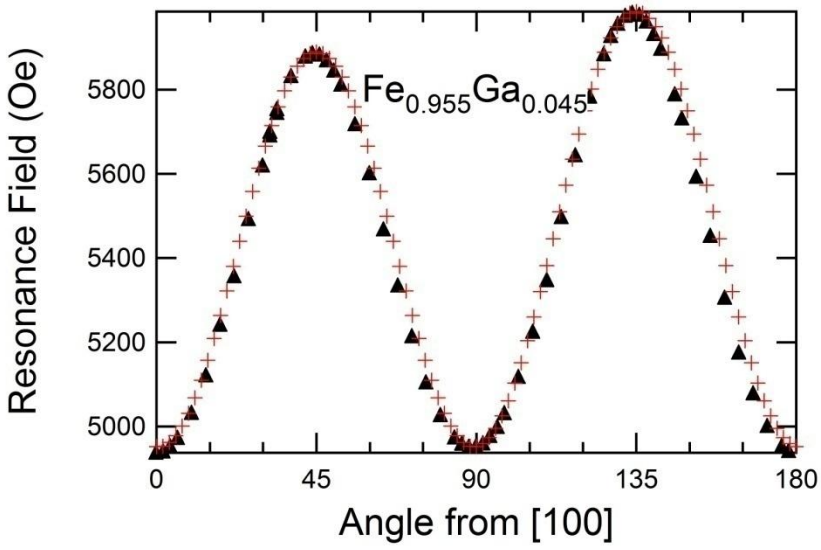

Figure 58: Q-band angular resonance fields for $Fe_{0.955}Ga_{0.045}$/ZnSe(001). The black triangles are the experimental data. The red crosses are the fittings to the data.

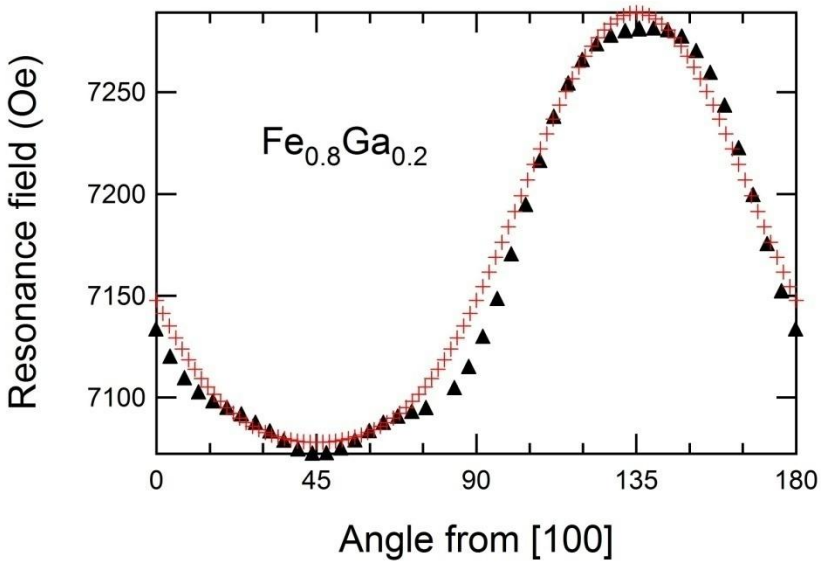

Figure 59: Q-band angular resonance fields for $Fe_{0.8}Ga_{0.2}$/ZnSe(001). The black triangles are the experimental data. The red crosses are the fittings to the data.

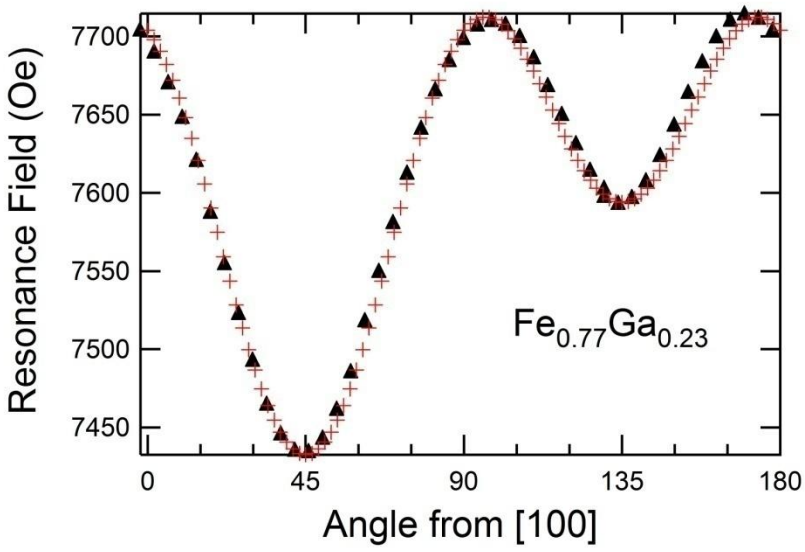

Figure 60: Q-band angular resonance fields for $Fe_{0.77}Ga_{0.23}$/ZnSe(001). The black triangles are the experimental data. The red crosses are the fittings to the data.

From the comparison of above measurements in the x-band and Q-band, we see that X-band and Q-band show similar behaviors for most of the samples except for the 20% Ga doped sample, we think the reason for the discripensy between the Q-band data and X-band data comes from the no-uniformity of the sample. Especially at 20% Ga doping, the cubic anisotropy and B2 changed sign, so the no-uniformity will generate different field dependent in the films for different Ga concentration regions and show up on the magnetic anisotropy.

Magnetization

Saturation magnetizations for these films were measured using the PPMS vibrating sample magnetometer (VSM). Effective magnetizations can also be extracted from angular FMR fitting using $2\pi Me_{ff} = \tilde{K}_p / M$. Effective magnetization means that any

perpendicular magnetic anisotropy is ignored, and that the d-magnetic field is assumed to be the only perpendicular magnetic anisotropy source. Figure 61 shows the effective magnetization from the FMR fitting procedure and from VSM measurements. Magnetizations from these two measurements track each other closely. For pure Fe, the magnetization from Q-band measurement is 1709 emu/cm^3, which is slightly lower than the reported bulk value of 1714 emu/cm^3. The reason for the difference might be that magnetoelastic anisotropy generates a negative surface anisotropy [8]. With doping of Ga, magnetization decreases linearly but remains lower than the pure dilution line. It drops to 482 emu/cm^3 at 36% Ga concentration. XMCD data [84] has shown that the Fe moments change upon doping of Ga, also the Fe induced magnetic moments for the doped Ga and the magnetic moment of Ga is anti-aligned with the Fe moment. All these will lower the total magnetization from the pure dilution line. With the increase of Ga doping, the slope of the magnetization changes. This change is caused by a structure change at 20% Ga doping as can be seen from the XMLD measurement [85]. The measurement results show the same trend as bulk Fe_xGa_{1-x} materials [5, 86]. The difference between VSM measurement values and FMR measurement values might come from thickness measurements in VSM measurements and perpendicular anisotropy being counted as part of the demagnetic field in the FMR analysis.

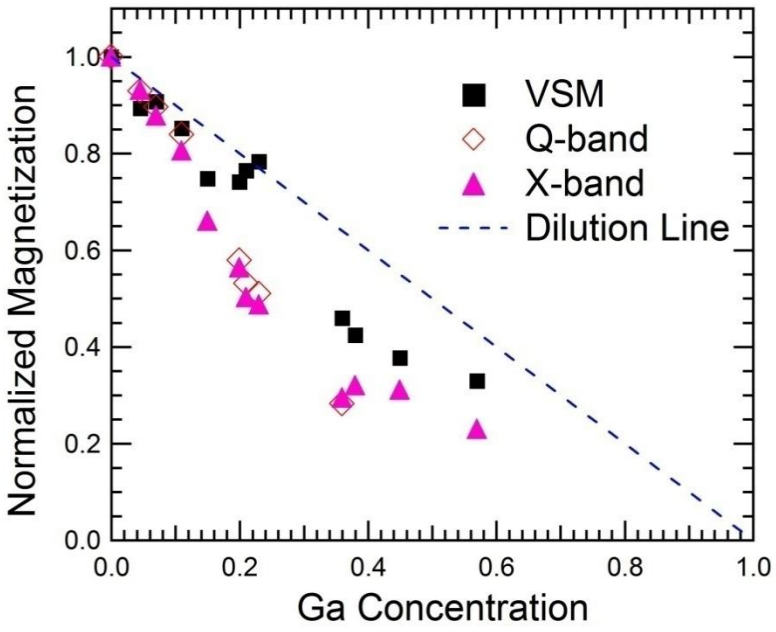

Figure 61: Saturation magnetization measured from VSM and effective magnetization extracted from FMR fittings in X-band and Q-band.

Cubic Magnetic Anisotropy Constant K_1

Cubic anisotropy comes from crystalline anisotropy. Nature of the BCC cubic structure determines that this crystal has cubic anisotropy. K_1 values have been extracted using the fitting data K_1/M and the magnetization value M_{vsm} from VSM measurement. Figure 62 shows the cubic anisotropy constant K_1 versus Ga concentration data. When Ga concentration is low, cubic anisotropy dominates and along [100] is the easy axis for K_1 term, so K_1 is positive. As Ga concentration increases to 20%, the cubic anisotropy decreases to zero. As Ga concentration increases even more, cubic anisotropy K_1 changes sign, and cubic anisotropy's easy and hard axes rotate 45º. Now [100] becomes the hard axis for the cubic term and [110] becomes the easy axis. As can be seen from Figure 62, for pure Fe, K_1 is 458839 erg/cm^3 (K_1/M is 267.7 Oe). It is very close to K_1 for Fe bulk at

4.8×10^5 erg/cm^3. The K_1/M value is close to the value of 290 Oe for BCC Fe on ZnSe [10]. As Ga doping increases, K_1 quickly drops to zero around 20%, and stays at negative, and then slowly increases in value as Ga increases. K_1 increases to about -118000 erg/cm^3 at 36% Ga, and then starts to decrease toward zero as doping increases. Comparing this behavior with Cullen's measurement for bulk $Fe_{1-x}Ga_x$ samples using VSM [6], their K1 values use (J/m3) as the unit, and 1 j/m3 is equal to 10 (erg/cm3), so the values are from out thin film samples are close to the bulk value and also have similar patterns as doping of Ga. The difference might be that their samples are un-constrained samples and our samples are thin film samples constrained by the substrate, so the second order magnetoelastic effect makes the difference on the K_1 value.

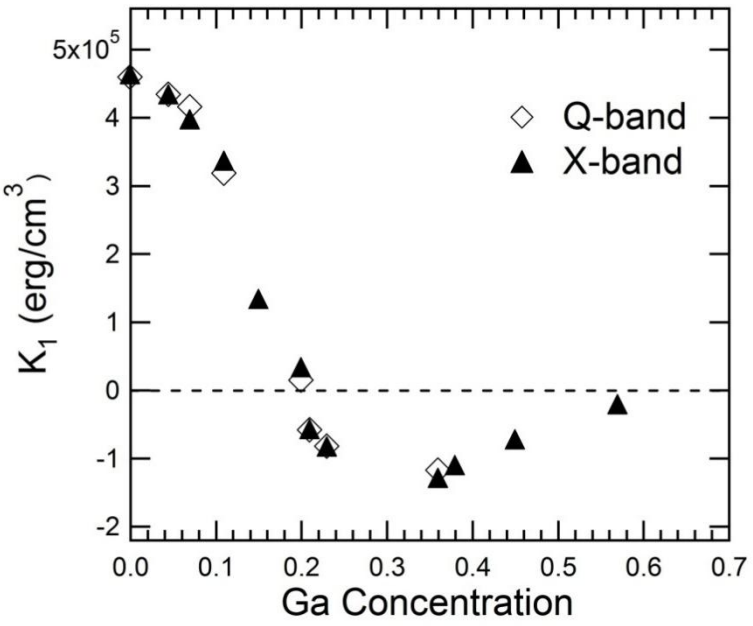

Figure 62: Extracted K_1 values from X-band and Q-band FMR fitting. Diamonds show the Q-band data and the solid triangles show the X-band data.

Uniaxial Anisotropy K_u

Figure 63 shows the concentration dependence of the modified uniaxial anisotropy constant K_u. For pure Fe, the uniaxial term is small (7.7×10^3erg/cm^3) with easy axis in the [110] direction. The easy axis is in the same direction as Fe deposited on GaAs(001) [34, 43, 45, 61, 64, 69, 79, 87] and as Fe on ZnSe(001) [10, 11, 48, 52, 88]. As Ga doping increases, uniaxial anisotropy suddenly increases to a higher value. It reached 9.14×10^4 erg/cm^3 for 20% Ga. When doping exceeded 30%, easy axis switched to [1-10] direction. The easy axis direction is different from Thomas's [73] data but still can be explained using the uniaxial strain relaxation theory as predicted by Mirbt [36]:

$$E_u = \tfrac{1}{2} B_2 \varepsilon_{12} sin(2\Theta) \tag{29}$$

Here E_u is the uniaxial anisotropy generated by the uniaxial relaxation in [110] direction. B_2 is the magnetoelastic coupling coefficient as shown in Equation 4, ε_{12} is the shear strain, and Θ is the angle between the magnetization and the [100] direction. As Ga dopping increases, according to Equation 5, the lattice mismatch will increase, so we expect ε_{12} to increase, which causes the uniaxial anisotropy to increase. But the B_2 value changes sign at 20% for bulk material [3] which means that for the same share strain ε_{12}, the energy term E_u will change sign. This will cause the easy axis to change direction. But the fact that the easy axis did not switch direction until after 23% Ga doping indicates the presence of another surface term that will hold the easy axis direction to [110] direction, so it will delay the switching of easy axis as a function of doping.

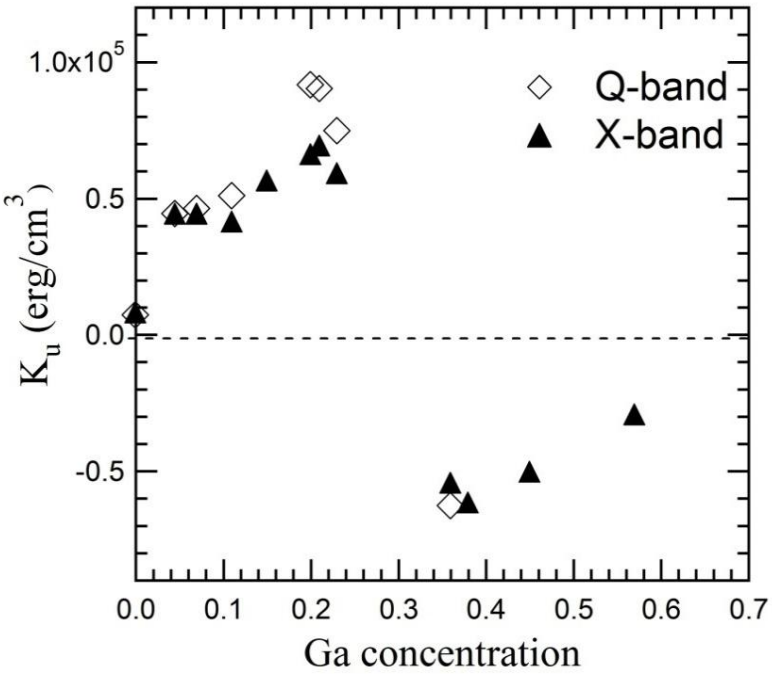

Figure 63: Extracted K_u values from X-band and Q-band FMR measurements. Diamonds show the Q-band data and the solid triangles show the X-band data.

In our experiment, K_u values measured in the X-band are always lower than those measured in the Q band. We attribute that to the field dependent strain ε_{12}. As field goes higher, $|\varepsilon_{12}|$ increases, generating a higher Ku value in the Q-band.

B_2 is positive when x is less than 20%. To get easy axis in the [110] direction, ε_{12} needs to be negative, so the [1-10] direction is more relaxed than [110] direction. The relaxation direction is different from Thomas's [73] but agrees with Mirbt's theoretical calculation. To see if this effect is really due to anisotropic relaxation, additional experiments need to be carried out.

Different Thickness Samples

In the following section, we will discuss the effects of thickness on magnetization and magnetic anisotropy for 21% Ga doped samples at thickness of 2.4 nm, 4.8 nm, 9.9 nm, 19.8 nm and 39.7 nm on ZnSe(001) surfaces.

Since inter-diffusion happens at the interface, lattice mismatch, and interface bonding, the interface might induce additional anisotropy or form a magnetic dead layer. To investigate the interface effects, different thickness samples have been grown at 21% Ga doping. For different thickness samples, K/M values have been reported because magnetization values change for different thicknesses.

Magnetization: In order to find the surface effect, we plotted effective magnetization × thickness for different thicknesses. Figure 64 shows the magnetic moment versus thickness plot. Magnetic moment increases with the increase of thickness. A straight line fitting to these data gives a dead layer of 1.6 nm. From the Q-band data, when the thickness is 2.4 nm, M_{eff} is as low as 375 emu/cm^3. It then goes to 912 emu/cm^3 at 40 nm. From the X-band data, M_{eff} goes from 240 emu/cm^3 to 1182 emu/cm^3 at 40 nm. A dead layer of 1.64 nm is extracted using Q-band data. X band M_{eff} is always smaller than Q-band M_{eff} (except the last point). Surface perpendicular magnetic anisotropy came from the lattice mismatch and can be written as $K_p = - B_1 \cdot (\varepsilon_\perp - \varepsilon_{||})$ [8], which can be extracted using $K_p^{eff} = K_{pv} + K_p^{int}/t$. The extracted values are M_{vol}=936 emu/cm^3, and K_p^{int} =1.2erg/cm^2 for the Q-band and M_{vol}=970 emu/cm^3, and K_p^{int} =0.84 erg/cm^2 for the X-band. In general, X-band K_p is smaller than Q-band K_p. This is because in the Q-band,

magnetic moments are lined up more in the applied field direction than in the X-band, so there will be a bigger de-magnetic field in the Q-band than in the X-band.

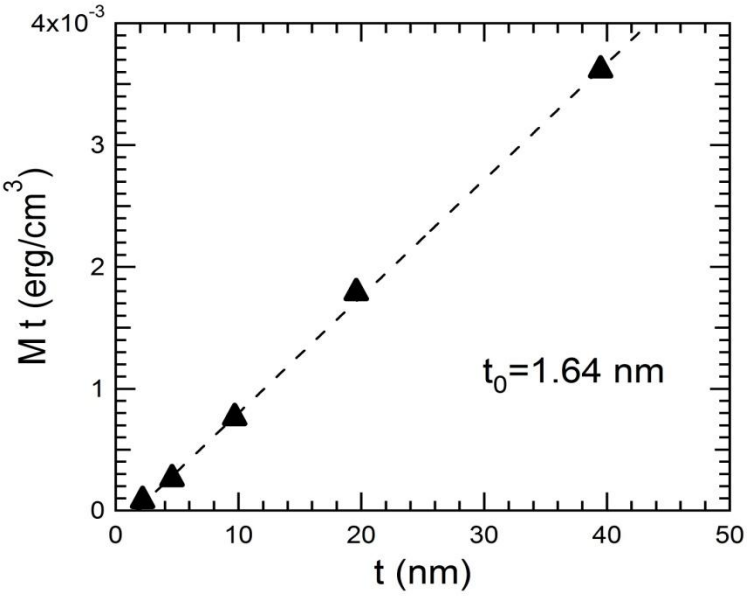

Figure 64: Effective magnetic moment multiplied by thickness versus thickness from Q-band FMR fitting. The straight line fitting gives a 1.64 nm dead layer.

$\underline{K_1^{int}}$ and $\underline{K_1^{bulk}}$: Thickness dependent K_1/M values are shown in Figure 65. The easy axis of the uniaxial term for these 21% Ga doped samples are always in the [110] direction for all the thicknesses. When thickness is very small, K_1 is almost zero. This suggests that in this thickness, crystal anisotropy has not formed.

For thickness greater than 2.4 nm, the thicker the films, the smaller the absolute K_1/M values. K_1/M values fluctuate a lot, which might be because the concentrations of these samples are slightly different. Q-band K_1/M starts from -88 Oe for 4.8 nm sample and goes up to -61.6 Oe for 40 nm sample. X-band K_1 starts from -113.8 Oe for 4.8 nm

sample and goes to -24 Oe at 40 nm. Bulk anisotropy K_{1bulk} and interface anisotropy K_{1int} can be extracted using $K_1^{eff}=K_1^{bulk}+K_1^{int}/(t-1.645)$. The extracted bulk value K_{1bulk}/M is -48 Oe for Q-band and -29.7Oe for X-band. Using magnetization of 936 emu/cm^3 for bulk 23% FeGa, K_1^{bulk} is -4.5×10^4erg/cm^3. Comparing this with the 20nm sample which has a K_1 value of -6.2×10^4 erg/cm^3, we see that 20 nm still has a big interface effect in it. K_1^{int} is -0.01erg/cm^2 in the Q-band and -0.025 erg/cm^2 in the X band. $K_1^{int} = K_1^{Fe/Al}+K_1^{Fe/ZnSe}$. The interface term is smaller than the reported values of $K_1^{Fe/ZnSe} = -2.8\times10^{-2}$ erg/cm^2, and -5.6×10^{-2} erg/cm^2 [11, 48].

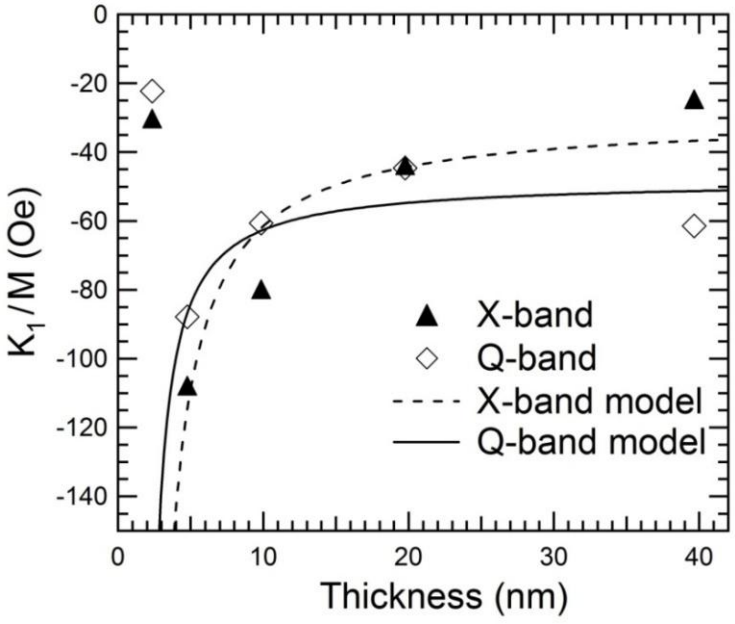

Figure 65: K_1/M values from X-band and Q-band FMR.

$\underline{K_u^{int}}$ and $\underline{K_u^{bulk}}$: For samples with 21% Ga concentration, the in-plane uniaxial anisotropy constants K_u/M are shown in Figure 66. K_u is largest when thickness is smallest. Q-band K_u/M starts at 204 Oe for 2.4 nm sample and drops to 44.8 Oe for 40 nm

sample. X-band K_u/M value is always about 20 Oe smaller than Q-band. It starts at 184 Oe at 4 nm and drops to 14.4 Oe at 40 nm. Surface and bulk effects are extracted using $K_u^{eff} = K_u^{bulk} + K_u^{\text{int}}/(t-1.645)$. The extracted K_u^{bulk}/M value is 70.9 Oe for the Q-band data and 49 Oe for the X-band data. Using magnetization of 936 emu/cm^3 (bulk value), K_u^{int} can be calculated as 0.0095 erg/cm^2 in the Q-band and as 0.0098 erg/cm^2 in the X-band. Compared with the uniaxial term for Fe/ZnSe $K_u^{\text{int}} = 5.9*10^{-2}$erg/cm^2 [48], K_u^{int} for $Fe_{0.77}Ga_{0.23}$ on ZnSe is much smaller than Fe/ZnSe.

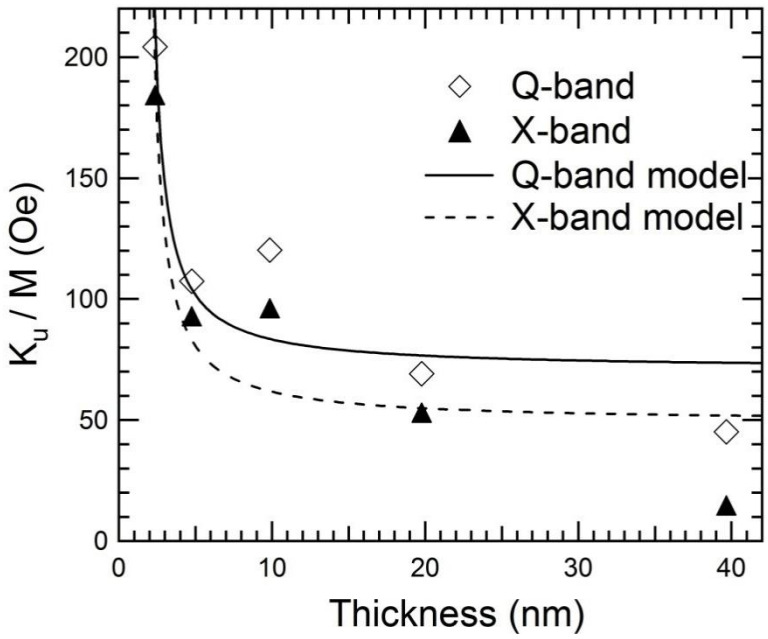

Figure 66: K_u/M values from X-band and Q-band FMR.

Summary

Measurements have been done on different Ga concentrations and different thickness samples using X-band and Q-band FMR. The extracted K_1 values from Q-band

and X-band FMR are almost the same. When Ga concentration goes from 0% to 60%, the cubic K_1 term goes from positive to about zero at 20% Ga concentration and then stays negative. From 21% Ga thickness data, extracted interface K_1^{int} is -0.01 erg/cm^2 for the Q-band and -0.025 erg/cm^2 for the X-band. Interface has a negative K_1^{int} value just as Fe/ZnSe. In general, K_1 values versus Ga concentration showed the same trend as bulk materials as in Figure 16.

The extracted K_u values from Q-band and X-band show slight differences. The K_u values extracted from X-band are always smaller than those from Q-band. The uniaxial easy axis was in the [100] direction when x is less than 20%, reached its peak at 20%, and then switched to [1-10] direction when x is greater than 30%. We suspect the uniaxial term comes from the uniaxial strain relaxation. The change of easy axis direction for uniaxial anisotropy energy is due to a B_2 sign change for different concentrations as shown in Figure 67 [3]. The difference in X-band and Q-band K_u values comes from the field dependence of ε_{12}. For different concentration samples, the biggest difference happens at 20% Ga concentration. From different thickness samples, the extracted Q-band K_u^{int} and X band K_u^{int} are almost the same. Anisotropic strain relaxation generates a uniaxial anisotropy [73]. When placed in magnetic field, the magnetic field will change the strain and might increase or decrease the anisotropy energy. In this case, the bigger the field is, the bigger the strain, making the uniaxial anisotropy increase.

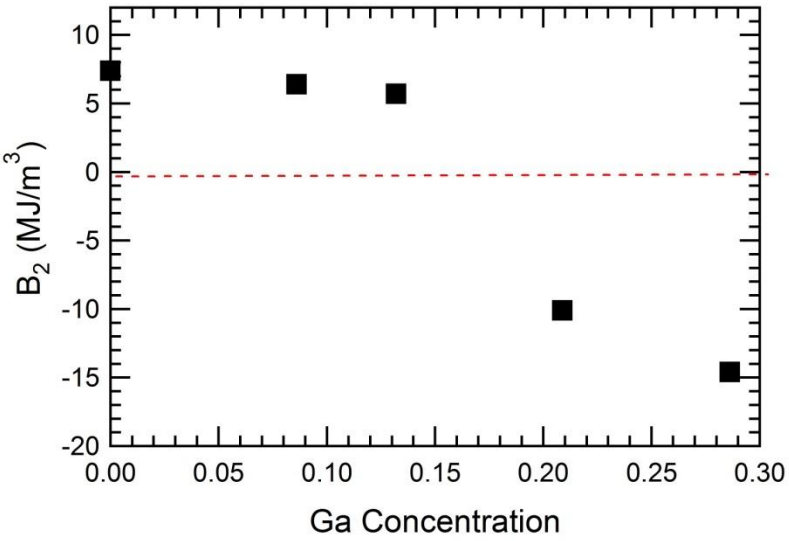

Figure 67: Calculated B_2 values for $Fe_{1-x}Ga_x$ from λ_{111}.

For very thin pure Fe film, From X band Varian data, the K_1/M value is 156.8Oe, K_p/M = 7424 Oe, K_u/M = 28.8 Oe.

For $Fe_{1-x}Ga_x$ system, there exist many phases for one composition. If those phases have different magnetic anisotropy, they will show multiple lines in the EPR measurement (we see multiple lines with multiple magnetic anisotropy values for $Fe_{1-x}Ga_x$ deposited on GaAs without ZnSe buffer layer). We do not observe multi magnetic anisotropy in the $Fe_{1-x}Ga_x$/ZnSe films, so only one phase exists in those films.

Magnetic Anisotropies for $Fe_{1-x}Ga_x$/ZnSe(110)

After studying $Fe_{1-x}Ga_x$/ZnSe(001), we have several reasons to study the $Fe_{1-x}Ga_x$/ZnSe(110) surface:

a. In contrast to standard molecular beam epitaxy growth, the method of cleaving the substrate in UHV and subsequent deposition has the advantage that atomically flat regions of up to several μm^2 in size and extremely clean surfaces are easily achieved [89].

b. The (001) oriented system is experimentally easier to prepare compared to the (110) oriented surface. However, it is known that GaAs(001) exhibits various surface reconstruction and growth conditions. Such complex surface structures are not expected in case of the nonpolar (110) surface. Therefore we concentrate here on Fe/GaAs(110) although the theoretical investigation is computationally more demanding because twice as many atoms are required in the calculation of the ideal interfaces without reconstructions [90].

c. The surface structure is different from (001) which can be seen from Figure 19.

   i) There are less directional bondings on (110) surfaces than on (001) surfaces. If the uniaxial term present on (001) surface is due to the bonding, we would expect the uniaxial term to be smaller on (110) surface.

   ii) There are two kinds of atoms, Zn and Se, on the surface of (110) while there is only one kind of atom on (001) surface. The Fe-Zn bonding and Fe-Se bonding have different bonding energies, which might cause different relaxation compared with the (001) surface.

Samples have been prepared at Ga concentration of 0%, 15%, 20%, 21%, 23%, 33%, 38% and 45%. These samples were cut into about 1.5 mm by 1.5 mm squares with

one edge parallel to the <111> direction. Sample orientation was confirmed with electron backscattering diffraction EBSD. FMR measurements were made using Bruker EleXsys E 500 system in the X-band (9.4 GHz) and the Q-band (34.6 GHz). The sample was put onto the end of the sample rod, with sample plane horizontal in the cavity. The sample was rotated horizontally in the cavity to take the in-plane angular FMR signal.

Figure 68 through Figure 72 show plots of magnetic resonance field versus angle data with fittings in the X-band. It is shown that there is a big uniaxial anisotropy term growing rapidly with doping of Ga, which makes the precession frequency in the easy axis direction large. So when the Ga concentration gets high, the X-band data only have few points in the hard axis direction.

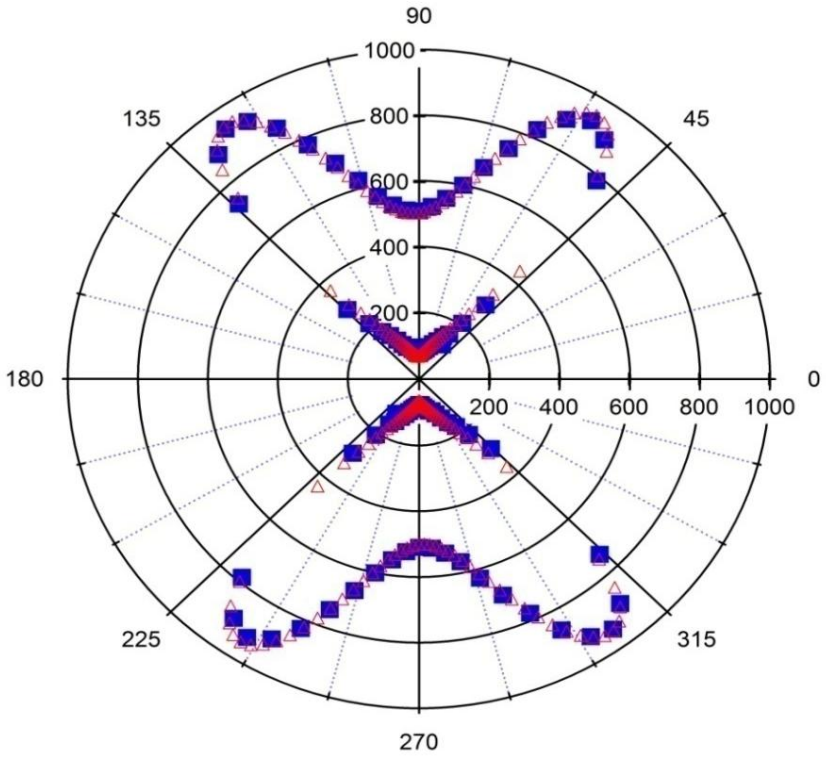

Figure 68: X-band resonance field for pure Fe/ZnSe(110) with fit. The black triangles are experimental data and the red crosses are fittings.

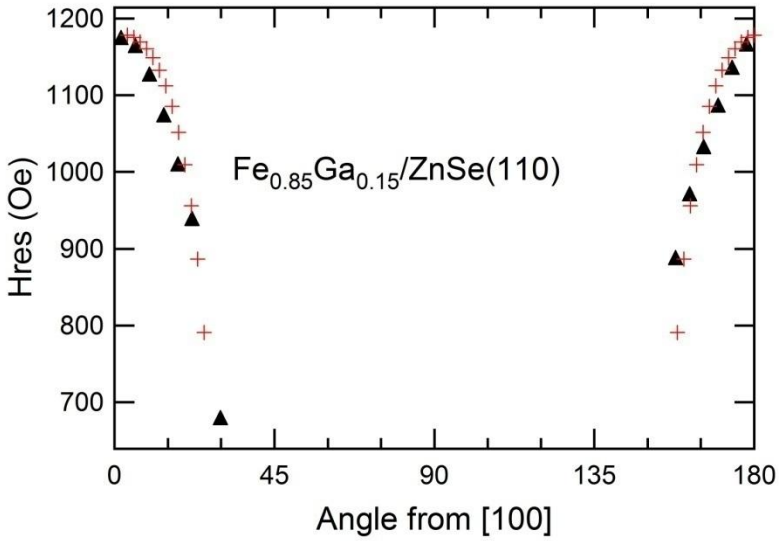

Figure 69: X-band resonance field for $Fe_{0.85}Ga_{0.15}$/ZnSe(110) data with fitting. The black triangles are experimental data and the red crosses are fittings.

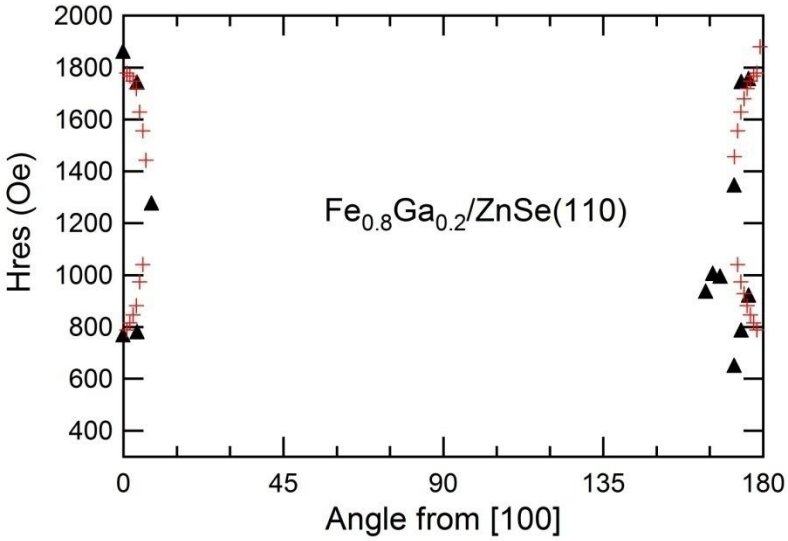

Figure 70: X-band resonance field for $Fe_{0.8}Ga_{0.2}$/ZnSe(110) data with fitting. The black triangles are experimental data and the red crosses are fittings.

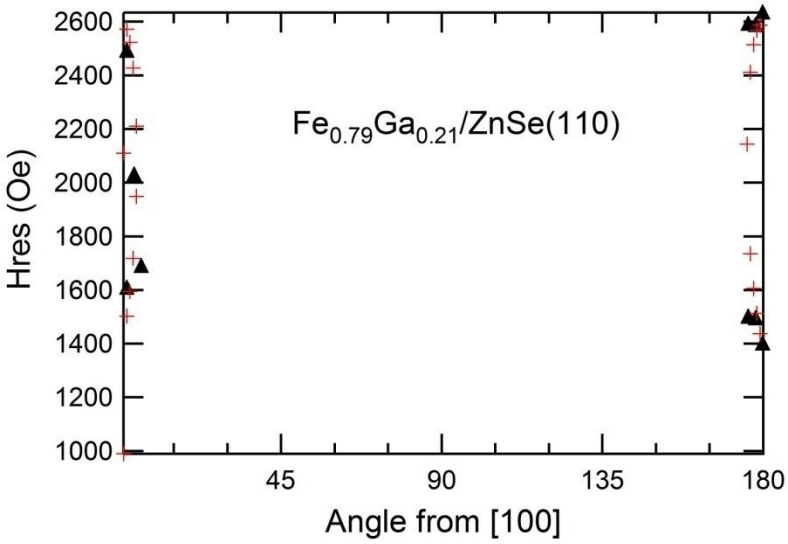

Figure 71: X-band resonance field for $Fe_{0.79}Ga_{0.21}$/ZnSe(110) data with fitting. The black triangles are experimental data and the red crosses are fittings.

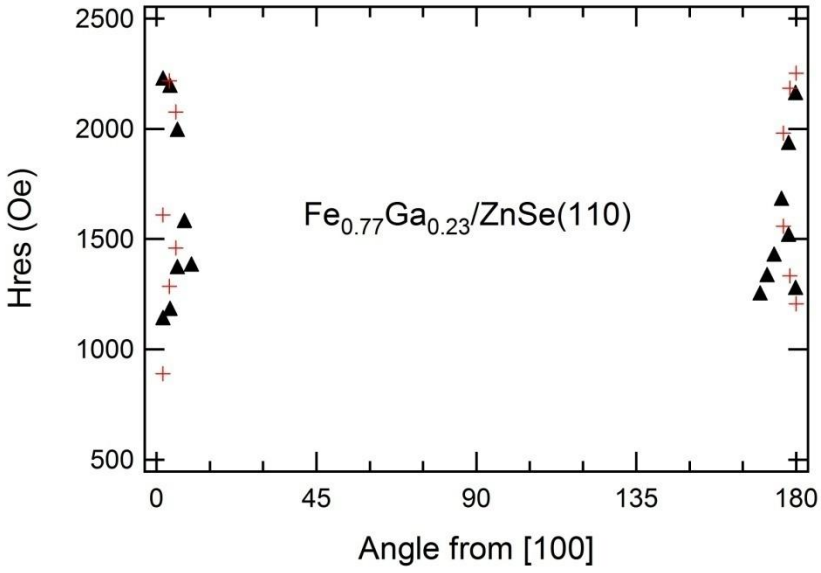

Figure 72: X-band resonance field for $Fe_{0.77}Ga_{0.23}$/ZnSe(110) data with fitting. The black triangles are experimental data and the red crosses are fittings.

Figures 73 and 74 plot the Q-band data for pure Fe and 15% Ga doping. Figure 73 shows the pure Fe/ZnSe(110) sample with its fits and also showing the fit which is only cubic without the uniaxial magnetic anisotropy. It should be noted that to get a good fit, a cubic anisotropy plus a uniaxial anisotropy is essential.

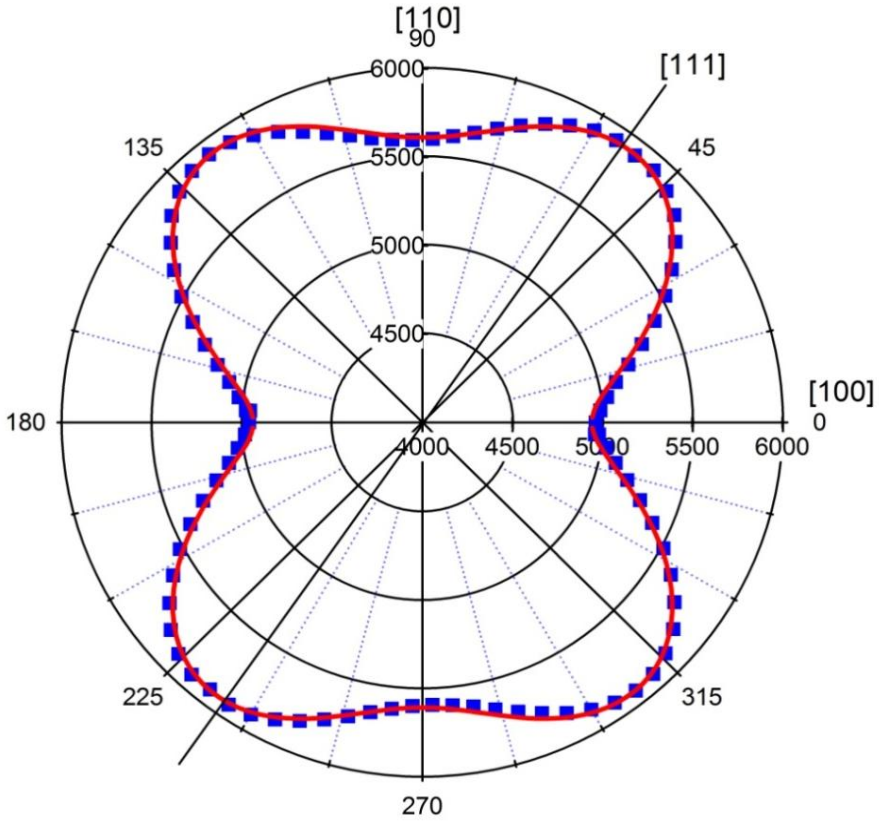

Figure 73: Q-band resonance field for pure Fe on ZnSe(110) . The blue triangles are experimental data and the red line is the fitting.

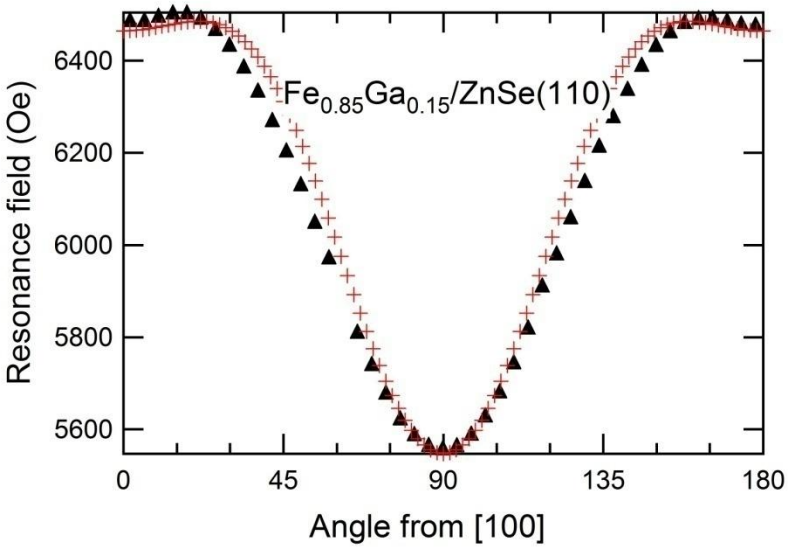

Figure 74: Q-band resonance field for $Fe_{0.85}Ga_{0.15}$/ZnSe(110). The black triangles are experimental data and the red crosses are fittings.

Different Concentration Samples

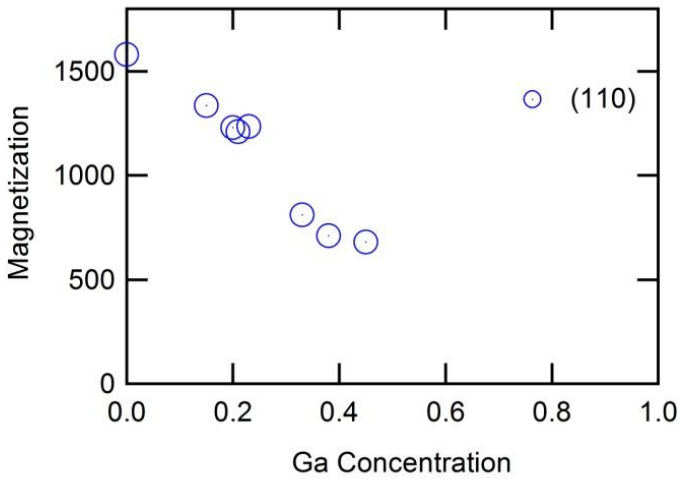

Figure 75: Effective magnetization extracted from Q-band FMR measurement.

Magnetization: The magnetization of $Fe_{1-x}Ga_x$/ZnSe(110) has been extracted from the FMR fitting by assuming that there is no perpendicular magnetic anisotropy except the demagnetization field, the results are shown in Figure 75.

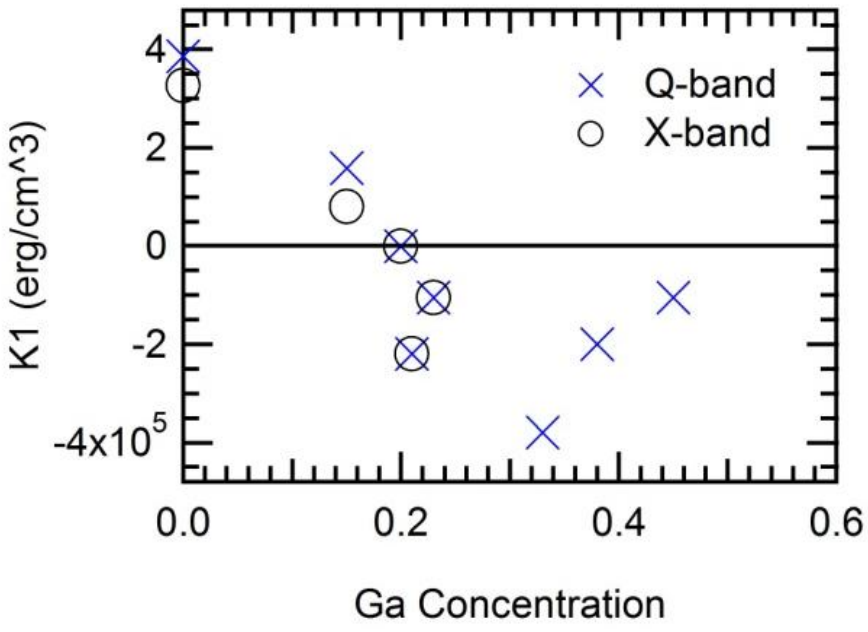

Figure 76: Cubic anisotropy energy density changes with Ga concentration.

Cubic Magnetic Anisotropy Constant K_1: For bulk $Fe_{1-x}Ga_x$ samples, the anisotropy energy consists of cubic term K_1 and K_2. Because the K_2 is small compared with K_1 for $Fe_{1-x}Ga_x$ and the effect is to higher order, so it can be ignored. K_1 value decreased with doping of Ga and reaches zero at about 19% of Ga doping. Then the K_1 value changed sign for higher doping. From theory, usually the magnetic anisotropy constant K_1 is not affected by lattice distortions. For our thin films, K_1 has been extracted from the FMR fitting and the results are listed in Figure 76. K_1 had positive value of

3.86×10^5 erg/cm^3 for pure Fe on (110) surface and it gradually decreased to zero at 20% Ga doping. Then the cubic anisotropy changed sign and became negative for dopings greater than 20%. As the doping increases, K_1 grows and goes to a maximum value of -3.8×10^5 erg/cm^3 at 33% Ga concentration, and then decreases towards zero after 33% of doping. From the graph we can see that the cubic term followed the same trend compared with $Fe_{1-x}Ga_x$ deposited onto ZnSe (001) surfaces and the bulk values [6].

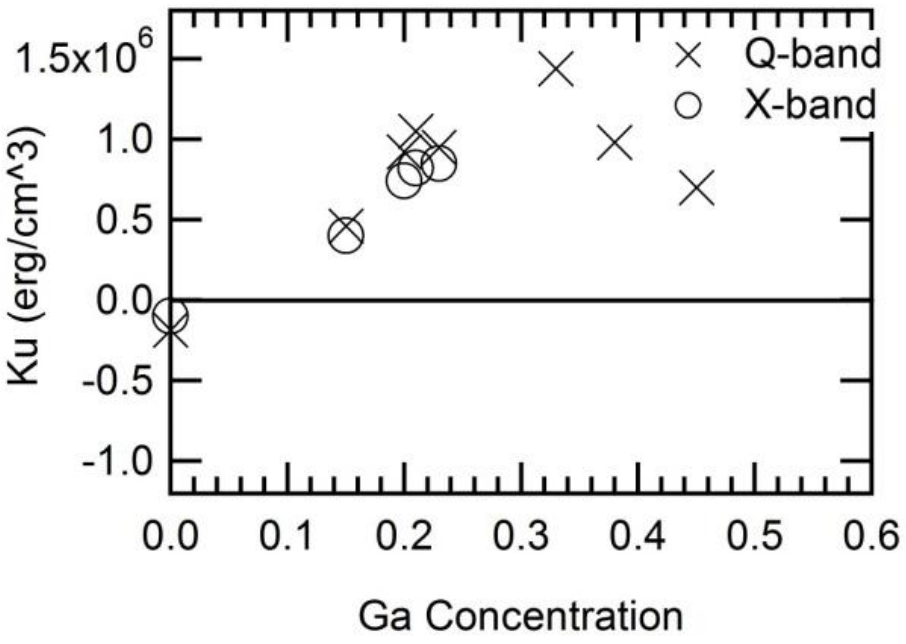

Figure 77: Extracted uniaxial anisotropy density as a function of Ga concentration.

In-Plane Uniaxial Magnetic Anisotropy Constant K_u: In the bulk $Fe_{1-x}Ga_x$ form, the magnetic anisotropy is purely cubic and no uniaxial term shows up [6]. But when $Fe_{1-x}Ga_x$ is deposited onto substrate, because of the asymmetry of chemical bonding at the substrate surface, and anisotropic strain relaxation is expected in the film [36]. This leads to a uniaxial anisotropy term. The uniaxial anisotropy constants for $Fe_{1-x}Ga_x$ deposited

on ZnSe (110) surface is listed in the Figure 77. For pure Fe, the easy axis is in the [100] direction and the hard axis is in the [110] direction. With doping of Ga, the uniaxial anisotropy changed direction, easy axis changed to [110] direction and hard axis changed to [100] direction. As the doping increases, the uniaxial anisotropy grows and reaches a peak value of 1.44×10^{6}erg/cm^3 at 33% doping. Compared with $Fe_{1-x}Ga_x$ doped on (100) substrate, the uniaxial anisotropy K_u is much bigger on the (110) surface.

Different Thickness Samples

$Fe_{0.79}Ga_{0.21}$ samples deposited on ZnSe (110) surface have been grown at 10 nm, 20 nm and 40 nm. Angle-dependent FMR have been carried out to investigate the thickness effects on anisotropy constants.

Thickness Dependence of Cubic Anisotropy K_1: The cubic anisotropy fitting results for the different thickness samples is shown in Figure 78. The K_1/M value for 10 nm sample is -215 Oe. The value does not change much as thickness increased from 10 nm to 40 nm.

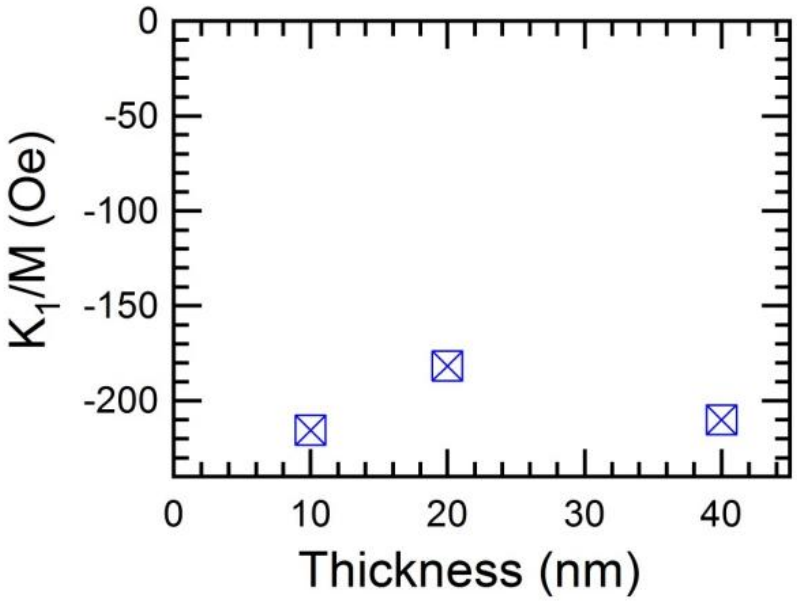

Figure 78: K1/M value for different $Fe_{1-x}Ga_x$ film thickness on ZnSe(110).

Thickness Dependence of the In-Plane Uniaxial Anisotropy: The uniaxial anisotropy energy density values over magnetization for the 21% Ga doping in different thicknesses are listed in Figure 79. We see that the easy axis of the uniaxial term is always in the <110> direction and does not switch sign as thickness changes. The value of the uniaxial term is above 800 Oe, which is much larger than that on the (001) surface. At thickness of 10 nm, Ku/M is 1073 Oe. Compared with Ku on (001) surface, where the Ku/M is 96 Oe, it is one order of magnitude larger. Ku/M decreases as thickness increases, but the value at 40nm is 870 Oe, which is still very large. To extract bulk and surface contributions to the uniaxial anisotropy, the thickness dependent data has been fitted using:

$$K_{eff} = K_{bulk} + K_{surface} / t, \tag{32}$$

where t is the thickness of the thin film.

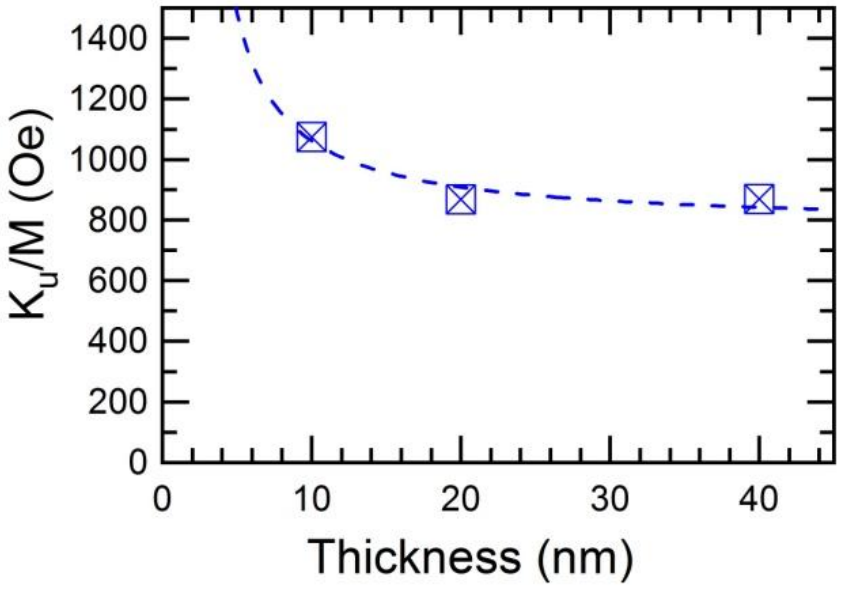

Figure 79: Uniaxial anisotropy energy density Ku/M value changes with thickness. The squares are extracted values from experiment. The dotted line is fitted to the data using equation $K_{eff} = K_{bulk} + K_{surface} / t$.

The fitting gives a bulk value of Bulk = 780.67 ± 58.1 Oe and interface value of 0.00023 erg/cm^2, which is much smaller than the interface value of 0.0095 erg/cm^2 for the (001) surface.

Summary

We have conducted angular FMR measurements on different Ga concentration of $Fe_{1-x}Ga_x$ samples deposited on ZnSe(110) surfaces. Rotational FMR results showed that the anisotropy energy consists of a cubic and a uniaxial term. From fitting to the resonance field versus angle data, cubic anisotropy K_1 and uniaxial anisotropy Ku have been extracted. The results show that the cubic anisotropy follow the same trend as bulk

$Fe_{1-x}Ga_x$ and the anisotropy energy density is close to $Fe_{1-x}Ga_x$/ZnSe(001). The uniaxial anisotropy starts with the easy axis in [100] direction and switches to [110] direction with doping of Ga. The uniaxial term grows as Ga doping and reaches the maximum value at 33% Ga concentration. The thickness results show that the uniaxial term stays large even for thick sample at 40 nm.

Compared with $Fe_{1-x}Ga_x$ deposited on the ZnSe(001) surface, the cubic anisotropy energies are almost the same whereas the uniaxial terms are much bigger on the (110) surfaces. The uniaxial term changed sign at 15% Ga concentration, which is slightly different from $Fe_{1-x}Ga_x$ on (001) surface, where uniaxial term changed sign at 23% Ga concentration. We suspect the reason for the bigger value of the uniaxial term is because the anisotropic lattice relaxation in the (110) surface is bigger than in the (001) surface. The uniaxial term stays in thick films is because the misfit which releases the strain happened much slower in the (110) surfaces.

For Fe deposited onto GaAs(110) surfaces, the easy axis direction switched with change of Fe film thickness. When the Fe film thickness is small, the easy axis is in the <110> direction and when the Fe film thickness is large, the easy axis switches to <100> direction. Considering that Ga and As have a big out diffusion effect into Fe, Ga atoms were trapped near the interface while As atoms were distributed all over the film. And the easy axis direction for the thinnest Fe/GaAs(110) film is the same as the high doping of $Fe_{1-x}Ga_x$/ZnSe(110), while the easy axis directions are the same for thick Fe/GaAs(110) films and Fe/ZnSe(110) films. So the change of easy axis with thickness in the Fe/GaAs(110) might be caused by the concentration change of Ga out diffusion into Fe film and formed $Fe_{1-x}Ga_x$ in the ultrathin film.

Linewidth Analysis

The analysis of linewidthes for FMR is a long-standing problem. It is a difficult task to interpret the experimental data with current theories involving elementary excitations and microscopic interactions. The study of resonance line broadening is one of the main procedures for investigating the relaxation mechanisms and the laws governing the basic types of interactions in a ferromagnetic system. The FMR linewidth in bulk metals is mainly due to the exchange-conductivity mechanism and the intrinsic damping. When investigating magnetic thin films deposited onto substrate, additional contributions from the surface, interface and the dispersion of the local axes of the anisotropy must be taken into account [91].

Because the linewidth analysis is so complicated and it is beyond the scope of this dissertation, here I list the results of the linewidth without going into detailed analysis. The Q-band linewidth for several Ga concentrations have been plotted in Figures 80-83.

In general, the linewidth goes up with the doping of Ga. For pure Fe and 7% Ga doping, the linewidths are in complicated form. For pure Fe, the linewidthes are big when the magnetization is in the hard axis[110], and small along the directions of easy axis[100]. For 7% Ga doping, the linewidths have peaks along <110> and <100>. For higher concentration, as the cubic anisotropy changes directions, the linewidth peaks also switches to <100> direction. It seems like the 7% doping linewidth has a combination of Pure Fe character and high Ga concentration character.

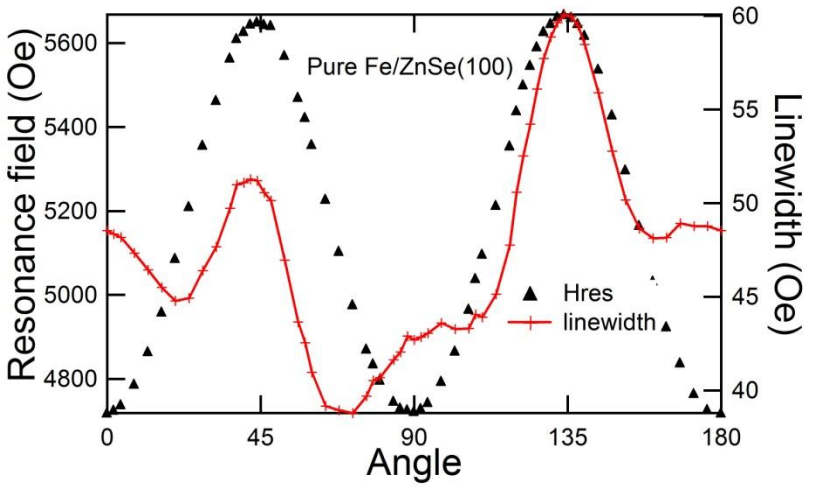

Figure 80: Pure Fe/ZnSe(001), angular linewidth and resonance field.

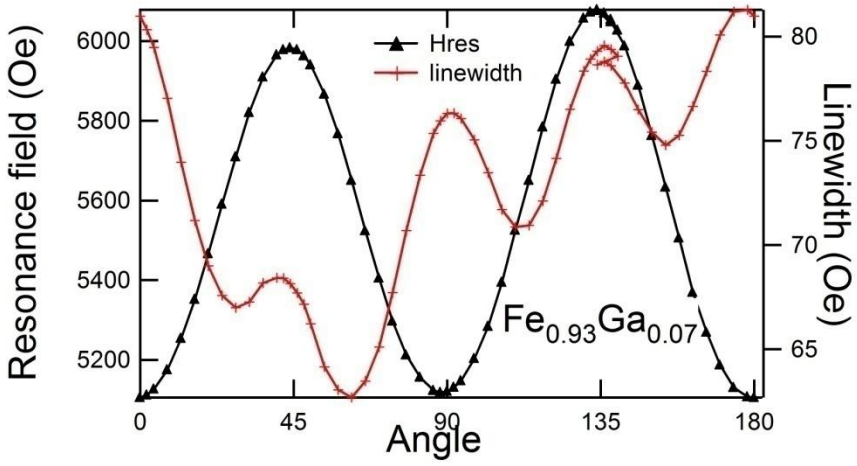

Figure 81: $Fe_{0.93}Ga_{0.07}$/ZnSe(001), angular linewidth and resonance field.

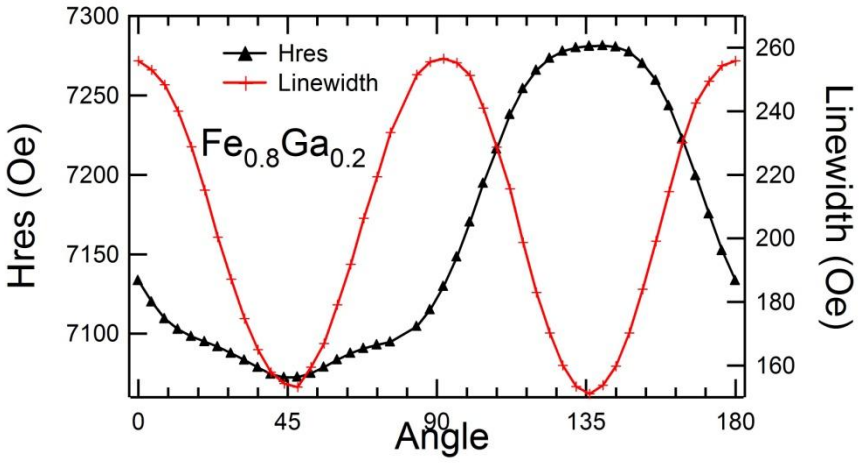

Figure 82: $Fe_{0.8}Ga_{0.2}$/ZnSe(001), angular linewidth and resonance field.

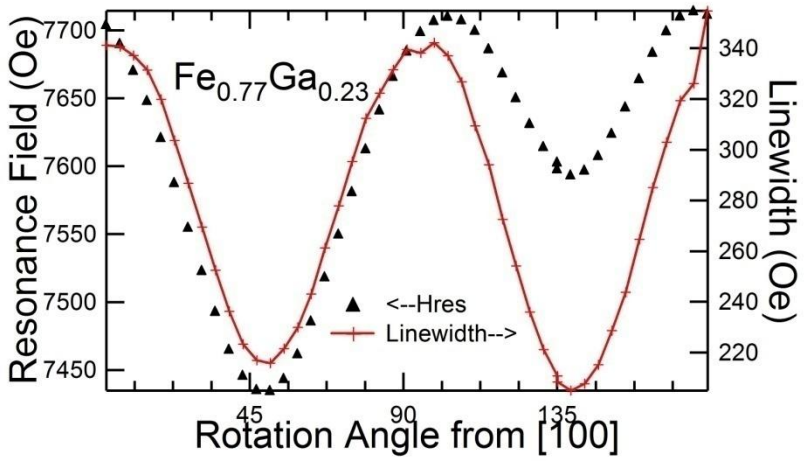

Figure 83: $Fe_{0.77}Ga_{0.23}$/ZnSe(001), angular linewidth and resonance field.

Dynamic magnetization switching has attracted more and more interests because of its relevance to the performance of magnetic data storage, inductors, transformers and other magnetic devices. In order to achieve tuning of resonance frequency and magnetic damping parameters, techniques like doping with rear earth elements Gd, Tb, Dy, and

Ho, Nb, doping with 3d or 5d transition metals Zr, covering a layer of antiferromagnetic materials, depositing multilayers, or controlling sputtering oblique angles have been used. In fact, tuning of resonance frequency can be easily achieved using tuning of saturation magnetization. But tuning of damping in a controlled way is hard to achieve.

Study of magnetic resonance line broadening is one of the main techniques to investigate relaxation mechanisms. But the analysis of linewidthes for FMR is a long-standing problem. The linewidth combines the real damping and inhomogeneous broadening. And the real damping consists of intrinsic damping and extrinsic damping such as two magnon scattering. In this dissertation, we report doping Ga effect on relaxation and resonance frequency for $Fe_{1-x}Ga_x$/ZnSe(001).

Zero field frequency is the precession frequency of the magnetic moment with no external magnetic field. The zero field frequency can be calculated after we find out the magnetic anisotropy fields for the sample. Zero field frequency can be tuning either by change of magnetic anisotropy or saturation magnetization. Figure 84 shows the zero field frequency calculated from X-band FMR fitting results. We can see that the natural frequency decreases with Ga doping as a result of a decrease in both magnetization and magnetic anisotropy. As Ga doping exceeds 20%, due to the mixed effect of magnetic anisotropy and magnetization, natural frequency does not change much.

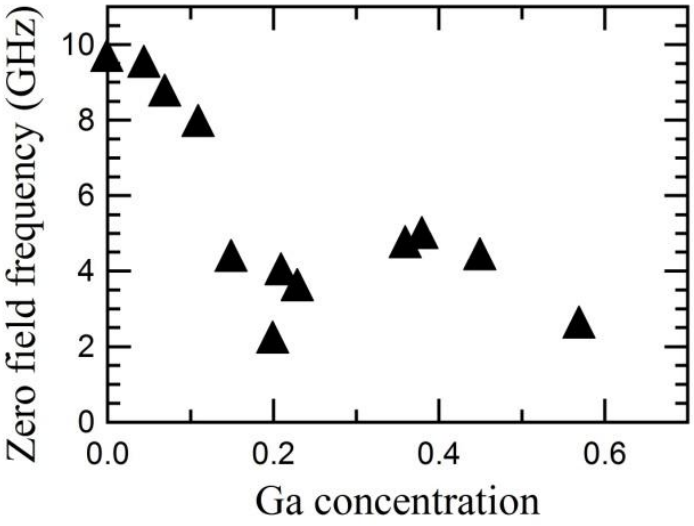

Figure 84: Zero field resonance frequencies for different Ga dopings.

The linewidth contains information about relaxation and inhomogeneous broadening. We can separate these two effects using

$$\Delta H = \Delta H(0) + 1.16(\frac{\omega}{\gamma}) \cdot (\frac{G}{\gamma M_s}) \tag{33}$$

Where ΔH is the linewidth, $\Delta H(0)$ is the zero frequency broadening and G is the Gilbert damping parameter, ω is the resonance frequency, *Ms* is the saturation magnetization. If we have ΔH for multiple frequencies, both the zero frequency broadening ΔH(0) and G can be extracted out. We did FMR for our samples in X-band and Q-band, and extracted G factors in (110) direction. Figure 85 listed the Gilbert damping parameters and Figure 86 listed the zero frequency broadening for different Ga dopings. We saw that both Gilbert damping parameter and zero frequency broadening had a sudden change at 20% Ga doping, which indicates a phase change at around 20%

doping. (Note: hard axis changed into easy axis at 20% doping. I would like to extract damping in the easy axis for all the samples, but X-band does not have spectra in the easy axis direction at low Ga dopings. Therefore the (110) directions were used instead of the easy axis directions.)

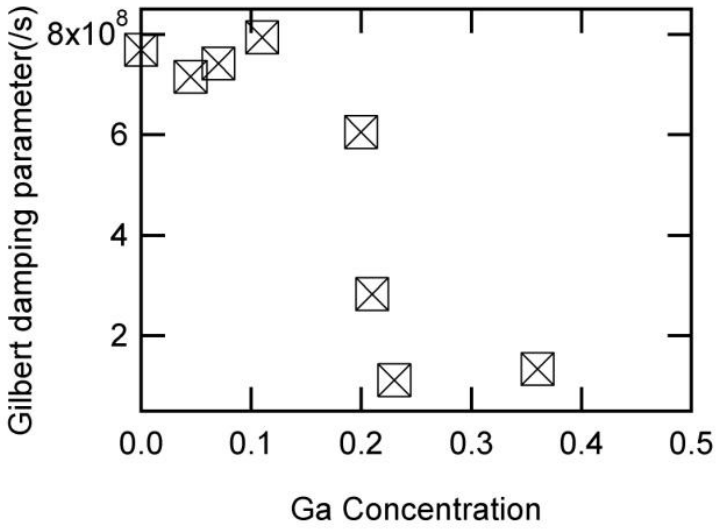

Figure 85: Gilbert damping in the (110) direction, which is hard axis for Ga<20% and easy axis for Ga>20%.

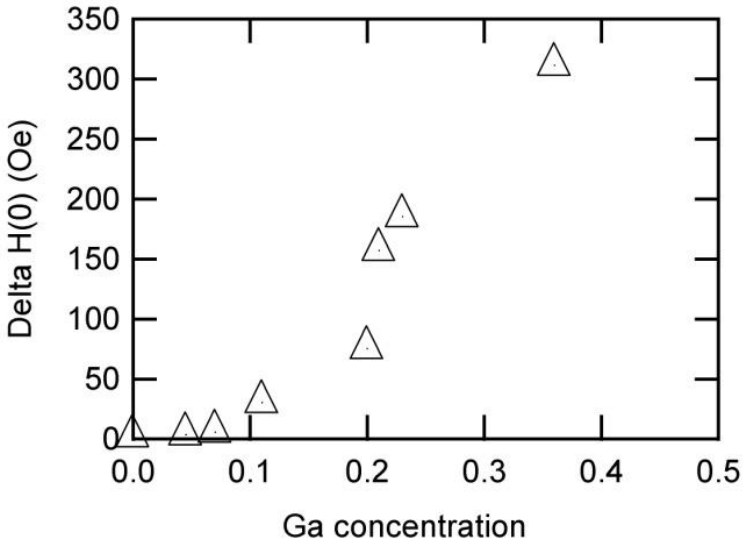

Figure 86: ΔH(0) in the (110) directions for different Ga dopings.

Linewidths for $Fe_{1-x}Ga_x$/ZnSe(110)

The linewidths of the samples increase from 100 Oe to 340 Oe when Ga concentration goes from 0% to 45%. Resonance fields extracted from fitting to the spectra as function of angles for pure Fe film are shown in Figure 87.

The linewidth for $Fe_{1-x}Ga_x$/ZnSe(110) has the same trend as $Fe_{1-x}Ga_x$/ZnSe(001) that the linewidth goes up as doping of Ga. The sharpest and biggest linewidthes for all the samples are plotted in Figure 87. The linewidth is always the biggest along [100] direction whether it is the easy axis or hard axis. It drops down to minimum linewidth along [111] and then increases toward [110] direction. The reason why the linewidths do not have the two trends like $Fe_{1-x}Ga_x$/ZnSe(100) is unknown.

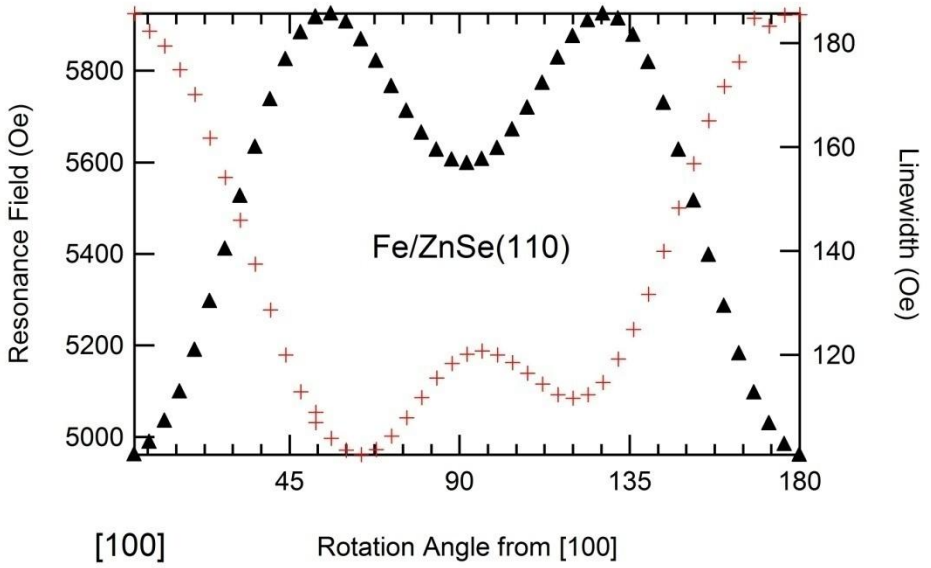

Figure 87: Linewidthes for Pure Fe/ZnSe(110) from Q-band FMR measurements. The black triangles are resonance fields and the red crossings are linewidths.

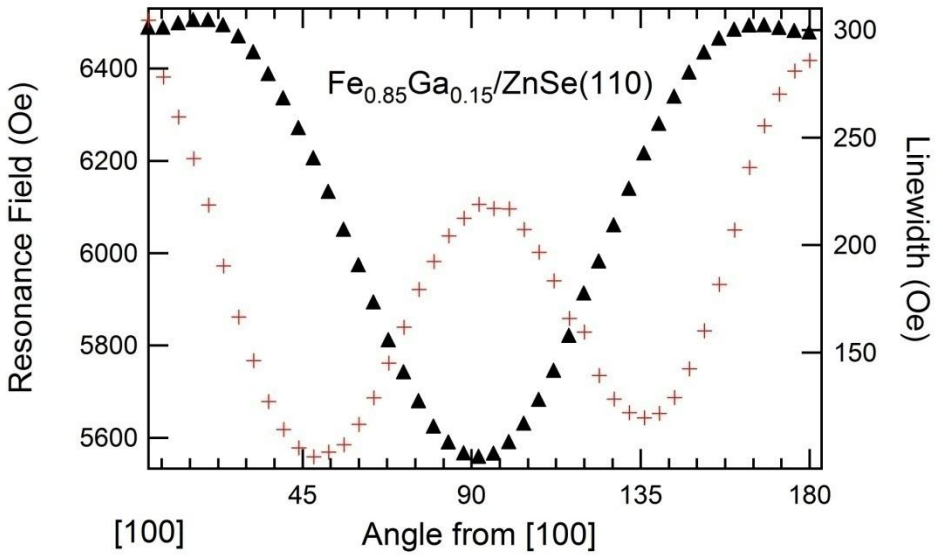

Figure 88: Linewidthes for $Fe_{0.85}Ga_{0.15}$/ZnSe(110) from Q-band FMR measurements. The black triangles are resonance fields and the red crossings are linewidths.

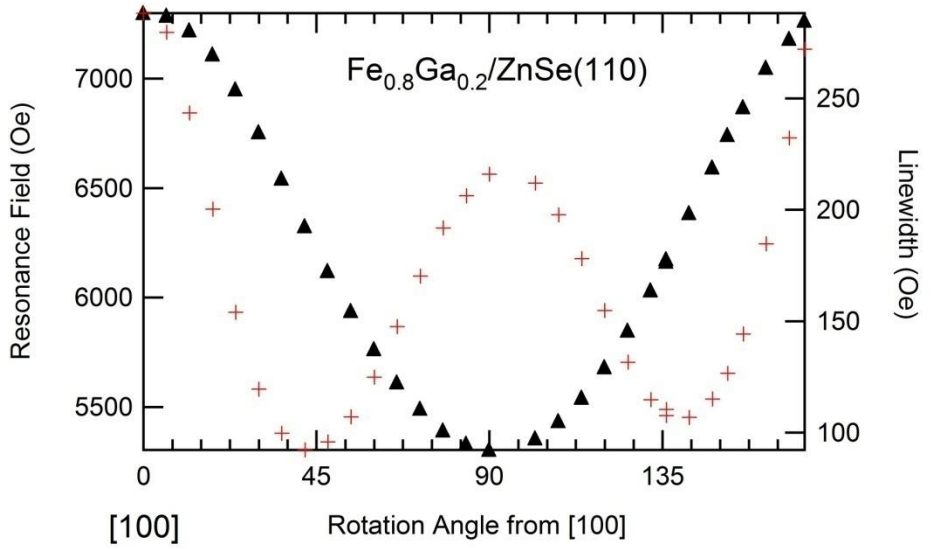

Figure 89: Linewidthes for $Fe_{0.8}Ga_{0.2}$/ZnSe(110) from Q-band FMR measurements. The black triangles are resonance fields and the red crossings are linewidths.

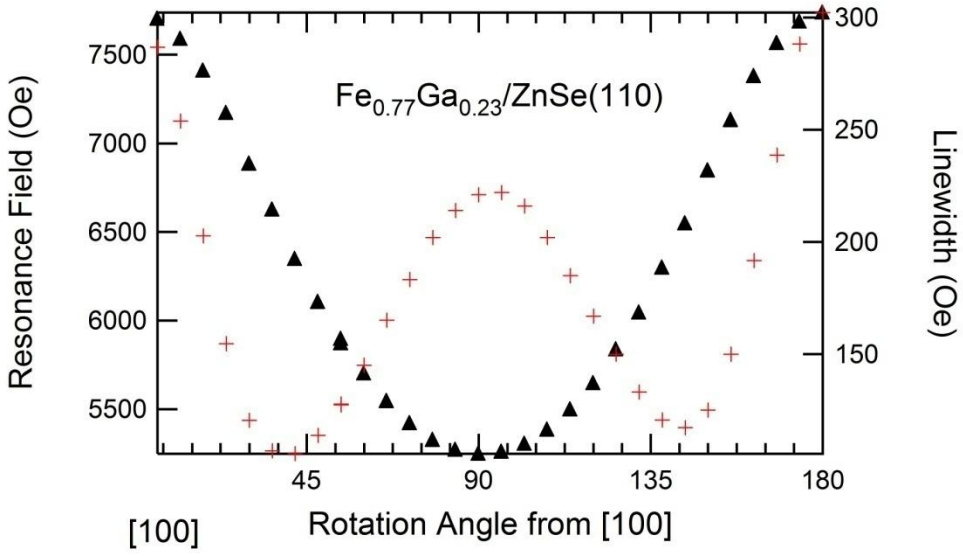

Figure 90: Linewidths for $Fe_{0.77}Ga_{0.23}$/ZnSe(110) surfaces from Q-band FMR measurements. The black triangles are the experimental data of the resonance field, and red crosses are the linewidths.

CONCLUSION AND OUTLOOK

While magnetostrictive thin films have many applications, the effects on the magnetic anisotropy and spin relaxation by clamping it onto a substrate need to be investigated. Since $Fe_{1-x}Ga_x$ is a magnetostrive material, applying a magnetic field will cause it to deform. It is necessary to investigate the field dependence of magnetic anisotropy and spin relaxation.

The first goal of the thesis is to find the interface effect (both chemical bonding and strain effect) on the magnetic anisotropy of $Fe_{1-x}Ga_x$ deposited on ZnSe(001) and ZnSe(110) surface. The second goal is to find how the relaxation time changes with the doping of Ga into BCC Fe for thin $Fe_{1-x}Ga_x$ films. The third goal is to find whether or not the magnetic anisotropy or relaxation time is magnetic field dependent. The reason for the third goal is because $Fe_{1-x}Ga_x$ is a magnetostrictive material. When placed under a magnetic field, the material will deform. When it is clamped onto a substrate, the deformation will be restricted by the substrate. This deformation will affect the magnetic anisotropy through magneto-elastic energy, and through spin-orbit coupling. The deformation will also affect the magnetic damping through spin-orbit coupling.

To investigate the interface effect, different thickness samples have been prepared and FMR measurements have been performed on them. The results show that the uniaxial magnetic anisotropy terms are bigger for thin films for both $Fe_{1-x}Ga_x$/ZnSe(001) and $Fe_{1-x}Ga_x$/ZnSe(110) than Fe/ZnSe. Even though the uniaxial term is bigger for $Fe_{1-x}Ga_x$/ZnSe(110) than $Fe_{1-x}Ga_x$/ZnSe(001), the interface effect is smaller for $Fe_{1-x}Ga_x$/ZnSe(110).

To investigate the Ga doping effect, a series of different Ga concentration samples have been made and FMR measurements have been performed on them. FMR results for both the $Fe_{1-x}Ga_x$/ZnSe(001) and $Fe_{1-x}Ga_x$/ZnSe(110) show that the uniaxial term changed dramatically with Ga doping, and the easy axis even changed directions. For low Ga-doped samples, the easy-axes are in the same direction as thick Fe/GaAs samples, and for high Ga doped samples, the easy-axis are in the same direction as thin Fe/GaAs samples. We belive that the reason for the uniaxial term in the Fe/GaAs system to switch direction can be explained by Ga outdiffusion and formed $Fe_{1-x}Ga_x$ thin layers.

We have performed X-band and Q-band FMR measurements. The comparison showed that the uniaxial term is field dependent.

The reason for a uniaxial term existing has been pinned down to 2 reasons. First, the directional bonding on the substrate surface changes the electronic structure of the Fe atoms and creates a uniaxial anisotropy. Second, the directional bonding affects the growth of $Fe_{1-x}Ga_x$ thin films and creates an anisotropic growth pattern and thus creates the anisotropic strain relaxation. Those two reasons can both create a uniaxial anisotropy, but the uniaxial anisotropy from the directional bonding cannot change direction with doping, so it cannot explain why the doping of Ga will switch the uniaxial anisotropy direction. We therefore conclude that the switch of the direction of the uniaxial term is due to the anisotropic relaxation in the sample.

Spin relaxation has been investigated using FMR linewidthes. The Lorentzian fit to our data show that the inhomogeneous broadening is not a big factor for the linewidth broadening. A brief analysis shows that the zero field frequency drops with Ga doping

until 20%, then stayed constant. A more detailed field dependent analysis need to do done to investigate field effects.

Future Work

The interface between a magnetoelastic material and its substrate is so interesting that many research projects can still be performed in this field. The following research questions are of interest.

1. When a magnetoelastic material is deposited on a ferroelectric material, will both materials' integrity still be held?
2. At the interface, is the bonding strong or weak? What kind of interface will produce a strong bonding? What kind of interface will produce a weak bonding?

The magnetic relaxation of these films is also a very interesting research topic as it is so complicated. The FMR linewidth is very sensitive to the growth procedure. We have already seen interesting behaviors as the doping of Ga is changed. For the relaxation, we expect it to change with field due to spin-orbit relaxation. Since field dependent relaxation is expected, the linewidth should not obey the simple $\Delta H = \Delta H(0) + 1.16\left(\frac{\omega}{\gamma}\right)\cdot\left(\frac{G}{\gamma M_s}\right)$ relation, which means that the linewidth versus frequency relation should not be a straight line. To prove this, FMR needs to be done in more than two frequencies to see if there is frequency dependent relaxation.

APPENDIX A

FMR FOR EXCHANGE COUPLED MAGNETIC LAYERS

In the previous sections, we have studied FMR for magnetic thin films in the (001) plane and (110) plane in both X-band and Q-band. After we measured FMR for the $Fe_{1-x}Zn_x/MgO$ sample, we noticed that we would need the exchange coupled magnetic layers FMR theory for the fitting. So in this section, we will discuss the FMR theory for exchange coupled magnetic thin layers.

For a magnetic thin film with two layers of ferromagnetic materials, they are other either anti-ferromagneticly or ferromagneticly coupled to each. So, there will be a coupling strength between them. This problem is similar to the classical mechanics problem we did in the course work, where two harmonic oscillators are coupled by a spring, as shown in Figure A1.

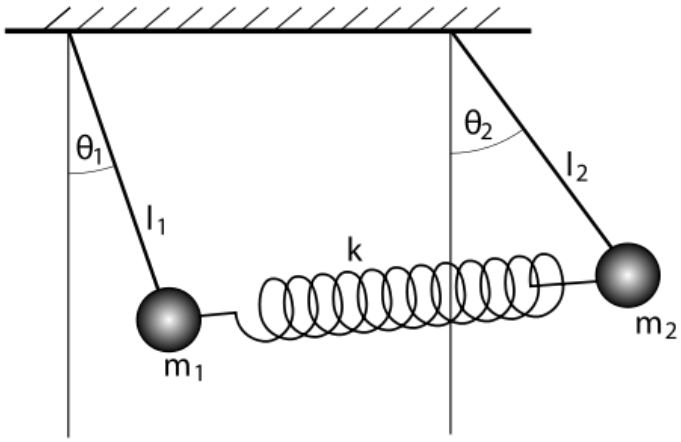

Figure A1: Coupled harmonic oscillators.

In this classical problem, we have two harmonic oscillators with same oscillating frequencies, but they are coupled by a spring. The normal mode frequencies of the oscillation consists of one mode where the two balls move in the same direction and the spring has a fixed length and do not play a role in the oscillation. Another mode is where

the two balls oscillate in opposite directions, so the spring undergoes a compress and stretch movement. In this scenario, the spring will affect the oscillation frequency of the balls.

The spin dynamics of exchange coupled magnetic thin layers are similar to the coupled pendula. The two layers of spins have their own precession frequency, and they are coupled through the exchange energy.

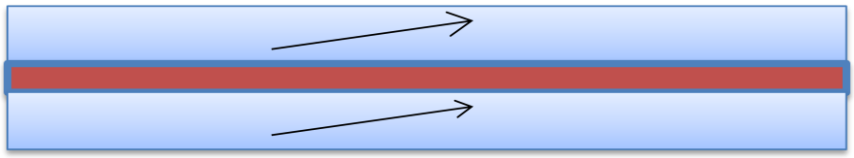

Figure A2: Coupled magnetic thin layers.

In the exchange coupled ferromagnetic layers, we have two layers of magnetic thin films, which are separated by a very thin layer of no-magnetic material. The non-magnetic layer is thin enough that the two magnetic layers are still exchange coupled. For these two layers, except their own magnetic anisotropies, they will experience another magnetic field from the exchange energy. The coupling could be ferromagnetic and anti-ferromagnetic. The exchange energy for the system can be written as: $E_{ex} = J_{12}\vec{M}_1 \bullet \vec{M}_2$.

So for the whole system, the energy can be written as: $E = E_1 + E_2 + J_{12}(\vec{M}_1 \cdot \vec{M}_2)$.

The process of finding the mode frequency is the similar as the coupled harmonic oscillators. The difference is that in this problem, the torque is perpendicular to the derivative of the energy surface. Suppose the equilibrium point of for the magnetic

moment is (θ_1, ϕ_1) and (θ_2, ϕ_2), and the energy for moments that are slightly off the equilibrium point can be written using Taylor expansion:

$$E = E_0 + \frac{1}{2}(E_{\theta_1\theta_1}\theta_1^2 + E_{\varphi_1\varphi_1}\varphi_1^2 + 2E_{\theta_1\varphi_1}\theta_1\varphi_1 + E_{\theta_2\theta_2}\theta_2^2 + E_{\varphi_2\varphi_2}\varphi_2^2 + 2E_{\theta_2\varphi_2}\theta_2\varphi_2 + 2E_{\theta_1\theta_2}\theta_1\theta_2 + \bullet\bullet\bullet) \tag{A1}$$

From the relation between magnetic moment and energy,

$$\begin{aligned} -M\dot{\theta} &= \gamma\partial E/\partial\varphi, \\ M\dot{\varphi} &= \gamma\partial E/\partial\theta. \end{aligned} \tag{A2}$$

The normal-mode frequencies for this system can be solved as:

$$\begin{bmatrix} E_{\theta_1\theta_1} & E_{\theta_1\varphi_1} + iz_1 & E_{\theta_1\theta_2} & E_{\theta_1\varphi_2} \\ E_{\varphi_1\theta_1} - iz_1 & E_{\varphi_1\varphi_1} & E_{\varphi_1\theta_2} & E_{\varphi_1\varphi_2} \\ E_{\theta_2\theta_1} & E_{\theta_2\varphi_1} & E_{\theta_2\theta_2} & E_{\theta_2\varphi_2} + iz_2 \\ E_{\varphi_2\theta_1} & E_{\varphi_2\varphi_1} & E_{\varphi_2\theta_2} - iz_2 & E_{\varphi_2\varphi_2} \end{bmatrix} \begin{bmatrix} \Delta\theta_1 \\ \Delta\varphi_1 \\ \Delta\theta_2 \\ \Delta\varphi_2 \end{bmatrix} = 0 \tag{A3}$$

Where

$$\begin{aligned} z_1 &= \omega M_1 \sin\theta_1/\gamma \\ z_2 &= \omega M_2 \sin\theta_2/\gamma \end{aligned} \tag{A4}$$

REFERENCES CITED

[1] R. R. Basantkumar, B. J. H. Stadler, W. P. Robbins, and E. M. Summers, Ieee-Inst Electrical Electronics Engineers Inc, 2006, p. 3102.

[2] R. Ramesh and N. A. Spaldin, Nat Mater 6 (2007) 21.

[3] A. E. Clark, Hathaway, K. B., Wun-Fogle, M., Restorff, J. B., Lograsso, T. A., Keppens, V. M., Petculescu, G., Taylor, R. A., Journal of Applied Physics 93, (2003) 8621.

[4] A. E. Clark, J. H. Yoo, J. R. Cullen, M. Wun-Fogle, G. Petculescu, and A. Flatau, Vol. 105, Journal of Applied Physics, 2009, p. 07A913.

[5] J. M. Borrego, J. S. Blazquez, C. F. Conde, A. Conde, and S. Roth, Intermetallics 15 (2007) 193.

[6] S. Rafique, J. R. Cullen, M. Wuttig, and J. Cui, Journal of Applied Physics 95 (2004) 6939.

[7] With kind permission from Springer Science+Business Media: magnetostriction of binary and ternary Fe-Ga alloys, Journal of Materials Science 42 (2007) 9582, E. Summers, T. Lograsso, and M. Wun-Fogle, figure 1.

[8] G. Wastlbauer, and J. A. C. Bland, Advances in physics 54 (2005) 137.

[9] G. A. Prinz, B. T. Jonker, J. J. Krebs, J. M. Ferrari, and F. Kovanic, Applied Physics Letters 48 (1986) 1756.

[10] J. J. Krebs, Jonker, B. T., Prinz, G. A., Journal of Applied Physics 61 (1987) 3744.

[11] F. Gustavsson, E. Nordstrom, V. H. Etgens, M. Eddrief, E. Sjostedt, R. Wappling, and J. M. George, Physical Review B 66 (2002)

[12] A. Javed, N. A. Morley, and M. R. J. Gibbs, Journal of Magnetism and Magnetic Materials 321 (2009) 2877.

[13] B. W. Wang, S. Y. Li, Y. Zhou, W. M. Huang, and S. Y. Cao, Journal of Magnetism and Magnetic Materials 320 (2008) 769.

[14] O. M. J. v. t. Erve, C. H. Li, G. Kioseoglou, A. T. Hanbicki, M. Osofsky, S. F. Cheng, and B. T. Jonker, Applied Physics Letters 91 (2007) 122515.

[15] G. A. Prinz, Rado, G. T., Krebs, J. J., Journal of Applied Physics 53 (1982)

[16] W. Jantz, G. Rupp, R. Smith, W. Wettling, and G. Bayreuther, Magnetics, IEEE Transactions on 19 (1983) 1859.

[17] B. T. Jonker and G. A. Prinz, Journal of Applied Physics 69 (1991) 2938.

[18] B. T. Jonker, G. A. Prinz, and Y. U. Idzerda, Journal of Vacuum Science & Technology B: Microelectronics and Nanometer Structures 9 (1991) 2437.

[19] A. McClure, S. Albert, T. Jaeger, H. Li, P. Rugheimer, J. A. Schaefer, and Y. U. Idzerda, Journal of Applied Physics 105 (2009) 07A938.

[20] R. J. Lancashire, http://wwwchem.uwimona.edu.jm:1104/courses/CFT.html

[21] R. C. O'Handly, Modern Magnetic materials, principles and applications. (2000)

[22] C. Kittel, Reviews of Modern Physics 21 (1949) 541.

[23] D. A. Resnick, Ph. D Thesis (2005)

[24] O. Ikeda, R. Kainuma, I. Ohnuma, K. Fukamichi, and K. Ishida, Journal of Alloys and Compounds 347 (2002) 198.

[25] H. Okamoto, phase diagrams of binary iron alloys, ASM internal, Materials Park, OH,.

[26] R. Wu, Journal of Applied Physics 91 (2002) 7358.

[27] S. Tomiya, R. Minatoya, H. Tsukamoto, S. Itoh, K. Nakano, E. Morita, and A. Ishibashi, Journal of Applied Physics 82 (1997) 2938.

[28] K.-i. Sano and T. Miyagawa, Applied Surface Science 60-61 (1992) 813.

[29] T. L. Monchesky, B. Heinrich, R. Urban, K. Myrtle, M. Klaua, and J. Kirschner, Physical Review B 60 (1999) 10242.

[30] M. Zölfl, M. Brockmann, M. Köhler, S. Kreuzer, T. Schweinböck, S. Miethaner, F. Bensch, and G. Bayreuther, Journal of Magnetism and Magnetic Materials 175 (1997) 16.

[31] M. Brockmann, M. Zölfl, S. Miethaner, and G. Bayreuther, Journal of Magnetism and Magnetic Materials 198-199 (1999) 384.

[32] F. Bensch, G. Garreau, R. Moosbuhler, G. Bayreuther, and E. Beaurepaire, Journal of Applied Physics 89 (2001) 7133.

[33] E. Kneedler, P. M. Thibado, B. T. Jonker, B. R. Bennett, B. V. Shanabrook, R. J. Wagner, and L. J. Whitman, Vol. 14, AVS, 1996, p. 3193.

[34] E. M. Kneedler, B. T. Jonker, P. M. Thibado, R. J. Wagner, B. V. Shanabrook, and L. J. Whitman, Physical Review B 56 (1997) 8163.

[35] S. C. Erwin, S.-H. Lee, and M. Scheffler, Physical Review B 65 (2002) 205422.

[36] S. Mirbt, B. Sanyal, C. Isheden, and B. Johansson, Physical Review B 67 (2003) 155421.

[37] K.-i. Sano and T. Miyagawa, Jpn. J. Appl. Phys. 30 (1991) 1434.

[38] B. D. Schultz, C. Adelmann, X. Y. Dong, S. McKernan, and C. J. Palmstrom, Applied Physics Letters 92 (2008) 091914.

[39] A. Filipe, A. Schuhl, and P. Galtier, Applied Physics Letters 70 (1997) 129.

[40] S. Députier, R. Guérin, and A. Guivarc'h, Eur. Phys. J. AP 2 (1998) 127.

[41] S. Députier, R. Guérin, B. Lépine, A. Guivarc'h, and G. Jézéquel, Journal of Alloys and Compounds 262-263 (1997) 416.

[42] Y. B. Xu, E. T. M. Kernohan, D. J. Freeland, A. Ercole, M. Tselepi, and J. A. C. Bland, Physical Review B 58 (1998) 890.

[43] M. Doi, B. R. Cuenya, W. Keune, T. Schmitte, A. Nefedov, H. Zabel, D. Spoddig, R. Meckenstock, and J. Pelzl, Journal of Magnetism and Magnetic Materials 240 (2002) 407.

[44] B. R. Cuenya, M. Doi, W. Keune, S. Hoch, D. Reuter, A. Wieck, T. Schmitte, and H. Zabel, Applied Physics Letters 82 (2003) 1072.

[45] R. Moosbuhler, F. Bensch, M. Dumm, and G. Bayreuther, Journal of Applied Physics, 91 (2002), p. 8757.

[46] E. Sjöstedt, L. Nordström, F. Gustavsson, and O. Eriksson, Physical Review Letters 89 (2002) 267203.

[47] D. H. Mosca, M. Abbate, W. H. Schreiner, V. H. Etgens, and M. Eddrief, Journal of Applied Physics 90 (2001) 5973.

[48] E. Reiger, E. Reinwald, G. Garreau, M. Ernst, M. ZoÂ¨lfl, F. Bensch, S. Bauer, H. Preis, and G. Bayreuther, Journal of Applied Physics 87 (2000) 5923.

[49] M. Eddrief, M. Marangolo, V. H. Etgens, S. Ustaze, F. Sirotti, M. Mulazzi, G. Panaccione, D. H. Mosca, B. Lepine, and P. Schieffer, Physical Review B 73 (2006)

[50] M. Marangolo, F. Gustavsson, M. Eddrief, P. Sainctavit, V. H. Etgens, V. Cros, F. Petroff, J. M. George, P. Bencok, and N. B. Brookes, Physical Review Letters 88 (2002)

[51] R. Bertacco, M. Riva, M. Cantoni, F. Ciccacci, M. Portalupi, A. Brambilla, L. Duo, P. Vavassori, F. Gustavsson, J. M. George, M. Marangolo, M. Eddrief, and V. H. Etgens, Physical Review B 69 (2004)

[52] M. Meckenstock, D. Spoddig, K. Himmelbauer, H. Krenn, M. Doi, W. Kuene, Z. Frait, J. Pelzl, Journal of Magnetism and Magnetic Materials 240 (2002) 410.

[53] M. W. Ruckman, J. J. Joyce, and J. H. Weaver, Physical Review B 33 (1986) 7029.

[54] B. Q. Syed, M. Goldenberg, G. A. Prinz, and J. M. Ferrari, Journal of Vacuum Science & Technology B: Microelectronics and Nanometer Structures 3 (1985) 718.

[55] G. A. Prinz and J. J. Krebs, Applied Physics Letters 39 (1981) 397.

[56] J. J. Krebs, F. J. Rachford, P. Lubitz, and G. A. Prinz, Journal of Applied Physics 53 (1982) 8058.

[57] H. J. Haugan, B. D. McCombe, and P. G. Mattocks, Journal of Magnetism and Magnetic Materials 247 (2002) 296.

[58] Y. Ding, C. J. Alexander, and T. J. Klemmer, Journal of Applied Physics 93 (2003) 6674.

[59] R. Hollinger, M. Zolfl, R. Moosbuhler, and G. Bayreuther, Journal of Applied Physics 89 (2001) 7136.

[60] M. Madami, S. Tacchi, G. Carlotti, G. Gubbiotti, and G. Socino, Journal of Applied Physics 99 (2006) 08J701.

[61] M. Gester, C. Daboo, R. J. Hicken, S. J. Gray, A. Ercole, and J. A. C. Bland, Journal of Applied Physics 80 (1996) 347.

[62] L. Winking, M. Wenderoth, J. Homoth, S. Siewers, and R. G. Ulbrich, Applied Physics Letters 92 (2008) 193102.

[63] S. McPhail, C. M. Gürtler, F. Montaigne, Y. B. Xu, M. Tselepi, and J. A. C. Bland, Physical Review B 67 (2003) 024409.

[64] J. Lu, H. J. Meng, J. J. Deng, P. F. Xu, L. Chen, J. H. Zhao, and Q. J. Jia, Journal of Applied Physics 106 (2009) 013911.

[65] N. A. Morley, M. R. J. Gibbs, E. Ahmad, I. G. Will, and Y. B. Xu, Journal of Applied Physics 99 (2006) 08N508.

[66] K. Zakeri, T. Kebe, J. Lindner, and M. Farle, Journal of Magnetism and Magnetic Materials 299 (2006) L1.

[67] R. A. Gordon and E. D. Crozier, Physical Review B 74 (2006) 165405.

[68] P. M. Thibado, E. Kneedler, B. T. Jonker, B. R. Bennett, B. V. Shanabrook, and L. J. Whitman, Physical Review B 53 (1996) R10481.

[69] B. Aktas, B. Heinrich, G. Woltersdorf, R. Urban, L. R. Tagirov, F. Yildiz, K. Ozdogan, M. Ozdemir, O. Yalcin, and B. Z. Rameev, Journal of Applied Physics 102 (2007) 013912.

[70] R. Zuberek, K. Fronc, A. Szewczyk, and H. Szymczak, Journal of Magnetism and Magnetic Materials 260 (2003) 386.

[71] R. Zuberek, K. Fronc, W. Paszkowicz, and H. Szymczak, Journal of Magnetism and Magnetic Materials 283 (2004) 28.

[72] M. L. James, O. H. Qi, J. P. Christopher, and S. Susanne, Applied Physics Letters 93 (2008) 121909.

[73] O. Thomas, Q. Shen, P. Schieffer, N. Tournerie, and B. Lépine, Physical Review Letters 90 (2003) 017205.

[74] Y. B. Xu, D. J. Freeland, M. Tselepi, and J. A. C. Bland, Physical Review B 62 (2000) 1167.

[75] Y. B. Xu, D. J. Freeland, M. Tselepi, and J. A. C. Bland, Journal of Applied Physics 87 (2000) 6110.

[76] B. R. Cuenya, A. Naitabdi, E. Schuster, R. Peters, M. Doi, and W. Keune, Physical Review B 76 (2007) 094403.

[77] N. Tournerie, P. Schieffer, B. Lepine, C. Lallaizon, P. Turban, and G. Jezequel, Physical Review B 78 (2008) 12.

[78] Y. Zhai, L. Shi, W. Zhang, Y. X. Xu, M. Lu, H. R. Zhai, W. X. Tang, X. F. Jin, Y. B. Xu, and J. A. C. Bland, Journal of Applied Physics 93 (2003) 7622.

[79] F. Bensch, R. Moosbuhler, and G. Bayreuther, Journal of Applied Physics 91 (2002) 8754.

[80] R. S. Alger, Electron Paramagnetic Resonance: Techniques and Applications, interscience publishers, 1968.

[81] J. Smit, Beljers, H. G., Philips Res. Rep. 10 (1955)

[82] A. Suhl, Physical Review 97 (1954)

[83] J. O. Artman, Physical Review 105 (1957) 11.

[84] A. McClure, E. Arenholz, and a. Y. U. Idzerda, J. Vac. Sci. Technol. A28 (2010)

[85] E. Arenholz, G. van der Laan, A. McClure, and Y. Idzerda, Physical review B 82 (2010) 180405(R).

[86] H. Basumatary, M. Palit, J. A. Chelvane, S. Pandian, M. M. Raja, and V. Chandrasekaran, Scripta Materialia 59 (2008) 878.

[87] F. Bensch, G. Garreau, R. Moosbuhler, G. Bayreuther, and E. Beaurepaire, Vol. 89, AIP, 2001, p. 7133.

[88] M. Marangolo, F. Gustavsson, G. M. Guichar, M. Eddrief, J. Varalda, V. H. Etgens, M. Rivoire, F. Gendron, H. Magnan, D. H. Mosca, and J. M. George, Physical Review B 70 (2004)

[89] M. Bjorn, N. Florian, S. Matthias, S. Alexander, and B. Gunther, Journal of Applied physics 103 (2008) 07B528.

[90] A. Grunebohm, H. C. Herper, and P. Entel, Physical Review B 80 (2009) 064417.

[91] J. R. Fermin, A. Antonio, F. M. d. Aguiar, L. Biao, and S. M. Rezende, Journal of Applied physics 85 (1999) 7316.